

Climate Variability in East Asia in Simulations and Reconstructions in the Last 1200 Years

Dissertation

Zur Erlangung des Doktorgrades der Naturwissenschaften
im Department Geowissenschaften der Universität Hamburg

vorgelegt von

Dan Zhang

aus

Liaoning, China

Hamburg

2012

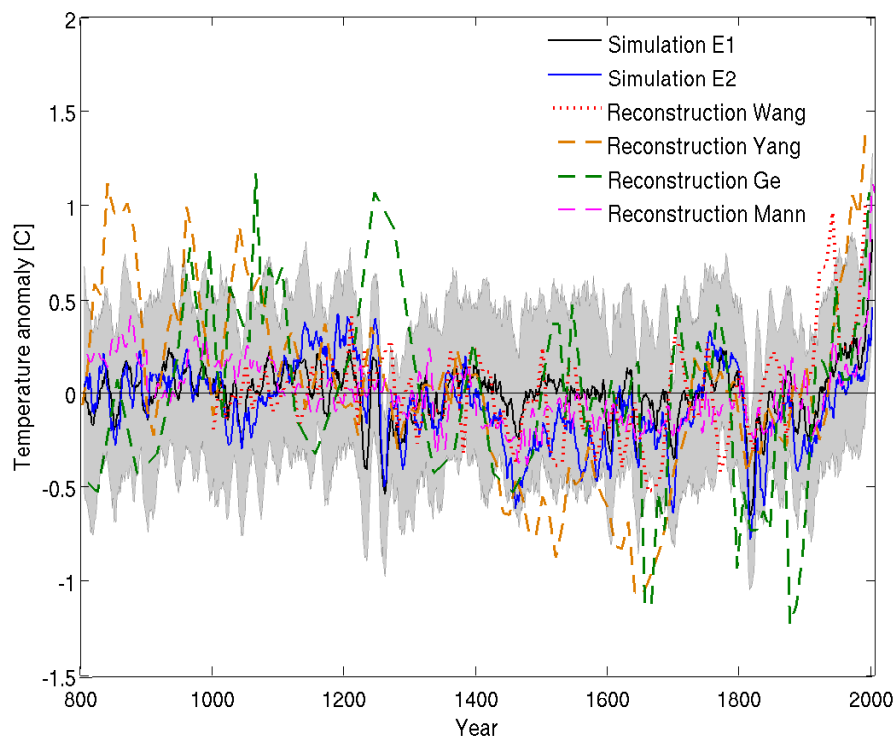
Als Dissertation angenommen von
Department Geowissenschaften der Universität Hamburg

Auf Grund der Gutachten von Prof. Dr. Klaus Fraedrich
und Dr. Richard Blender

Hamburg, den 21. Mai 2012

Professor Dr. Jürgen Oßenbrügge
Leiter des Department Geowissenschaften

Climate variability in East Asia in simulations and reconstructions in the last 1200 years



Dan Zhang

Hamburg 2012

Cover picture sources

From Zhang et al. (2010)

Near surface temperature anomalies [$^{\circ}\text{C}$] in China from simulations and reconstructions: Ensemble E1 (black/solid) forced by a weak solar forcing from Krivova et al. (2007, about 0.1% of the standard total solar irradiance (TSI) value of 1367W/m^{-2} , given by the difference between present-day and Maunder minimum); ensemble E2 (blue/solid) forced by a strong solar forcing from Bard et al. (2000, about 0.25% of the standard TSI); reconstructions by Wang et al. (2007b, dotted/red), Yang et al. (2002, dashed/brown), Ge et al. (2003, dashed/green), and Mann et al. (2009, dashed/magenta). The ensemble spread is indicated by the 11-year running means of simulated minimum and maximum in ensemble E1 (grey/shaded).

Contents

Dedication	iii
Abstract	1
List of Abbreviations	1
1 Introduction	1
1.1 Motivation	1
1.2 Scope, objective and outline	3
2 Temperature variability in simulations and reconstructions	9
2.1 Introduction	9
2.2 Data and methods	11
2.3 Reconstructed temperature in East Asia	14
2.4 Northern Hemisphere	15
2.5 Mutual assessment between simulations and reconstructions	17
2.5.1 Solar forcings and different reconstructions	19
2.5.2 Regional anomaly and ensemble spread	21
2.5.3 Centennial anomaly patterns and annual cycle	23
2.6 Summary and conclusion	27
3 Precipitation variability in simulations and reconstructions	29
3.1 Introduction	29
3.2 Data and methods	32
3.3 Reconstructed drought index in East Asia	36
3.4 Precipitation and runoff in Yangtze catchment in control run	38
3.4.1 Short and long term memory	39
3.4.2 Local and remote relationships	41
3.5 Precipitation variability in simulations and reconstructions	44
3.5.1 Centennial anomaly patterns	44
3.5.2 Regional anomaly and ensemble spread	44
3.6 Possible causes for rainfall deficits after 1800 AD	48
3.6.1 Internal forcing: anthropogenic land cover change and fossil fuel emissions	49
3.6.2 Asian summer monsoon	54

3.7	Summary and conclusion	57
4	Volcanic and ENSO effects: Global and East Asia	61
4.1	Introduction	61
4.2	Data and methods	63
4.3	Global volcanic response	69
4.3.1	Temperature and SPI	70
4.3.2	Winter warming	71
4.3.3	Recovery timescale	72
4.4	East Asia: volcanic and ENSO effects	73
4.4.1	Volcanic impacts without ENSO events	73
4.4.2	ENSO effects	75
4.4.3	Volcanic response with ENSO events	76
4.5	Tambora eruption in 1815	79
4.5.1	Temperature and SPI	79
4.5.2	ENSO optimal realization	80
4.6	Volcanic eruptions and Asian summer monsoon	83
4.7	Summary and conclusion	83
5	Climate change on the Tibetan Plateau and its effects on East Asia	87
5.1	Introduction	87
5.2	Model and experimental design	89
5.3	Climate change in the Tibetan Plateau and in eastern China	91
5.3.1	Surface albedo induced climate anomaly in the Tibetan Plateau and its influences in eastern China	91
5.3.2	Dynamical mechanisms	95
5.4	Summary and conclusion	96
6	Summary and outlook	99
6.1	Summary and conclusion	99
6.2	Outlook	107
	Appendixes	109
	A Figures	111
	B Methods and third party software	117
	List of figures	118
	List of tables	125
	Bibliography	129
	Acknowledgement	145

Dedication

In loving memory of all forerunners
and all those who attempt doing a PhD without success
not because they are not brilliant, hard-working, dedicated, and committed
but whose lack of ability in time management
and capacity to ride-on-the-wind of running-time
did make a shipwreck of their dreams.

We will forever be grateful to you,
for leaving your marks on the sound of time
So other generations yet-to-come
May learn from your folly and repent of their ways.

This thesis is dedicated to all
who were mad enough to desire the title of a Dr.

———Author Dr. Adetutu Mary Aghedo

Abstract

The climate variability during 800-2005 AD is investigated using ensemble simulations performed with the COSMOS-Atmosphere-Surface(Land)-Ocean-Biogeochemistry model ECHAM5/MPIOM/JSBACH forced by both anthropogenic and natural forcings. The millennium run is designed as two ensembles forced by a solar forcing with weak variability (E1, 5 members) and a solar forcing with strong variability (E2, 3 members). The study also includes a detailed comparison of the simulated results with reconstructed data in East Asia. The atmospheric model ECHAM5 is run at T31 resolution with 19 vertical levels up to 10hPa. The ocean model MPIOM has a horizontal grid spacing of about 3° with 40 unevenly spaced vertical levels and applies a conformal mapping grid with a horizontal resolution ranging from 22 km to 350 km. The carbon cycle is interactively transported in the atmosphere and the ocean.

First, the temperature variability in China is analyzed by a mutual assessment of three reconstructed and two simulated data sets which are obtained from ensembles E1 and E2. The model uncertainty is assessed by the ensemble spread as maximum and minimum in five members. After the comparison in terms of temperature anomaly and long term memory analysis, ensemble E1 with weak solar forcing and one reconstructed data set are selected for further comparison. In the three regions in China, ensemble E1 and the reconstruction reveal weak long-term anomaly periods known as the Medieval Climate Anomaly (MCA), the Little Ice Age (LIA), and the Modern Warming (MW), whereas reconstructed data hint to higher decadal variability in West China and centennial variability in Northeast China. Cold periods are found in 1200-1300 and in 1600-1900 AD in whole China. The coldest anomalies which are caused by volcanic eruptions in the beginnings of the thirteenth and the nineteenth centuries are only partly consistent with reconstructed data. After 1800, the annual cycle reduces in the Northeast and on the Tibetan plateau, whereas the eastern Pacific Ocean shows an enhanced summer-winter contrast.

Secondly, the simulated precipitation is compared with various reconstructed drought indices in China. The mutual assessment reveals less consistency compared to the surface temperature. The evolution of precipitation is dominated by random unpredictable internal dynamics in four considered regions (Northeast, Southeast, Northwest and Southwest China). The distinguishing decreasing trend in the simulated precipitation, which is not captured in the reconstructions, is analyzed through internal forcing (sensitivity experiments) and dynamical mechanism (the Asian summer monsoon system) to pursue the possible causes. The most plausible answers are attributed to the anthropogenic land cover change (ALCC), the rising fossil fuel CO₂ emission and the weakening Asian summer monsoon in the last century. The analysis is further completed by the variability of the precipitation and runoff in Yangtze catchment (the biggest river in China) as well as its relationship with the snow cover in the Tibetan Plateau, El Niño/Southern Oscilla-

tion (ENSO) and the Asian summer monsoon.

In the third step, the impacts of volcanic eruptions and ENSO and their cooperative effects on the climate are obtained at a global scale and compared to the reconstructed data in East Asia. Volcanoes without ENSO events cause a global cooling and a non-significant El Niño-like warming in the tropical Pacific Ocean one year after the eruption. The following winter is warmer in Siberia and central Asia. The recovery times for the volcano induced-cooling (31 major eruptions averaged) vary globally between one and 12 years. In East Asia, the simulated temperature and drought index from E1 and E2 are compared with reconstructed data sets. Volcanoes without ENSO event in the following winter cause a dramatic cooling in West China and a drought in East China at the year one after the eruption. The reconstructed data show similar cooling patterns with smaller magnitudes in China, and similar droughts in East China. In both ensembles, there is no significant increase of El Niño events after volcanic eruptions. El Niño events in the winters after eruptions compensate the cooling in most regions of China (consistent with reconstructions), while La Niña events intensify the cooling. The simulated and reconstructed drought indices both show a tripole pattern disturbed by El Niño. The simulated impact of the eruption of the Tambora in 1815, which caused the 'year without summer' in 1816 in Europe and North America and a three-year famine in China, depends crucially on the ENSO state of the coupled model.

The Tibetan Plateau is the biggest and highest plateau in the world and has evident dynamic and thermodynamic effects on the general circulation and the climate in East Asia. Since the ALCC turns out to be one of the factors that cause the summer precipitation deficits in the Tibetan Plateau and in eastern China, the effects of surface albedo changes (one facet of the biogeophysical effect of ALCC) on the climate in the Tibetan Plateau is analyzed using a model of intermediate complexity, Planet Simulator. The experiments include one control simulation and two sensitivity experiments. The climate change in the Tibetan Plateau and its remote influence on the summer monsoon precipitation in eastern China are analyzed, and the underlying mechanism is discussed and compared to general circulation models.

Keywords: temperature, precipitation/drought index, volcano, ENSO, millennium, East Asia/China, simulation, reconstruction

List of Abbreviations

ACA	arid central Asia
AHFL	latent heat flux
AHFS	sensible heat flux
ALBEDO	surface albedo
ALCC	anthropogenic land cover change
APRC	convective precipitation
ASM	Asian summer monsoon
CC	cloud cover
DFA	detrended fluctuation analysis
EA	East Asia
EAMI	East Asian summer Monsoon Index
ENSO	El Niño/Southern Oscillation
EOFs	Empirical Orthogonal Functions
ESM	earth system model
EVAP	evaporation
GCM	general circulation model
IPCC AR4	Intergovernmental Panel on Climate Change the 4th Assessment Report
LIA	Little Ice Age
LTM	long term memory
MCA	Medieval Climate Anomaly
MELT	snow melt
MHI	Monsoon Hadley circulation Index
MIC	model of intermediate complexity
MW	Modern Warming
NAO	North Atlantic Oscillation
NE	Northeast
NW	Northwest
PC	principal component
PDSI	Palmer Drought Severity Index
ppb	unit: parts per billion
ppm	unit: parts per million
PRCP	total precipitation
PS	Planet Simulator
SE	Southeast
SNOW	snow depth
SPI	Standardized Precipitation Index
SR	net surface radiation (clear sky)
SR-c	net surface radiation
SRO	net top radiation (clear sky)
SRO-c	net top radiation

SSA	singular spectrum analysis
SST	sea surface temperature
SW	Southwest
TEMP	two meters temperature
TP	Tibetan Plateau
TR	net thermal radiation (clear sky)
TR-c	net thermal radiation
TSI	Total Solar Irradiance
WET	soil wetness
WNP	western North Pacific
YC	Yangtze Catchment

Chapter 1

Introduction

1.1 Motivation

Climate variability and climate change profoundly influence social and natural environments throughout the world with consequences for natural resources and society that could be large and far-reaching. For example, seasonal to interannual climate fluctuations strongly affect the success of agriculture, the abundance of water resources, and the demand for energy, while long-term climate change may alter agricultural productivity, land and marine ecosystems, and the resources that these ecosystems supply. During the past few decades, the Medieval Climate Anomaly (MCA), a supposed interval of elevated temperatures between approximately 900 and 1300 AD, has generated considerable interest due to its potential value as a 'natural' analogue of 20th century 'greenhouse' warming (or Modern Warming, MW) (Ge and Wu, 2011). Understanding and quantifying the past natural climate variability on decadal to centennial time scales is a pre-requisite to project future climate changes.

A high priority on identifying the confidence level in regional to hemispherical temperature changes during the past thousands years was placed by National Research Council of the National Academy (National Research Council: North et al. 2006) and the Fourth Assessment Report of the Intergovernmental Panel on Climate Change (IPCC AR4, Solomon et al., 2007, Ge and Wu, 2011). While many of these results show indications of notable climate shifts associated with the MCA, it is apparent that this period was characterized not by uniformly warmer temperatures, but rather by a range of temperature, hydroclimate and marine changes with distinct regional and seasonal expressions (Hughes and Diaz, 1994; Bradley, 2000;

Bradley et al., 2003). A huge number of previous studies on the temporal and regional expression of MCA for different parts of the world have been obtained and comprehensive reviews of those studies are obtained by Graham et al. (2011) and Diaz et al. (2011).

There are two effective ways to detect the climate variability: the reconstructed measures and model simulations. East Asia (EA) is one of the few regions in the world, which has almost all types of climate archives that could provide high-resolution proxy data, including the worlds longest continuous written historical records (Ge and Wu, 2011). Temperature time series of the last 500 to 2000 years have been reconstructed based on historical documents and natural archives (e.g., tree rings, ice cores, stalagmites, lake sediments) from China. EA has the strongest monsoon system in the world, the Asian monsoon system which has a strong sensitivity to the changes in all components of the climate system, and thus is characterized by large climate changes and enormous variability covering multi-millennial to intraseasonal timescales in the past (Lau et al., 2000; Wang et al., 2001; Ding et al., 2007, 2008). The local climate changes affect the life of nearly two-thirds of the global population (Clift and Plumb, 2008). Therefore, it is of essential importance to understand the main factors that could influence the climate system in EA and to investigate the fundamental mechanisms that determine the climate variability and changes in this region (Mann, 2002).

Causes for the reconstructed climate patterns and their changes are investigated with climate models and appropriate forcings (Bauer et al., 2003). The spectrum of climate models range from high-resolution General Circulation Models (GCMs)/Earth system models (ESMs) of intermediate complexity (EMICs) to energy balance models (EBMs). Coupled atmosphere-ocean GCMs support the importance of changes in insolation, volcanism, greenhouse gases and aerosols to simulate climate changes for important climatic periods (Shindell et al., 2004). The advantages of complex GCMs are their complete and dynamically consistent atmospheric and oceanic data sets and the assessment of the impact of different natural and anthropogenic forcings. The differences between millennium simulations are traced back to climate sensitivity, spin-up, and internal decadal variability (Goosse et al., 2005). Comparing model simulations with proxy-based climate reconstructions enables the possibility to understand and to explain mechanisms of climate variability, such as the MCA and the Little Ice Age (LIA). For instance, if a set of proxies indicate warm conditions in one region and other sets indicate wetter conditions in other regions for the same time period, climate simulations can provide clues about whether both types of climate conditions may be caused by large-scale atmospheric circulation patterns and are reasonable in terms of physical climatology (Zorita, 2012). Discrepancies between the simulations and reconstructions may also help to identify possible deficiencies in our understanding of past climate, its modeling or its representation by proxy records (González Rouco et al., 2011). Furthermore, a new focus is the spatial pattern of climate change, which provides a better understanding of past patterns of climate change (Fig. 1.1); and their causes may be even more important for validating the regional-scale pro-

jections, and therefore are paramount in assessing future climate change impacts (Mann et al., 2009).

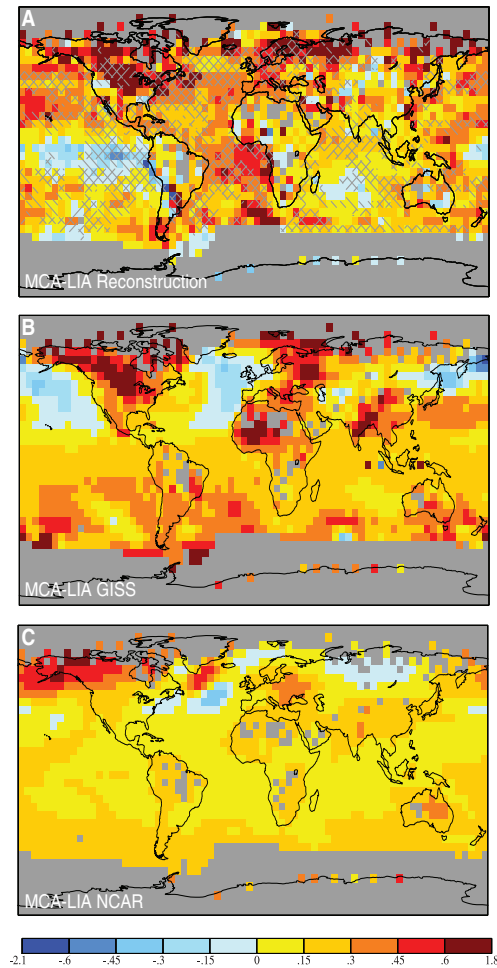


Fig. 1.1: Spatial pattern of the Medieval Climate Anomaly (MCA) minus the Little Ice Age (LIA) surface temperature difference [$^{\circ}\text{C}$] in reconstructions and model simulations. **(A)** Proxy-based temperature reconstructions (significant marked), **(B)** GISS-ER (using the same solar forcing difference as in the NCAR simulation—shown is the ensemble mean); and **(C)** NCAR CSM 1.4 simulation (Figure is from Mann et al. 2009, reprinted with permission from AAAS.)

1.2 Scope, objective and outline

The IPCC AR4 (Solomon et al., 2007) has provided a useful overview and assessment of paleo-climate data spanning different time periods, and its interpretation of possible causal mechanisms (Diaz et al., 2011). There are three sets of

mechanisms that have been proposed to account for pre-industrial multi-decadal to multi-century scale climatic variability: i) external forcing by, for example changes in solar irradiance (Ammann et al., 2007; Jungclaus et al., 2010), volcanism and atmospheric turbidity, ii) internal variability of the coupled ocean-atmosphere system, or iii) some combination thereof (Diaz et al., 2011). Therefore, the millennium experiments used in the present thesis are two ensembles forced by two different solar irradiance forcings including the most recent state-of-the-art forcing and a solar forcing with higher variability (see discussions in Jungclaus et al., 2010 and Schmidt et al., 2011). The ensemble members are forced by different initial conditions obtained from the control run and the ensemble spread (maximum and minimum anomalies in all members) are used as an assessment of the internal variability. Furthermore, in terms of greenhouse gases, the present model interactively calculates the carbon cycle within the submodel, while most of the other models incorporate prescribed values of CO₂ concentration. Similarly, the land cover changes before 1700 AD are incorporated only in our simulations as variations in vegetation types due to agricultural activities (Pongratz et al., 2008; Pongratz, 2009; Jungclaus et al., 2010).

The present thesis aims at investigating the climate variability in EA in the last 1200 years in terms of its spatial and temporal characteristics, to compare model results with proxy and historical documents, and to retrieve the underlying dynamical mechanisms. The model experiments include two full-forcings simulations: ensemble E1 (five members) forced by the state-of-the-art TSI reconstructed by Krivova et al. (2007, about 0.1% of the standard TSI value of 1367W/m⁻², given by the difference between present-day and Maunder minimum) and ensemble E2 (three members) forced by a TSI with higher variability by Bard et al. (2000, about 0.25%). The focuses lie on two climate variables, temperature and precipitation/drought index. The regional focus is given to EA, the highest and biggest plateau, the Tibetan Plateau, and the biggest river in terms of runoff volume in China, the Yangtze Catchment. The impacts of the most dominant forcing, volcanoes, as well as its cooperative effects with the important global climate phenomena El Niño/Southern Oscillation (ENSO), are discussed.

Pursuing these objectives, the present thesis is organized as follows:

Chapter 2

A mutual assessment of three reconstructed data sets and two simulated temperature, which is obtained from ensemble E1 and E2 forced by different solar forcings in China during the last 1200 years, is analyzed in Chapter 2 following a brief overview of the reconstructed temperature. A reconstructed data set and the simulated ensemble for weak solar forcing are selected for further analysis in terms of the regional climate anomalies and centennial spatial patterns in North-east, Southeast and West China. The uncertainty of the simulations is estimated by the ensemble spread which is a measure of the internal variability. We try to answer the following questions:

Q1: Are the Medieval Climate Anomaly (MCA)/Little Ice Age (LIA)/Modern Warming (MW) consistent in the simulated and reconstructed data? Which ensemble does the mutual assessment favor?

Q2: Are these climatic episodes spatially uniform? Are they consistent with reconstructed temperature in different regions?

Chapter 3

The precipitation variability in two full-forcings ensembles (E1 and E2) is analyzed in Chapter 3 and the results are compared with various reconstructed drought indices in China in the last 1200 years. The simulated drying trend in Northeast, Southeast and Southwest China, however, is not captured in the reconstructed data. In order to pursue the possible causes, single forcing experiments are adopted and the anthropogenic land cover change (ALCC) and fossil fuel CO₂ turn out to be the main factors. Furthermore, two Asian summer monsoon indices are retrieved for dynamical analysis. As for the hydrological cycle, a focus on the precipitation and runoff in the Yangtze catchment, its long-term variability and its relationship with ENSO, monsoon indices, and the snow cover on the Tibetan Plateau. We try to answer the following questions:

Q3: In control simulation, what are the variabilities of runoff and precipitation in the Yangtze catchment? What are the relationships with ENSO, the Asian summer monsoon system as well as the snow cover on the Tibetan Plateau?

Q4: What were the humidity conditions in China in the last 1200 years in the two full-forcings ensembles? Do different solar forcings show different trends and variabilities? Are they reconcilable with or are they captured in the reconstructed drought indices? What causes are responsible for the main trend in the simulated precipitation?

Chapter 4

Volcanoes turn out to be the dominant signal in the present millennium simulations. Volcanic eruptions and ENSO events can influence the climate on similar time scales and with comparable magnitudes. The combined signal can be greater in magnitude with different geographical patterns than suggested from a simple linear combination (Kirchner and Graf, 1995). Furthermore, an increase of the probability of El Niño events after volcanic eruptions is detected in reconstructions (Adams et al., 2003; McGregor et al., 2010) and simulations with the Zebiak-Cane model (Mann et al., 2005; Emile Geay et al., 2008). In EA, this impact is highly relevant since the ENSO is related to drought during El Niño and wetness during La Niña phases, thus both phenomena can lead to either a partial cancellation or to an enhancement with even more disastrous consequences. The present two ensemble simulations with eight members in total (five for ensemble E1 and three

for ensemble E2) enable the analysis of the volcanic and ENSO impacts as well as their co-operative effects.

The impacts of volcanic eruptions and ENSO and their co-operative effects on the climate in EA is analyzed in Chapter 4. The global climate response patterns and the relaxation time scales are first determined for the eruptions without ENSO out of 21 most intense eruptions in each member. The precipitation anomalies are analyzed in terms of the Standardized Precipitation Index (SPI). The simulated temperature and SPI anomalies are compared with reconstructed temperature and drought indices in EA in terms of: i) volcanic eruptions without ENSO events, ii) ENSO effects without preceding eruptions and iii) cooperative effects of eruptions and ENSO. We try to answer the following questions:

Q5: What are the volcanic impacts at a global and regional scale? How does the recovery of the temperature decay proceed and what time scales do they have? Is there winter warming and are they comparable with observations?

Q6: Do volcanoes cool/dry East Asia? Are they uniform in East Asia and are they consistent with reconstructed data?

Q7: Do eruptions increase the probability of El Niño events? When there are ENSO events in the following winter, how does the climate in East Asia respond compared to eruptions without ENSO events? Are the results consistent with proxy data?

Q8: What was the climate in East Asia after Tambora eruption? What was the ENSO state in history? Would the climate be different in East Asia if the ENSO state were different?

Chapter 5

The Tibetan Plateau is the biggest and highest Plateau in the world. It is of outstanding relevance for the atmospheric circulation. In particular, it has evident dynamic and thermodynamic effects on the general circulation and the climate in EA (Yao et al., 1996; Wang et al., 2007a, 2008; Yang et al., 2008; Bothe et al., 2011; Zhu et al., 2011). The warming and rainfall deficits detected in the general comprehensive model ECHAM5 in the last century are plausibly caused by the ALCC and the rising greenhouse gases. Meanwhile, the increasing temperature in the Tibetan Plateau and the rainfalls in eastern China (Wang et al., 2008) may be physically linked (Wang et al., 2008). Therefore, we aim to analyze the effects of ALCC in terms of surface albedo change on the climate variability in the Tibetan Plateau and its influence on the summer monsoon precipitation in eastern China. A model of intermediate complexity, Planet Simulator, is used due to its attractiveness in the fast diagnostic compared to GCMs with large amounts of components and interactions. One control run and two sensitivity experiments are performed in T42 resolution and the results are compared to GCMs in Chapter 5. We try to answer the following questions:

Q9: How do temperature and precipitation respond when the surface albedo

increases/decreases on the Tibetan Plateau? Would the climate changes in Tibetan Plateau increase the summer monsoon precipitation in eastern China?

Q10: What are the dynamical mechanisms behind? Is Planet Simulator, a model of intermediate complexity, able to capture what GCMs exhibit?

Chapter 6 contains the summary and discussion. The main findings of the thesis are highlighted.

The work presented in Chapter 2, Chapter 3 and Chapter 4 have been published (Zhang et al., 2010; Blender et al., 2011; Zhang et al., 2011). Sections in Chapter 4 has been accepted as separate journal publications (Zhang et al., 2012).

Chapter 2

Temperature variability in simulations and reconstructions

2.1 Introduction

Knowledge of past climate evolution is essential for understanding natural climate variability. Information on the climate during the last millennium is known from reconstructions using proxy data and simulations with Earth System Models (ESMs). The variability of the Northern Hemispheric climate during the last millennium is commonly characterized by multi-century episodes with distinct temperature and humidity anomalies: the Medieval Climate Anomaly (MCA, approximately 900-1300 AD), the Little Ice Age (LIA, approximately 1300-1850 AD) and the Modern Warming (MW, beginning in the 19th century). Due to substantial regional deviations these climatic periods are not uniquely defined and describe a simplified view of past climate in the Northern Hemisphere (see Jones and Mann, 2004 and Jungclauss and the COMSIMUM Team, 2009 for a review).

In China, these main climatic episodes are confirmed by temperature reconstructions (Wang et al., 1991; Yang et al., 2002; Ge et al., 2006, 2007; Wang et al., 2007b; Qian et al., 2008; Yang et al., 2009). Regional reconstructions are available for East China (Liu et al., 2005b; Peng et al., 2009), West China (Holmes et al., 2009), the Yellow river and the Yangtze catchment (Ge et al., 2003; Zhang et al., 2008b) and the Tibetan (Yang et al., 2003). Using proxy data in 10 regions in China, Wang et al. (2007b) claimed that the mean temperature in China varied in a range of about 1°C during the last 1000 years. After 1400 AD, temperature

decreased with mean temperatures 0.6-0.9°C below present-day (Ge et al., 2003). Climate oscillations are found by Wang et al. (1991) in the annual mean temperature with periods of 200, 80, 30, and 22 years, which can be identified with the solar deVries (200-yr), Gleissberg (80-yr) and Hale cycles (22-yr) (for an overview see Tsiropoula, 2003).

Several ESMs used for millennium simulations include a simplified atmosphere, for example simple energy balance models (Crowley et al., 2003), models without explicit atmospheric dynamics (CLIMBER, Bauer et al., 2003), or a quasi-geostrophic atmosphere (ECBILT-CLIO-VECODE, Goosse et al., 2005). Complex ESMs simulate a coarse resolution dynamic atmosphere, the majority in T31 ($\approx 3.75^\circ$), for example CCSM2.01 (National Center for Atmospheric Research, NCAR, Ammann et al., 2007 and Peng et al., 2009), GISS-ER (Goddard Institute for Space Studies-ER, Mann et al., 2009), and ECHO-G (ECHAM4/HOPE-G, Max-Planck Institute for Meteorology, Zorita et al., 2004 and Liu et al., 2005b).

The advantages of complex ESMs are complete and dynamically consistent atmospheric and oceanic data sets and the assessment of the impact of different natural and anthropogenic forcings. The differences between millennium simulations are traced back to climate sensitivity, spin-up, and internal decadal variability by Goosse et al. (2005). Discrepancies between global reconstructions and two model simulations for the MCA-LIA difference were interpreted in terms of teleconnection patterns by Mann et al. (2009). The comparison of simulated data obtained by dynamical ESMs with reconstructed data is necessary for the following reasons:

(a) Boundary conditions. Simulated climate variability depends to a large degree on the quality of reconstructed boundary conditions used in the model. One of the most important forcings is the solar irradiance for which the recent reconstruction by Krivova et al. (2007) assumes a smaller magnitude of variations than previous reconstructions (for example Bard et al., 2000). The model output can be used to validate the reconstructed forcings.

(b) Reconstruction deficits. Reconstructed data suffer from several shortcomings: they depend to a large degree on statistical approaches and are possibly not dynamically consistent, the spatial coverage and the information are incomplete, and the uncertainty is poorly known. Model data can be useful to benchmark contradicting reconstructions.

Thus, the mutual assessment of dynamical earth system models and reconstructions is useful for the understanding of climate variability and the development of reliable models.

The aim of this chapter is to derive the temperature variability in East Asia during the last 1200 years on a regional basis. The analysis includes two simulated ensemble mean temperature data sets in China as well as three reconstructions. The simulated data are from two full-forcings ensembles for 800-2005 AD using the complex atmosphere-ocean general circulation model ECHAM5/MPIOM/JSBACH forced by the state-of-the-art solar forcing reconstruction from Krivova et al. (2007) and a forcing reconstruction with higher variability from Bard et al. (2000), denoted

as ensemble E1 (five members) and E2 (three members), respectively. The uncertainty of the simulations is estimated by the ensemble spread which is a measure of the internal variability.

This chapter is organized as follows: Section 2.2 describes the model and simulations, the forcings and the reconstructed data. Section 2.3 gives a brief overview of the reconstructed temperature in China during the last 1200 years, and Section 2.4 describes the simulated temperature variability in Northern Hemisphere in the last 1200 years. Section 2.5 begins with a mutual assessment between two ensemble simulations with three reconstructions, which resulting a reconstructed data set and the simulated ensemble selected for further analysis in terms of the regional climate anomalies and centennial climate anomaly patterns. The results are summarized and discussed in Section 2.6.

2.2 Data and methods

Model components and forcings

The millennium experiments are carried out using the COSMOS-Atmosphere-Surface (Land)-Ocean-Biogeochemistry Earth System Model (Jungclaus, 2009; Jungclaus et al., 2010). The model includes the atmospheric model ECHAM5 (Roeckner et al., 2003), the ocean model MPIOM (Marstrand et al., 2003) and modules for land vegetation JSBACH (Raddatz et al., 2007) and ocean biogeochemistry HAMOCC (Wetzel et al., 2006), which are coupled via the OASIS3 coupler. ECHAM5 is run at T31 resolution ($\approx 3.75^\circ$) with 19 vertical levels, and MPIOM at a horizontal grid spacing of about 3° with 40 unevenly spaced vertical levels. CO_2 is interactively transported in the atmosphere and the ocean. The atmospheric concentration was initially set to 278ppm derived from the Law Dome ice core for the year 800 and reached a value of about 281ppm which was used at the start of the control run.

The model is forced by reconstructions of (I) Total solar irradiance (TSI), (II) volcanic forcing considering aerosol optical depth (AOD) and effective radius distribution, (III) land use change, and (IV) anthropogenic green house gases and aerosols.

(I) Two solar forcings are used to conduct two full-forcings ensembles. The first TSI is based on the state-of-the-art solar forcing data reconstructed by Krivova et al. (2007) (see Jungclaus et al., 2010, for a discussion). It combines sun-spot observations starting back in the 17th century and variations of atmospheric C^{14} -concentrations derived from tree-rings. The time series exhibit low long-term variability of about 0.1% of the standard TSI value of 1367W/m^{-2} (given by the difference between present-day and Maunder minimum), therefore it is denoted as weak solar forcing. The second TSI is based on Bard et al. (2000) which has a higher variability of 0.25% and is denoted as strong solar forcing.

(II) The volcanic effects are taken into account in a data set of Aerosol Optical Depth (AOD) at $0.55 \mu\text{m}$ and effective radius for 10-day time steps and split into four equal area segments ($30\text{-}90^\circ\text{N}$, $0\text{-}30^\circ\text{N}$, $0\text{-}30^\circ\text{S}$, $30\text{-}90^\circ\text{S}$). Growth and decay time for each eruption is calibrated and fitted to recent observations. The data set includes information about mean particle radius evolution vs. time, a feature particularly important for large eruptions (for details see Crowley et al., 2008 and Timmreck et al., 2009) have shown for the 1258 eruption that a shift of the volcanic aerosol size distribution towards larger particles reduces the cooling effect and improves the consistency with temperature reconstructions.

(III) The anthropogenic land cover change (ALCC) prior to 1700 is reconstructed by Pongratz et al. (2008) and after 1700 by Foley et al. (2003). In China where crop areas were already large at 800 AD, natural vegetation is almost completely replaced by agricultural land use after 1700 in Southeast China. In the present simulations, the reconstructed ALCC is considered by applying the reconstruction of global agricultural areas and land cover, and the reconstruction merges published maps of agriculture from 1700 to 1992 AD and a population-based approach to quantify agriculture from 800 to 1700 AD (see more details in Pongratz et al., 2008; Jungclaus et al., 2010).

(IV) The carbon cycle is interactively simulated. For 1860-2000 regional fossil fuel CO_2 emissions are from Marland et al. (2003). For 2001-2100 global CO_2 emissions are adopted from the SRES A1B scenario (IPCC AR4, Solomon et al., 2007) and distributed proportional to the regional emissions (Marland et al., 2003) in 2000. All these fossil fuel CO_2 emissions are allocated within the regions proportional to population density (Goldewijk, 2005). Atmospheric CH_4 (650ppb) and N_2O (270ppb) concentrations for the year 800 were derived from ice core measurements at Law Dome, Antarctica (Meure et al., 2006).

Simulated data

The simulated data are from two full-forcings ensembles (see Table 2.1): ensemble E1 with five members (10, 12, 13, 14 and 15) forced by the state-of-the-art solar forcing data from Krivova et al. (2007) and ensemble E2 with three members (21, 25 and 26) forced by a strong solar forcing from Bard et al. (2000) (see (I) above). The remaining natural and anthropogenic forcings are identical; the whole experiments cover the period from 800 to 2005 AD (Bard et al., 2000; Jungclaus et al., 2010). The different initial conditions for the ensemble members are derived from a 3000-year control integration.

China has an area of 10^6km^2 and is approximated by the model area extending from $70^\circ\text{-}130^\circ\text{E}$ and $17.5^\circ\text{-}55^\circ\text{N}$; for a comparison with reconstructed temperature, China is divided in three regions: Northeast (NE), Southeast (SE), and West (W) China (Fig. 2.1).

All anomalies are calculated with respect to the time means which are determined individually for each ensemble member in the whole period 800-2005 AD.

Table 2.1: List of the millennium experiments used in the present chapter carried out with ECHAM5/MPIOM/JSBACH at T31 resolution.

Experiment ID	Description	Years
01	Control run	800-3800
10, 12-15	Ensemble E1: full-forcings experiment members 1-5	800-2005
21, 25-26	Ensemble E2: full-forcings experiment members 1-3	800-2100

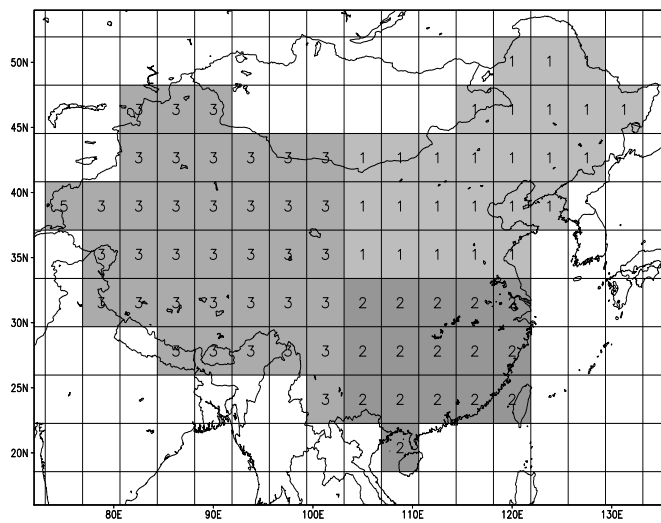


Fig. 2.1: Research regions in China: (1) Northeast (NE) China, (2) Southeast (SE) China, (3) West (W) China marked in grid cells in the ECHAM5 T31 model simulation ($\approx 3.75^\circ$).

Reconstructed data

The reconstructed temperature time series in the last millennium used in the present analysis are from Yang et al. (2002), Ge et al. (2003), and Wang et al. (2007b) (see Section 2.3 for a overview on reconstructed temperature in China).

The temperature from Yang et al. (2002) is reconstructed in China for 800-1999 AD with 10-yr resolution (the whole original period 0-1999 AD) based on ice core, tree rings, peat and lake chronologies, biota and other climate indices (Yang et al., 2002).

The winter half-year (October to April) from Ge et al. (2003) is reconstructed over eastern part of China with 30-yr resolution for 800-1999 AD (10-yr resolution in 960-1100 AD, the original period is from 15-1999 AD) using the phenological cold/warm events recorded in Chinese historical documents (Ge et al., 2003).

The temperature from Wang et al. (2007b) is reconstructed for ten regions in China with 10-yr resolution spanning the time 1000-2005 AD using a variety of

proxy data, such as ice cores, tree-rings, stalagmites, peat, lake sediments, pollen and historical records validated with instrumental observations. It presents a detailed regional temperature reconstruction in Northeast, North, East, South China, Taiwan, Central, Southwest, Northwest China, Xinjiang, and Qinghai-Tibet Plateau (Wang et al., 2007b).

Power spectrum analysis

Long term memory is determined by power spectra. In the last years several investigations could show that inter-annual temperature variability is dominated by power-laws, $S(f) \sim f^{-\beta}$ in wide ranges of time scales (Fraedrich and Blender, 2003; Huybers and Curry, 2006). Thus, climate variability is present on all time scales with a continuous background superimposed with oscillations or cycles. For positive exponents, $\beta > 0$, this long-term memory is explained by the thermal inertia of subsystems, mainly the ocean. Long-term memory is also found in a long-term simulation of the hydrological cycle with the coupled model ECHAM5/MPIOM in China (Blender and Fraedrich, 2006). The exponent β is determined by detrended fluctuation analysis (DFA, Hurst exponent $\alpha = 0.75$, Fraedrich and Blender, 2003).

2.3 Reconstructed temperature in East Asia

The dominant climate variability observed in the Northern Hemisphere is confirmed by temperature reconstruction in China (see for example, Yang et al., 2001, 2002; Wang et al., 2007b). Data in the western part of China and on the Tibetan plateau are documented by Ge et al. (2006), Holmes et al. (2009), and Zhang et al. (2009). Ge et al. (2003) and Zhang et al. (2008b) derived the winter temperature in eastern China with emphasis on the Huang He (Yellow River) and the Yangtze catchment. An outstanding deviation from the mean temperature in China is the absence of a distinct warming during the MCA in West China (Ge et al., 2006), instead, Xinjiang and the Qinghai-Tibet Plateau experienced a cold phase during the eleventh century (Wang et al., 2007b). The temperature reconstructions in China during the last two millennia (Ge et al., 2010) reveal high consistency after 1500 AD for the five regions assessed (Northeast, Northwest, Southeast, Central East, and Tibet), whereas prior to 1500, large inconsistencies are found.

The reconstructed temperature anomalies during the last 1200 years in the three regions, West (W), Northeast (NE) and Southeast (SE) China (Fig. 2.1) are summarized in Table 2.2: in 800-1000 AD data of Ge et al. (2003) and Yang et al. (2002) are used, after 1000 AD this follows Wang et al. (2007b). The Table shows three classes for the absolute anomalies: weak ($<0.2^{\circ}\text{C}$), moderate ($0.2\text{-}0.5^{\circ}\text{C}$), and large amplitudes ($>0.5^{\circ}\text{C}$). The chronology is given by centennial means during three major climatic epochs, the MCA (900-1300 AD), the LIA (1300-1850 AD), and the MW (after 1900 AD). The temperature during the 20th century was comparable to that in the MCA in East China.

Table 2.2: Summary of reconstructed centennial regional temperature anomalies [$^{\circ}\text{C}$] in China in 800-2000 AD.

	Years	China	Northeast	Southeast	West
MCA	800-900	3	1	1/-2	1
	900-1000	2	2	2/-1	1
	1000-1100	-1	2	1	-2
	1100-1200	1	2	1	-1
	1200-1300	1	3	1	-1
LIA	1300-1400	-1	3	1	-2
	1400-1500	-1	-1	-1	-1
	1500-1600	-1	-2	-1	-1
	1600-1700	-2	-2	-1	-2
	1700-1800	-1	-2	-1	1
MW	1800-1900	-1	-1	-2	2
	1900-2000	2	1	2	3

2.4 Northern Hemisphere

In the control run there is no external forcing variability and the orbital parameters are fixed to those for the year 800. The 2000-year integration shows that the model exhibits a stable climate and compares well with other pre-industrial control integrations. European temperatures from the model agree well with the 500-year reconstruction of Luterbacher et al. (2004) (see project descriptions from Millennium group, 2012).

In the full-forcings simulation (ensemble E1), the comparison of the impact of different forcing mechanisms in the millennium experiments (Jungclaus et al., 2010) yields that the variability is dominated by volcanic eruptions decreasing the net short wave radiation at the top of the atmosphere (Fig. 2.2a, incoming TSI reduced by cloud and aerosol reflection). The most severe eruption occurred in 1258 (Stothers, 1984), presumably in the lower latitudes, and the second most severe was the Tambora eruption in 1815. The Maunder minimum of solar activity (1645-1715) is barely detectable while the Dalton minimum (1790-1830) coincides with a series of volcanic eruptions (Cole Dai et al., 2009).

The ensemble mean (E1) of the Northern Hemispheric mean surface temperature (Fig. 2.2b) shows distinct long-term climate anomalies. Decadal cooling periods are found after volcanic eruptions in 1258 (unknown volcano) and 1815 (Tambora) respectively, the latter period coincides with the Dalton minimum (1790-1830). A warm period in 1100-1200 may be associated with the MCA, and an intermittent cool period during 1400-1700 corresponds to the little ice age (LIA). After 1900 the modern warming (MW) commenced. The cooling of -0.1°C during the LIA in the Northern Hemisphere is much less pronounced than the reconstructed range, between -0.6 and -0.3°C (Mann et al., 2008). Volcanic eruptions are the

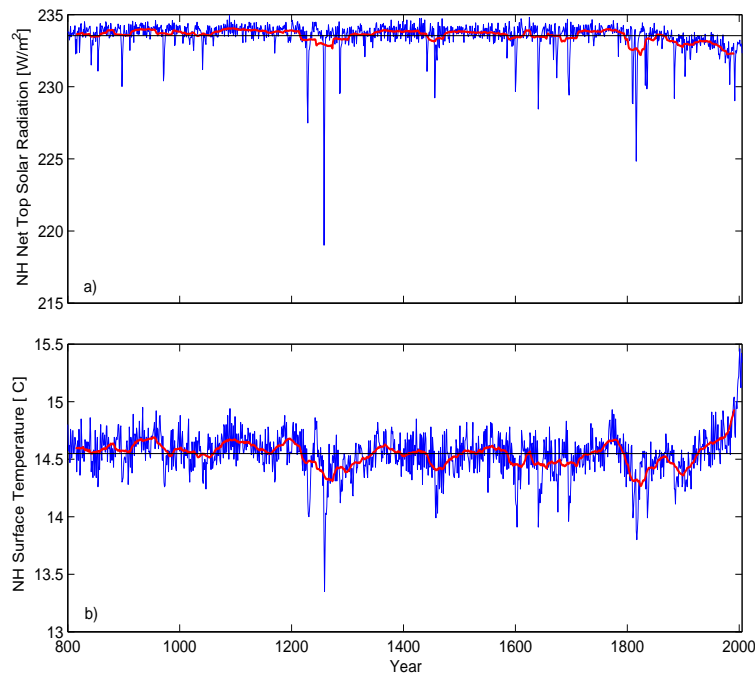


Fig. 2.2: Northern Hemispheric annual means (blue) of (a) net shortwave radiation at the top of the atmosphere [W/m^{-2}] and (b) surface temperature [$^{\circ}\text{C}$] in ensemble E1. 30-year running means are indicated (red).

most efficient impacts on surface temperature during the pre-industrial era.

The present simulations represent an overall warmer MCA and a cooler LIA at global and hemispherical scales in both ensembles as a response to long term changes in volcanic activity and solar irradiance (Fig. 2.3). Ensemble E1 with the weak solar forcing has smaller amplitudes of cooling than E2 with the strong solar forcing, and it has more regional widespread cooling, including parts of Southern Ocean, Atlantic Ocean, North America and west India Ocean. It is a sign of the lower weight of TSI changes that allows the internal variability to be more prominent (González Rouco et al., 2011). Meanwhile, these regional features may be related to the different initial conditions used for each member (Fig. 2.4).

Similarly, most of the models in IPCC-AR4 (Solomon et al., 2007) tend to produce a similar warmer MCA in Northern Hemisphere (NH), which were performed with a comparatively high solar variability scenario (see González Rouco et al., 2011). Only the present model has two different ensembles that were forced by small (E1) and large (E2) irradiance. In terms of greenhouse gases, all models incorporate prescribed values of CO_2 concentration except for the present model, which interactively calculates them within the carbon cycle submodel. Similarly, land use changes before 1700 AD are incorporated only in our simulations as variations in vegetation types due to agricultural activities (see (III) and (IV) in Sec-

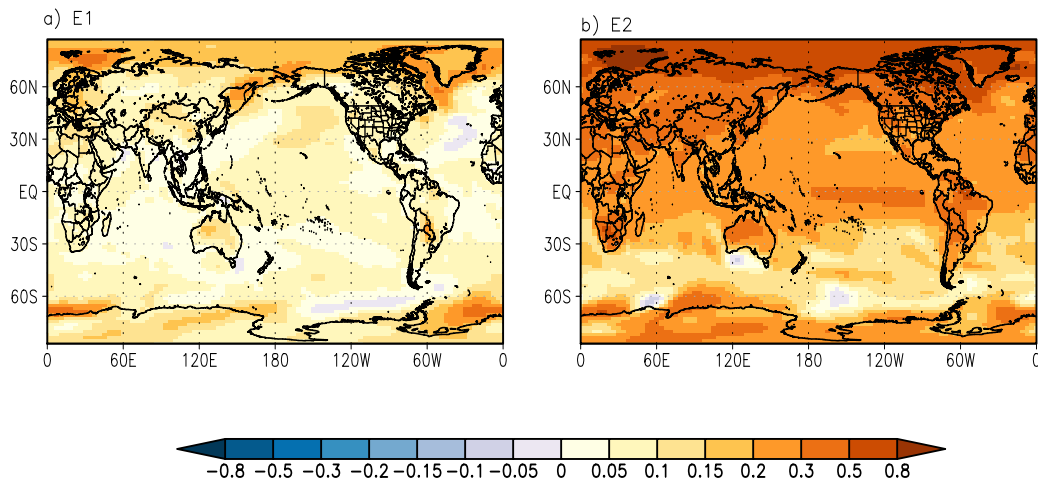


Fig. 2.3: Annual mean temperature difference [$^{\circ}\text{C}$] of the Medieval Climate Anomaly (MCA) minus the Little Ice Age (LIA, approximately 950-1250 AD minus 1400-1700 AD) in ensemble (a) E1 and (b) E2.

tion 2.2, Pongratz et al., 2008, Pongratz, 2009 and González Rouco et al., 2011). The amplitude of the warmer response, however, is dependent on the specific set of forcing reconstructions used to drive the simulations. Compared to the reconstructed data by Mann et al. (2009), the models results are better in the Northern Hemisphere than in the Southern Hemisphere, even though none of them reproduces the La Niña-like cooling in the Pacific Ocean (González Rouco et al., 2011).

2.5 Mutual assessment between simulations and reconstructions

The three reconstructed near surface temperature data sets are compared with two simulations obtained for different solar forcing in order to select a reconstruction and a simulated data set which agree within an uncertainty given by the internal climate variability. This mutual assessment, which is based on the mean temperature in China, includes a spectral analysis to validate the data using information on low frequency variability detected in previous analyses. Furthermore, the analysis includes a comparison of regional climate anomalies in China in the selected reconstructed and simulated data sets.

- **Mutual assessment of solar irradiance forcings and different reconstructions**

Two ensembles forced by weak and strong solar irradiance (see Section 2.2) are included and both are compared with three reconstructed data sets (Ge

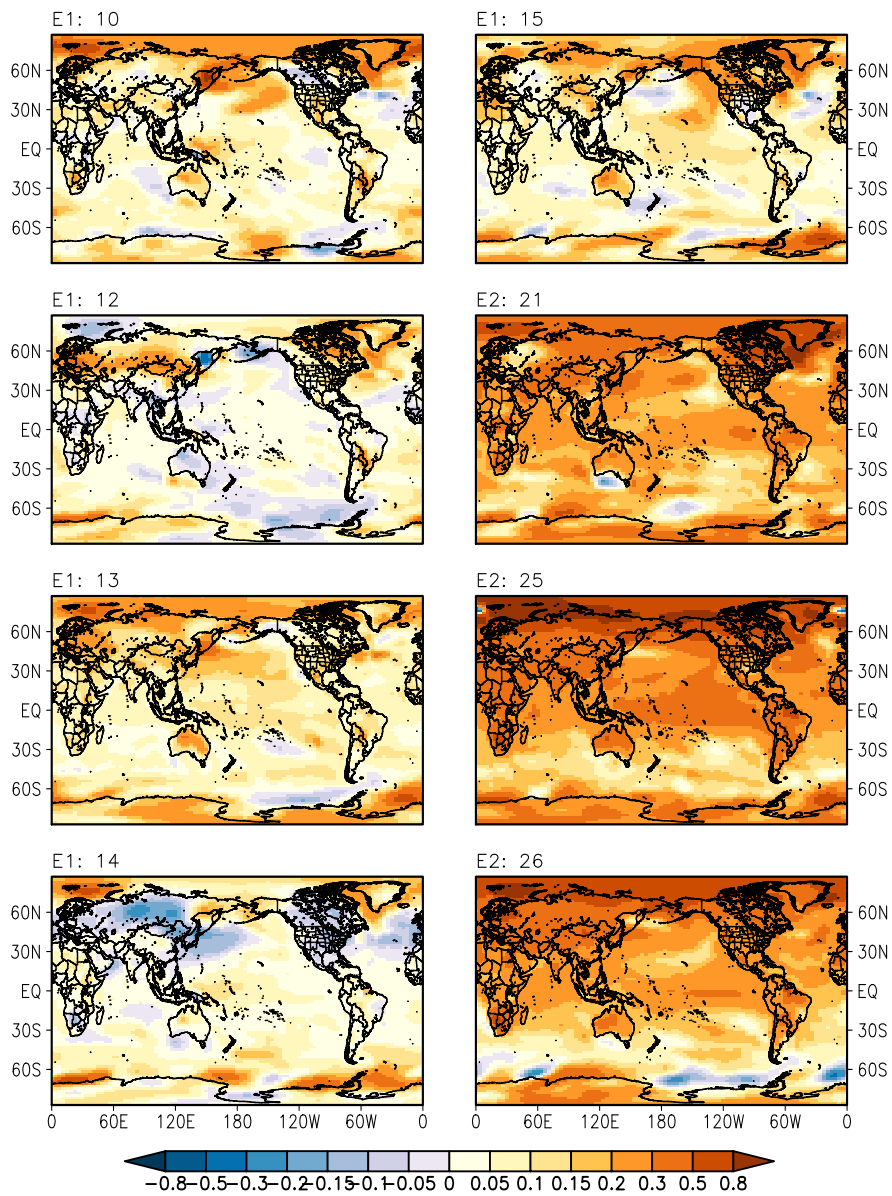


Fig. 2.4: As Fig 2.3 for each ensemble member E1: 10, 12-15, and E2: 21, 25 and 26. Experiment details see Table 2.1.

et al., 2003; Yang et al., 2002; Wang et al., 2007b). The comparison which includes a spectral analysis yields considerable differences between reconstructed data and gives some hints to the assessment of the forcing.

- **Regional temperature anomaly and ensemble spread**

For a comparison with reconstructions China is divided in three regions (Fig.

2.1): Northeast, Southeast, and West China. The uncertainty of the ensemble experiments is derived by the spread of temperature extremes on decadal time scales. The time series are compared with reconstructed data.

- **Centennial temperature anomaly patterns and annual cycle**

For a detailed geographical comparison the time span of the model simulation is split into bi-centennial time bins beginning with the 9th century up to present-day. Particular periods are assessed for a comparison with the climatology merged by Wang et al. (2007b). The model results are used to retrieve the change of the annual cycle during the past 1200 years.

2.5.1 Solar forcings and different reconstructions

Three reconstructions of the mean temperature in China are compared with the ensemble means in simulations which differ with respect to the variability of the solar forcing (Fig. 2.5). The reconstructed temperature anomalies by Yang et al. (2002) (decadal means in China), and Ge et al. (2003) (30 years winter means in East China with decadal means in 960-1100 and after 1500) show large centennial variability of the order of 1°C which are far beyond the reconstructions by (Wang et al., 2007b) (decadal means after 1000 AD) as well as the model uncertainty. For example in Yang et al. (2002) the mean temperature in 800-900 is 0.6°C and shows -0.6°C in 1400-1700. In Ge et al. (2003) the temperature anomaly reaches more than $\pm 1^{\circ}\text{C}$ for decades in the 13th century and falls below -0.6°C in 1800-1900. The mutual comparison of the simulated and the reconstructed data indicates that the reconstructions by Wang et al. (2007b) are reconcilable with the simulations.

The variability of this data (standard deviation 0.27°C), however, is too large to provide an assessment of both simulations. Ensemble E1 with strong solar forcing reveals larger anomalies and in particular a warmer MCA (0.1°C) and a cooler LIA (-0.07°C) compared to ensemble E1 with weak solar forcing. Compared to the 1960-90 mean, the Maunder minimum (1645-1715) is -0.34°C (-0.35°C) colder in ensemble E1(E2). Therefore, based on the data by Wang et al. (2007b) we cannot decide whether ensemble E2 with higher solar variability is preferable to ensemble E1 with weak solar variability.

Since reconstructed and simulated data indicate considerable differences in low frequency variability (Fig. 2.5), the comparison is complemented by spectral analysis (method see Section 2.2). The simulated temperature (with annual resolution) shows a nearly continuous power-spectrum with an exponent $\beta \approx 0.5$, which is valid in the whole accessible frequency range from annual to several centuries (Fig. 2.6a). The single deflection is an increase in power within the frequency range corresponding to 3-4 years which can be attributed to El Niño/Southern Oscillation (ENSO). Further periodic or quasi-periodic variability contributions are not simulated (see for example Wang et al., 1991). Ensemble E2 with the higher solar irradiance variability (0.25%, not shown) reveals a power-spectrum with the same scaling and exponent. Note that in instrumental records and long-term simulations

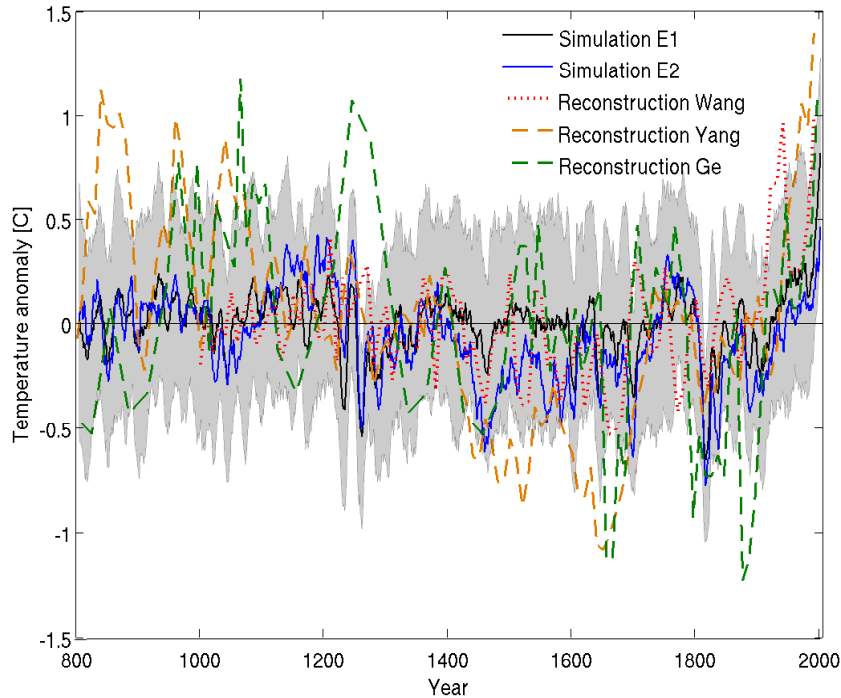


Fig. 2.5: Temperature anomalies [$^{\circ}\text{C}$] in China from simulations and reconstructions: ensemble E1 (black/solid) and E2 (blue/solid), and reconstructions by Wang et al. (2007b, dotted/red), Yang et al. (2002, dashed/brown), and Ge et al. (2003, dashed/green). The ensemble spread (from ensemble E1) is indicated by the 11-year running means of simulated minimum and maximum anomalies in the ensemble (grey/shaded).

smaller values of $\beta \approx 0.2 \dots 0.4$ are found on land on time scales up to centuries (Fraedrich and Blender, 2003). In climate simulations long-term memory is caused by dynamic ocean models which show a variety of spectra (Zhu et al., 2006).

The power-spectrum of the reconstructed decadal mean temperature (Wang et al., 2007b) shows scaling with the same exponent $\beta \approx 0.5$ (Fig. 2.6b). Thus, the simulated and the reconstructed temperature time series indicate the same type of long term memory. The power-spectra of the reconstructed temperature time series proposed by Yang et al. (2002) and Ge et al. (2003) (Fig. 2.6c) confirm the high low frequency variability observed (Fig. 2.5). Both spectra increase steeply for low frequencies with a spectrum that can be roughly estimated as $S(f) \sim 1/f^2$, hence $\beta \approx 2$. This result provides further evidence that the reconstruction by Wang et al. (2007b) is in agreement with the model simulation. In summary, we conclude that given the reconstruction of the solar irradiance with 0.1% variability (in ensemble E1) is considered as a state-of-the-art (Krivova et al., 2007; Jungclaus et al., 2010), there is no need to deviate from this suggestion and that this forcing intensity, i.e., ensemble E1 is appropriate for millennium simulations.

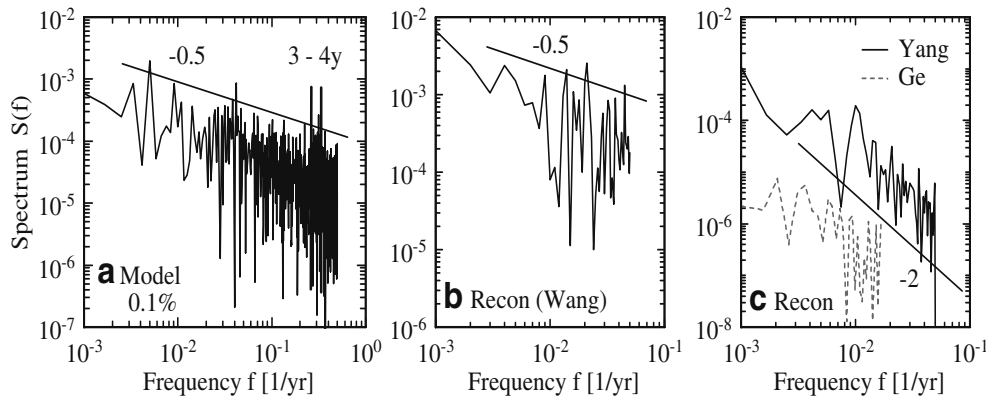


Fig. 2.6: Power spectra of the mean temperature in China: (a) simulation (ensemble E1 with weak solar irradiance), (b) reconstruction by Wang et al. (2007b), and (c) reconstruction by Yang et al. (2002, solid) and Ge et al. (2003, dashed). In (a) the 3-4 year ENSO cycle is marked.

2.5.2 Regional anomaly and ensemble spread

Temperature time series for China and three regional averages (Northeast, Southeast and West) are compared with the reconstruction by Wang et al. (2007b). The uncertainty of the simulation is estimated by the minima and maxima in the 5-member ensemble. The mean temperature in China (Fig. 2.7a) is above normal in 900-1200 and below average during 1200-1300 and 1800-1900 AD. An anomalously cold and persistent LIA is hardly distinguishable. This is comparable to the simulation by Peng et al. (2009). The cool periods during the 13th and the 19th centuries are associated with sequences of the most intense volcanic eruptions in 1258 and in 1815 (Tambora). After that, the cold temperature anomalies recover on decadal time scale, which is attributed to the ocean heat uptake in a coupled ensemble experiment (Stenchikov et al., 2009).

According to Cole Dai et al. (2009) 1810-1819 was the coldest period during the last 500 years. A short cooling period appears at the end of the 19th century which is most dominant in the Northeast (Fig. 2.7b). A possible reason for this cooling is a sequence of volcanic eruptions (Krakatau in 1883, Santa Maria and Mount Pelée in 1902, and Novarupta in 1912). The Maunder minimum in 1645-1715 is related to a centennial period with a weak cooling while the Dalton minimum in 1790-1830 is marked by a strong cooling for roughly two decades. The dominant temperature change occurs during the Modern Warming (MW) in the 20th century.

Regional averages of temperature in Northeast, Southeast and West China reveal major consistent long term anomalies determined with respect to the total simulation period (Fig. 2.7b-d). All regional temperature anomalies vary within a corridor of $\pm 0.5^\circ\text{C}$. The differences between regional temperatures, however, are much

weaker than between reconstructed anomalies. The most remarkable differences are in the Northeast with a distinct reconstructed warming in 1000-1400 AD and a cooling from 1400-1800 AD; but much weaker anomalies are found in the Southeast. The reconstructed temperature anomalies in the Northeast are characterized by centennial variability, whereas decadal variability dominates in the West.

As summarized in the Section 2.5.1, although that the ensemble E1 is chosen for its representance as a state-of-the-art, the results from ensemble E2 reveal importance to account for uncertainty of the amplitude in solar forcing (Fig. A.1 in Appendix). Distinct regional dissimilarities in reconstructions are not detected in ensemble E2 either, however, the simulated temperature anomalies have better agreements in NE China where there is a distinct MCA and LIA in reconstructions. This is an obvious response to the solar irradiance with higher variability (about 0.25% in ensemble E2 and 0.1% in ensemble E1, see Section 2.2). In SE China, the reconstructed temperature anomalies are at the lower threshold of the ensemble spread in LIA. This again confirms that the anomalies during the relevant

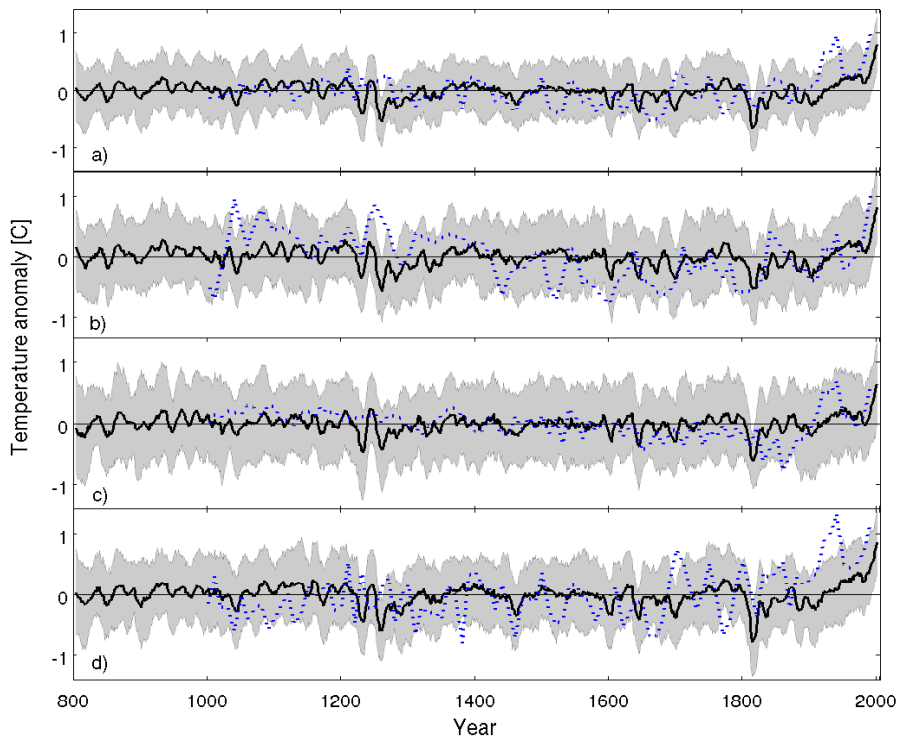


Fig. 2.7: Temperature anomalies [$^{\circ}\text{C}$] in (a) China, (b) Northeast China, (c) Southeast China, and (d) West China from simulations and reconstructions: ensemble E1 (black/bold) and ensemble spread (grey/shaded) as 11-year running means of minimum and maximum; Reconstructions (blue/dotted) by Wang et al. (2007b). Simulated (reconstructed) anomalies are with respect to the 800-2005 (1000-2000) mean.

climatic periods are largely influenced by the internal variability (González Rouco et al., 2011)

2.5.3 Centennial anomaly patterns and annual cycle

In this section, the simulated ensemble mean is first compared with the reconstructed temperature anomalies patterns for periods given by Wang et al. (2007b), which is complemented by a bi-centennial decomposition of temperature anomalies during 800-2000 AD.

Comparison with centennial temperature reconstructions

Wang et al. (2007b) present a geographic overview of climate anomalies for the last millennium considering distinct periods: (a) 1041-1140, (b) 1171-1270, (c) 1601-1700, (d) 1781-1880, and the shorter periods (e) 1951-2000, and (f) 1991-2000. This summary of long-term mean temperatures is an apt compilation for the assessment of the simulation. For ease of the comparison the anomalies of the near surface temperature are determined for the corresponding periods (all anomalies are relative to the mean in the total range 800-2005). The main findings are summarized as follows (Fig. 2.8, compare Fig. 5 in Wang et al., 2007b and Fig. 2 in Mann et al., 2009):

(a) 1041-1140: The model shows a moderate warming of the order of 0.1°C for East Asia, whereas in the reconstructions, the western part is colder than average, and the East is distinctly warmer, up to 0.4°C warmer in the Northeast (Table 2.2 and Wang et al., 2007b, compare Mann et al., 2009).

(b) 1171-1270: The simulations reveal a negative anomaly in West China which agrees with reconstructions by Wang et al. (2007b). The reconstructed warming in the Northeast is not found in the simulation.

(c) 1601-1700: This century is the coldest period during the LIA (for the Northern Hemisphere (see Mann et al., 2009) which is captured as well in the reconstruction by Wang et al. (2007b). The simulated temperature anomaly pattern agrees with the reconstructions; in the Southeast where a negligible anomaly is reconstructed the simulated cooling is not significant.

(d) 1781-1880: The simulation reveals a persistent LIA with even lower temperature anomalies than during 1601-1700. This century includes the Dalton minimum and in particular the extreme cold decade 1810-1819 (Cole Dai et al., 2009). The simulated cold century deviates from the reconstructions by Wang et al. (2007b), mainly in the West.

(e) 1951-2000, and (f) 1991-2000: This periods show the highest temperature during the last millennium (up to 0.9°C, significant in almost all regions).

In summary, a distinct medieval warming in China is found in the simulation until 1140 AD; this is terminated by a cooling during 1170-1270 (in the reconstructions

by Wang et al., 2007b, the medieval warming persists until 1270). The LIA persists until the 19th century. Before 1900 the absolute values of the simulated temperature anomalies are lower than in the reconstructions ($\pm 0.2^\circ\text{C}$ compared to $\pm 0.4^\circ\text{C}$).

Ensemble E2 shows a distinct warming as in the reconstructed temperature in (b) 1171-1270 (Fig. A.2 in Appendix). But in (c) 1601-1700, the reconstructed warming in NE China is still not simulated (the amplitudes in ensemble E2 is even larger than in ensemble E1). E2 reveals a cooler LIA (d) and (e). For the last half century (f), MW is again obvious in most parts of China with smaller amplitudes than in ensemble E1.

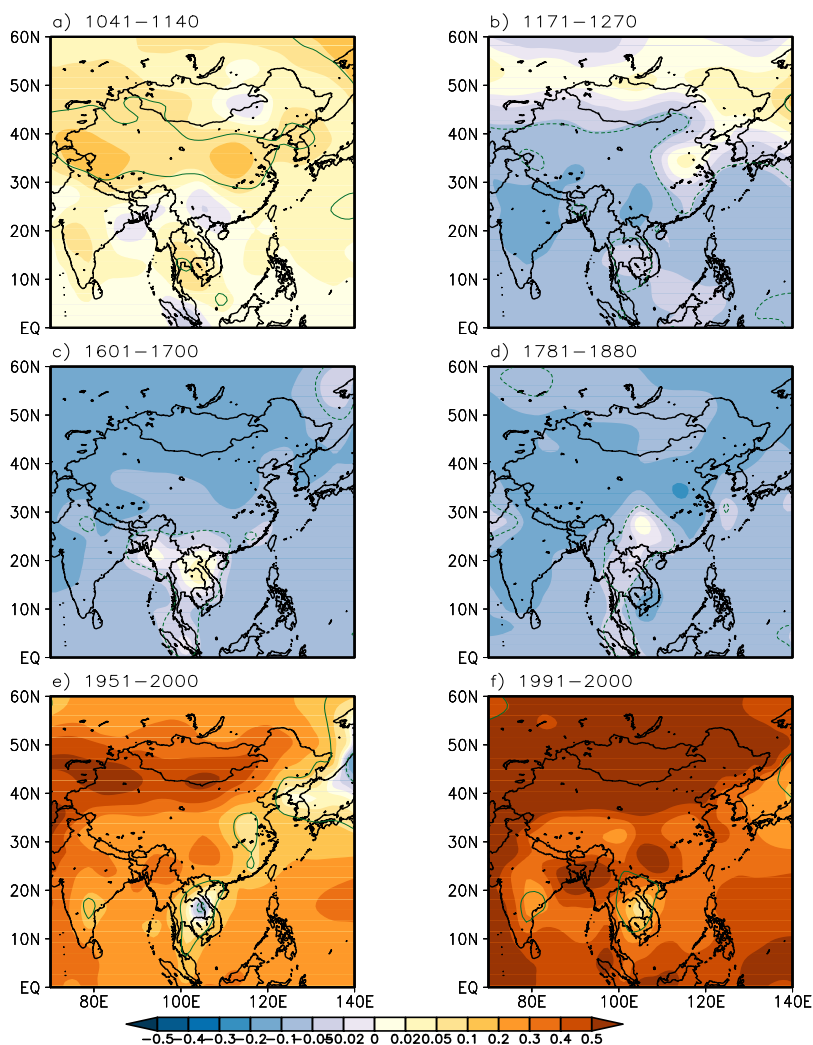


Fig. 2.8: Simulated temperature anomalies [°C] during the periods as indicated (with respect to the overall mean in 800-2005, compare with Fig. 5 in Wang et al., 2007b). The green contours mark the statistical significance as p-values (representing 90% confidence level) of the Student's t-test.

Bi-centennial temperature patterns

The simulated temperature anomalies are assessed by means for adjacent bi-centennial periods (800-1000, 1000-1200, etc.) to obtain a complete overview of the climate evolution in China (Fig. 2.9).

(a-b) 800-1200: During this period, which is considered as the warmest during the last two millennia in the Northern Hemisphere (Mann et al., 2008), moderate warming prevailed in China (up to $\pm 0.1^{\circ}\text{C}$). Deviations from this are weak and limited to a few regions. In 800-1200 significance is restricted to the Northeast, in 1000-1200 also in the northwest. Recent reconstructions of Mann et al. (2009) find a warming up to $\pm 0.5^{\circ}\text{C}$ in Southeast Asia.

(c-e) 1200-1800: A complete cooling is the most distinct feature of these centuries (significant in the West and in the Southeast China). In 1200-1400 and 1600-1800 the cold anomalies below -0.08°C are significant. The simulated LIA cooling is interrupted during 1400-1600 in Tibet and the Northeast when the LIA prevailed in the Northern Hemisphere (Mann et al., 2008). A warming is reconstructed by Mann et al. (2009) for 1400-1700 in Southeast Asia.

(f) 1800-2000: The model shows a cold northeast and a warm southeast China. In the northeast the cold anomalies at the beginning of the 19th century (Fig. 2.8d) compensate for the warming in the 20th century in the North (Fig. 2.9).

Ensemble E2 has a relative warmer MCA (up to 0.2°C) compared to ensemble E1 (Fig. A.3a-b in Appendix). The weak cooling in 1200-1400 in ensemble E1 is replaced by a moderate warming (Fig. A.3c). The moderate cooling in the early LIA in ensemble E1 is lowered severely by about 0.3°C in ensemble E2 (Fig. A.3d). In the last four hundred years, the temperature anomaly patterns are similar to ensemble E1.

Annual cycle

The climate evolution is accompanied by a considerable change of the annual cycle (Fig. 2.10). Note that this figure shows the anomalies of summer minus winter temperatures with respect to the total simulated period).

During 800-1200 (MCA) until the advent of the LIA the annual cycle shows a pronounced land-sea contrast with largest differences (summer minus winter) on the Tibetan plateau. Within 1200-1400 the annual cycle begins to weaken and the anomalies reverse in Central China. During the cold period in 1400-1800 the annual cycle reduces further (except in the Northwest) and reverses on the Tibetan plateau. After 1800 a severe reduction of the annual cycle in the North and on the Tibetan plateau is found whereas the eastern Pacific shows an enhanced summer-winter contrast. Thus, the annual cycles during the modern and the medieval warming (MCA) differ considerably. The most probable reason is the anthropogenic aerosol load which increased during the 20th century (see discussions in Section 3.6).

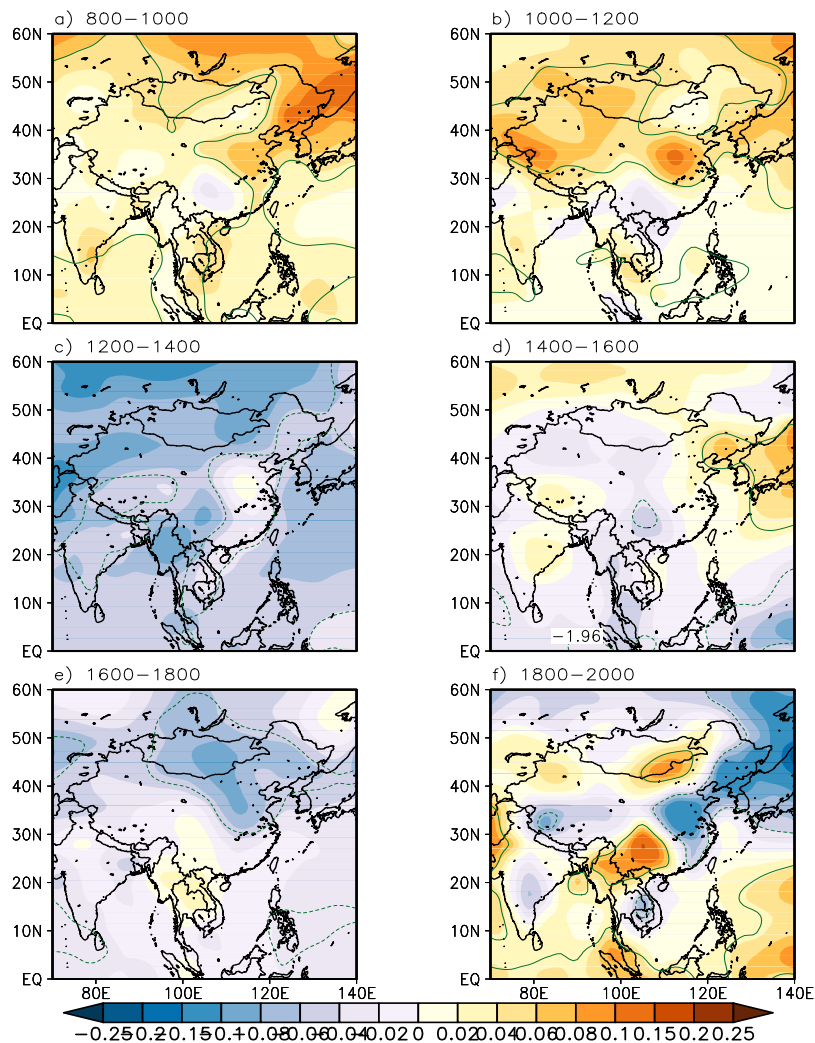


Fig. 2.9: Simulated temperature anomalies [$^{\circ}\text{C}$] as bicentennial means (with respect to the overall mean in 800-200). The green contours mark the statistical significance as p-values (representing 90% confidence level) of the Student's t-test.

Ensemble E2 reveals similar patterns of annual cycle anomalies in the MCA with larger amplitudes in central Asia and Mongolia (Fig. A.4a in Appendix). In the early LIA similar patterns are found with opposite polarities compared to ensemble E1 (positive in ensemble E2 and negative in ensemble E1), while in the late LIA the amplitudes of the positive anomalies in central Asia are smaller (Fig. A.4d and e). In the last hundred years, in agreement with ensemble E1, the annual cycle anomalies differ considerably with the MCA (Fig. A.4f).

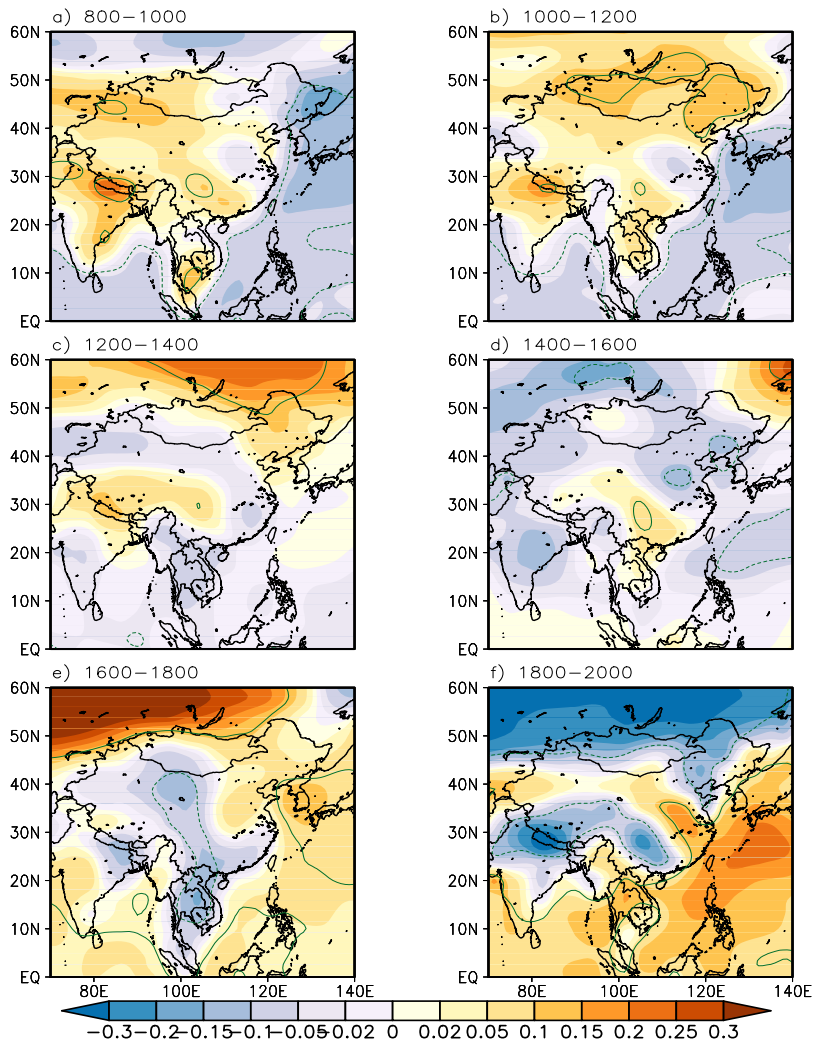


Fig. 2.10: Simulated annual cycle (defined as summer minus winter temperature) as bicen-tennial means [°C]. The mean annual cycle in 800-2005 is subtracted. The green contours mark the statistical significance as p-values (representing 90% confidence level) of the Student's t-test.

2.6 Summary and conclusion

The near surface temperature data in a 1200 years climate simulation is compared to reconstructed regional temperature records in China. The millennium run is designed as an ensemble of simulations with the atmosphere ocean general circulation model ECHAM5/MPIOM/JSBACH including modules for land vegetation and ocean biogeochemistry. The two full-focings ensembles are forced by two different total solar irradiance (with weak and strong variability), as well as volcanic forcing, land use change, and anthropogenic green house gases and aerosols.

The simulated Northern Hemispheric means show long-term warming and cooling periods corresponding to the MCA in 900-1300, the LIA in 1300-1850, and the MW after 1850. Volcanic eruptions are the most efficient external forcing (Jungclauss and the COMSimm Team, 2009). The spread within the ensemble simulations yields the uncertainty $\pm 0.5^{\circ}\text{C}$ of the dynamic reconstruction.

A mutual comparison of simulated and three reconstructed data sets indicates that the reconstructions by Wang et al. (2007b) are reconcilable with the simulations obtained with the solar irradiance by Krivova et al. (2007), ensemble E1 with a variability amplitude of 0.1%. The long term anomalies of other reconstructions are beyond the uncertainty given by the simulations. The low frequency variability of the simulated mean temperature in China reveals a power-law scaling in the power-spectrum, $S(f) \sim f^{-\beta}$ with $\beta \approx 0.5$, indicating stationary long term memory (obtained for both ensembles). This agrees with the variability of the reconstructed mean temperature in China by Wang et al. (2007b), whereas other reconstructions reveal nonstationary power spectra with $\beta \approx 2$.

The model simulations are compared to regional temperature reconstruction with decadal and centennial temporal resolution (Wang et al., 2007b). Deviations from the reconstructions are: During the 11th century the model shows a moderate warming in China, whereas reconstructions indicate a zonal temperature contrast with a cooler western and a warmer eastern part. A further discrepancy is found in the 13th century when simulations are too cool in the west and the Northeast (in the Southeast the simulations agree with reconstructions). During the LIA the simulated temperature anomaly agrees with reconstructions in the West and the Northeast. The annual cycle during the MCA was stronger on land but weaker on the East Pacific compared to the last two centuries.

The main results can be summarized as: (i) The comparison of the temperature anomalies in China obtained in the model simulation with reconstructed data demonstrates that the ensemble E1 with weak solar irradiance variability is reconcilable with the reconstructions by Wang et al. (2007b). (ii) Simulated regional temperature anomalies show high inter-annual variability on decadal time scales with volcanic eruptions as the dominant signature. (iii) The uncertainty of the simulated mean temperature is of the order of $\pm 0.5^{\circ}\text{C}$. (iv) The power-spectra of the simulated and reconstructed mean temperature in China agree and indicate stationary long term memory, while periodicities apart from ENSO (3-4 years) are not simulated. (v) The land-sea contrast of the annual cycle changed sign during the last millennium.

Chapter 3

Precipitation variability in simulations and reconstructions

3.1 Introduction

Temperature and precipitation are the two important properties of climate and the most widely measured variables. According to Hughes and Diaz (1994), Bradley (2000), Bradley et al. (2003), and Graham et al. (2011), the Medieval Climate Anomaly (MCA) was characterized not by uniformly warmer temperatures, but rather by a range of temperature, hydroclimate and marine changes with distinct regional and seasonal expressions. The widespread hydroclimatic anomalies are a major reason why the term MCA has been proposed by a number of researchers (Stine, 1994; Bradley et al., 2003; Seager et al., 2007; Burgman et al., 2010; Diaz et al., 2011; Graham et al., 2011) since extreme droughts or pluvials have had an impact on human societies at the time equal to or greater than the changes in surface temperature (Büntgen et al., 2011). In the present thesis, the temperature variability in the last 1200 years in East Asia (Chapter 2) reveals only one facet of the past climate change. Therefore, the insights into the past changes of other societal relevant climate variables, like the long-term changes in precipitation and the links to the controlling circulation influences are paramount in better understanding and assessing the climate changes (Jones and Mann, 2004).

The global climate change in the last millennium is summarized by Diaz et al. (2011) and Graham et al. (2011). In East Asia, the dominant climate variability observed in Northern Hemisphere is detected in precipitation data in China by Zheng

et al. (2006). Proxy records from a regional reconstruction in central Asia north of the Himalaya (Yang et al., 2009) indicate reduced cool-season precipitation as suggested by the Guliya ice cap accumulation record (Wang et al., 2007a). The proxy records from the southern coast of China (Wang et al., 2005) show a transition towards a pattern in which the driest periods during the last millennium occur early in the Little Ice Age (LIA) between about 1300 and the late 1500s AD (Sinha et al., 2007). This pattern indicating early LIA aridity across much of monsoon Asia is also noted by Buckley et al. (2010) and Graham et al. (2011). Central China also shows clear evidence for aridity during the LIA, though the timing is shifted roughly a century later than noted above (Zhang et al., 2008a; Tan et al., 2008). Documentary records from southeastern China (Zheng et al., 2006) indicate inverse precipitation variability compared to central China (MCA tending to be drier than the LIA in southeastern China). Ge et al. (2007) review the proxy records of precipitation in China during the Holocene (especially the last two millennia) and find also significant regional differences in China, especially east China. Such a pattern of opposing variability in monsoon rainfall over southern and northern China is well documented and characterizes observed and simulated precipitation trends over the second half of the twentieth century (Ding et al., 2008; Li et al., 2010).

The precipitation in East Asia is strongly influenced by the Asian Monsoon incorporating the East Asian and the Indian monsoon which are independent sub-systems but also interact (Ding and Chan, 2005). In the MCA, evidences are found for a strong Asian monsoon, wet conditions over much of tropical South America, dry conditions in equatorial East Africa, wet in South Africa, a dry western Mediterranean region and wet northwest Europe (see compilation of proxy data in Seager et al. 2007, Burgman et al. 2010, and Seager and Burgman 2011). Thus the MCA does not have a clear or uniform global pattern, although the reconstructions show that the South Asian monsoon was more drought-prone during the LIA than during the MCA (Shen et al., 2009, Berkelhammer et al., 2010, Diaz et al., 2011 and Graham et al., 2011) and there is a tendency to relatively wetter conditions during the MCA in some regions (Sinha et al., 2007; Zhang et al., 2008a).

The Yangtze river is the biggest river in terms of runoff volume in China, and it is strongly affected by the local interannual climate variability. Its densely populated low terrain catchment leads to disasters like floods or long-lasting wetness and drought conditions stressing natural vegetation and agriculture. Driving forces of the hydrological variability are the thermal contrasts between the high altitude snow on the Tibetan Plateau (TP) and the sea surface temperatures of the adjacent oceans which modulate the atmospheric circulation and the water cycles storage and supply. Temperature and snow cover on the TP and the thermal inertia of the oceans are also the origin of long term memory and interannual variability both of which lead to extreme events on different time scales. One of the large scale circulation patterns affecting the Yangtze Catchment (YC) is the South Asian summer monsoon whose variability on decadal to centennial time scales (Duan et al., 2004) determines the YC precipitation. The established positive correlation of near surface land temperature and monsoon strength may change sign in global warming

simulations (Sun et al., 2010); it is unknown whether such changes have occurred in the past. The East Asian summer monsoon is weaker during El Niño/Southern Oscillation (ENSO) warm phases (Kawamura, 1998; Ju and Slingo, 1995). However, this relationship varies on longer time scales due to anomalies in the western North Pacific (Wu and Wang, 2002). Gershunov et al. (2001) have demonstrated that the relationship between ENSO and average Indian rainfall varies less for decadal means than for annual data and have interpreted these time scale dependent relationships as a stochastic effect. A major restriction for a detailed analysis of long term climate variability is the short duration (about 50 years) of instrumental data in East Asia. But there is a wealth of documentary records and proxy data for the most relevant hydrological impacts like floods and droughts in south-eastern China and the TP (Wang et al., 1991; Jiang et al., 2006; Qian et al., 2008; Holmes et al., 2009). In order to physically interpret these data for climatological reconstruction, their dynamic consistency and their highly significant interrelation with large scale circulation patterns are necessary prerequisites.

The aim of this chapter is to derive the precipitation variability in East Asia during the last 1200 years, to determine the possible causes for its main trend and the impacts of internal climate variability on the runoff and the hydrological cycle in YC. The analysis includes simulated precipitation variability from one control simulation and two full-forcings simulations as well as a comparison with reconstructed drought index. The two full-forcings ensembles for 800-2005 AD are performed using the complex atmosphere-ocean general circulation model ECHAM5/MPIOM/JSBACH forced by the state-of-the-art solar forcing reconstruction by Krivova et al. (2007) and a forcing reconstruction with higher variability by Bard et al. (2000) (denoted as ensemble E1 (five members) and E2 (three members), respectively). The uncertainty of the simulations is estimated by the ensemble spread which is a measure of the internal variability. In the analysis of pursuing the possible causes for the main trend of simulated precipitation, single-forcing experiments are adopted.

This chapter is organized as follows: Section 3.2 describes the model components and forcings, and the reconstructed data. Section 3.3 gives an overview of reconstructed precipitation/drought index in the last millennium. Section 3.4 focuses on the variability of the precipitation and the runoff in the YC and its relationship with the Asia summer monsoon and ENSO in the control simulation. The precipitation variability through two ensemble simulations with two different solar forcings as well as reconstructed drought indices are analyzed in Section 3.5 in terms of the centennial climate anomaly patterns and regional climate anomalies. The possible causes for the distinguishing trends in the simulated precipitation are discussed in terms of internal forcing and dynamics in Section 3.6. The results are summarized in Section 3.7.

3.2 Data and methods

Model components and forcings

The millennium experiments are carried out using the Earth System Model (Jungclaus, 2009; Jungclaus et al., 2010) including the atmospheric model ECHAM5 (Roeckner et al., 2003), the ocean model MPIOM (Marsland et al., 2003) and modules for land vegetation JSBACH (Raddatz et al., 2007) and ocean biogeochemistry HAMOCC (Wetzel et al., 2006). ECHAM5 is run at T31 resolution ($\approx 3.75^\circ$) with 19 vertical levels, and MPIOM at a horizontal grid spacing of about 3° with 40 unevenly spaced vertical levels. CO_2 is interactively transported in the atmosphere and the ocean. The model is forced by reconstructions of (I) Total solar irradiance (TSI), (II) volcanic forcing considering aerosol optical depth (AOD) and effective radius distribution, (III) land cover change, and (IV) anthropogenic green house gases and aerosols. More details on the model and the forcings see Section 2.2 in Chapter 2.

Simulated data

The analysis uses the 3000-year unforced control experiment (01, see Table 3.1) as well as two ensemble experiments: ensemble E1 with five members (experiments 10, 12, 13, 14 and 15) forced by a weak solar forcing (about 0.1% of the standard TSI value of 1367W/m^{-2} , given by the difference between present-day and Maunder minimum, Krivova et al., 2007) and a second ensemble E2 with three members (21, 25 and 26) forced by a strong solar forcing (2.5%, Bard et al., 2000, see (I) in Section 2.2 in Chapter 2); the remaining natural and anthropogenic forcings are identical. The full-forcings experiments cover the period from 800 to 2005 AD (Bard et al., 2000; Jungclaus et al., 2010). The different initial conditions for the ensemble members are derived from a 3000-year control integration forced by constant conditions for 1860. In addition, sensitivity experiments with just one external forcing at a time were performed. Although the present thesis uses the sensitivity experiments as well, its main focus is the full-forcings experiments, i.e. ensemble E1 and E2. Zhang et al. (2010) compared both ensembles with climate reconstructions in China and concluded that ensemble E1 reproduces the reconstructed climate variability. Therefore, the present analysis is restricted to this five member ensemble E1 unless indicated otherwise.

China has an area of $9 \times 10^6 \text{km}^2$ and is approximated by the model area extending from 70° - 130°E and 17.5° - 55°N ; for a comparison with reconstructions China is divided in four regions (Fig. 3.1): Northeast (NE), Southeast (SE), Northwest (NW) and Southwest (SW) China based on the general characteristics obtained from Section 3.3. All anomalies are calculated with respect to the time means which are determined individually for each ensemble member in the whole period 800-2005 AD.

The YC with an area of $1.8 \times 10^6 \text{km}^2$ is approximated by the model area extend-

Table 3.1: List of the millennium experiments used in the present chapter carried out with ECHAM5/MPIOM/JSBACH at T31 resolution.

Exp. ID	Description	Years
01	Control run	800-3800
02	Single-forcing: only anthropogenic land cover change (ALCC)	800-2100
03	Single-forcing: only ALCC (maximum estimation)	800-2100
05	Single-forcing: only solar forcing	800-2005
07	Single-forcing: only biogeochemical influence of ALCC	800-2100
08	Single-forcing: ALCC plus fossil fuel emissions	1860-2100
09	Single-forcing: only volcanic forcing	800-2005
10, 12-15	Ensemble E1: full-forcings experiment members 1-5	800-2005
21, 25-26	Ensemble E2: full-forcings experiment members 1-3	800-2100

ing from 100°-120°E and 25°-35°N (Fig. 3.2). The hydrology is based on annual mean catchment averages of precipitation (PRCP), near surface air temperature (2m, TEMP), and soil wetness (WET). The Yangtze runoff (RUN) in the model is determined in the estuary (near 120°E, 31°N).

The TP is approximated by the area extending from 80°-92°E and 30°-37°N (Fig. 3.2). We analyze snow depth (SNOW) to capture climatology and storage and snow melt (MELT) as the freshwater discharge.

The Asian summer monsoon is characterized by two indices: The Monsoon Hadley circulation index (MHI) is defined as $MHI = V_{850} - V_{200}$ (Goswami et al., 1999), where the meridional velocities V are determined at 850 and 200hPa in 70°-110°E and 10°-30°N. The MHI describes the South Asian (Indian) summer monsoon as part of the Hadley cell. The East Asian summer Monsoon Index (EAMI) which describes the subtropical circulation is defined by the difference in sea level pressure in 160°E minus 110°E in 10°-50°N (Guo et al., 2004; Wei and Zhang, 2010).

El Niño/Southern Oscillation (ENSO) is described by sea surface temperature anomalies in the Nino3 region in the eastern tropical Pacific (5°S-5°N, 90°-150°W).

All anomalies are calculated with respect to the time means which are determined individually for each ensemble member in the whole period 800-2005 AD.

Reconstructed data

The reconstructed drought indices used in the present analysis are from Central Meteorological Bureau (1981, hereafter, CMB), Zheng et al. (2006), and Cook et al. (2010). All anomalies are with respect to the time means in the corresponding data set during the whole period.

The annual drought index from Zheng et al. (2006) is reconstructed for 501-2000

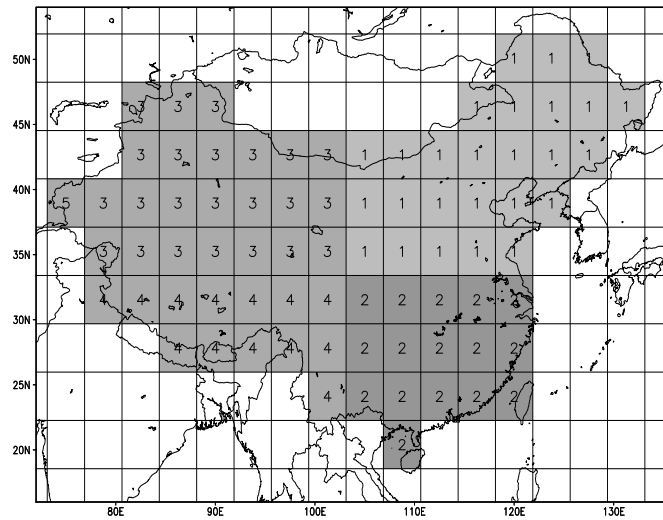


Fig. 3.1: Research regions in China: (1) Northeast (NE) China, (2) Southeast (SE) China, (3) Northwest (NW) China and (4) Southwest (SW) China marked in grid cells in the ECHAM5 T31 model simulation ($\approx 3.75^\circ$).

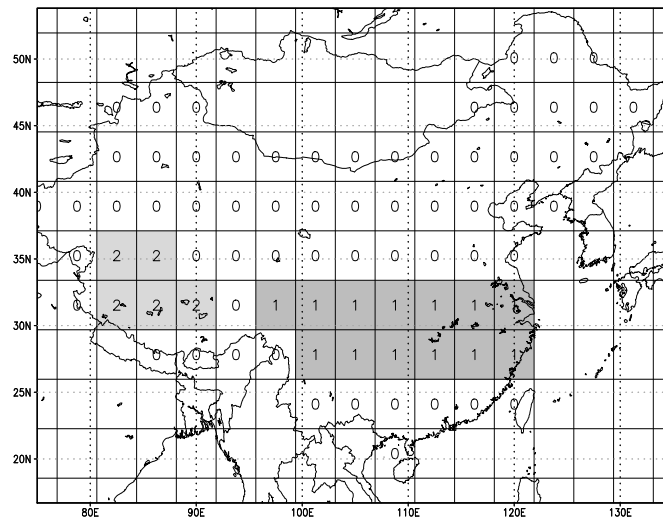


Fig. 3.2: Research regions in China: (1) Yangtze catchment and (2) Tibetan Plateau in the grid cells of the ECHAM5 T31 model simulation ($\approx 3.75^\circ$).

AD in eastern part of China with annual resolution based on Chinese historical documents and instrument measurements. The index includes the averaged value in eastern part of China and four sub-regions, the Huaibei (HB), Jianghuai (JH) and Jiangnan (JN) areas. The area locations are shown in Zheng et al. (2006). The original index varies from -2 (extremely dry) to 2 (extremely wet).

The annual drought index from CMB (1981) is reconstructed for 1470-1979 AD (May-September) and compiled from anecdotes about the weather found in local gazettes in 120 districts in China. The index includes the averaged value in China and nine sub-regions, which are Northeast (NE), North China (N, same area as HB by Zheng et al. 2006), central north (CN), central east (CE), central south (CS), south (S), northwest (NW), southwest (SW), and inner lands (In). The approximate area locations are shown in Central Meteorological Bureau (1981). The index varies from 1 (extremely wet) to 5 (extremely dry).

The Palmer Drought Severity Index (PDSI) from Cook et al. (2010) is reconstructed for 1300-2005 AD in JJA (June, July and August) based on tree rings in the forested areas of the Asian Monsoon area (Cook et al., 2010). The index is averaged over four regions, Northeast (NE), Southeast (SE), Northwest (NW) and Southwest (SW) China according to Fig. 3.1. The index varies from -4 (extremely dry) to 4 (extremely wet).

Long term memory and power spectrum analysis

In Section 3.4 short term memory is determined by the e-folding time (Wang et al., 2010), assuming an exponential decay of the autocorrelation function, $C(t) = \exp(-t/\tau)$. Long term memory (LTM) is determined by power spectra and detrended fluctuation analysis (DFA). All time series are standardized in the calculations. The power spectra (see also Section 2.2 in Chapter 2) are averages of the spectra calculated in 10 non-overlapping segments. The DFA is an efficient method to determine LTM in stationary time series (Peng et al., 1994; Fraedrich and Blender, 2003). The major application of the DFA is the extraction of power laws while oscillations (or cycles) should be analyzed by a standard power-spectrum or periodogram. The DFA yields the fluctuation function $F(t)$ on the time scale t . For a power law in the power spectrum, $F(t) \sim t^\alpha$, the exponents are related by $\beta = 2\alpha - 1$. To determine $F(t)$ the anomalies are integrated to the profile which is partitioned in segments of length t , where linear fits are determined. The fluctuations $F(t)$ are the variances of the profile with respect to these fits averaged in all segments. The correlations are based on Pearson's correlation coefficient (Table 3.2 and 3.3)

Singular spectrum analysis (SSA, Vautard and Ghil, 1989), applied in a different context by Fraedrich (1986) is used to determine modes of variability which cannot be associated with distinct spectral modes (for example the cyclic El Niño/Southern Oscillation). The SSA provides an adaptive spectral filter which decomposes variability according to dominant modes obtained in prescribed windows. In these windows empirical orthogonal functions (EOFs, denoted as singular vectors) are determined which maximize the variability. The singular values describe the amount of variability in the corresponding vector. The principal components are obtained by projecting the data on the singular vectors, and the original time series can be retrieved by sums of principal components multiplied by the singular vectors (this is analogous to the superposition of fields by EOFs). An oscillation in the data leads

to a pair of singular vectors which are in quadrature (compare sine and cosine functions) and are used to reconstruct the periodic component of the data.

3.3 Reconstructed drought index in East Asia

East Asia has the strongest monsoon system in the world, and is sensitive to the changes in all components of the climate system. Thus it is characterized by large climate changes and enormous variability covering multi-millennial to intraseasonal timescales in the past. From May to August, the Asian summer monsoon shifts through a series of dry and rainy phases as the rain belt moves northward, beginning over the South China Sea, to the Yangtze River Basin and Japan, and finally to North China and Korea. When the monsoon ends in August, the rain belt retreats to South China. West China (especially Northwest), due to its locations in the deep continent, has less rainfalls compared to the eastern China. For example, Xinjiang Province, located closely to the arid central Asia (ACA) areas, which is a unique dry land area that is likely to be strongly influenced by global warming. The understanding of the past variations in effective moisture in such regions is also of essential importance for the prediction of future hydrological change.

Central Asia and West China

The arid central Asia (ACA) has been characterized by a relatively dry MCA (1000-1350 AD), a wet LIA (1500-1850 AD) and a wetness during recent decades (Chen et al., 2010). Proxy records from a regional reconstruction in the north of the Himalaya indicate an anomalous dry climate in MCA, whereas the LIA extended from the 15-18th centuries and was accompanied by pluvial conditions reduced cool-season precipitation (Yang et al., 2009).

In the northeast margin of the TP, there were three short wet periods from the end of 10th century to the early 11th, from the end of 11th century to the early 12th and first half of the 20th century. The driest periods were at the end of the 17th and 18th centuries (Tan et al., 2008). This evidence for aridity during the LIA is also noted by Zhang et al. (2008a) with the period roughly shifted by a century later. In the same region, Liu et al. (2006) find that the precipitation variation over this region displays a 'W' shape in the last 1000 years, which has three peaks and two gaps. The precipitation is low during 1571-1879 AD, and high during 1880-2000 AD. 1900-2000 (1962-2000) AD is the century with the highest precipitation. For the same region, Liu et al. (2005a) find increased precipitation in 1403-1449 and 1615-1661 and decreased precipitation in 1321-1348, 1497-1557, 1728-1743 and 1885-1891. Significant abrupt changes occurred in the 15th century.

In Delingha Qinghai province in the last 1000 years, Shao et al. (2005) find a prominent upward trend in the precipitation occurring in the last century and the notable strengthening of the global monsoon during 1961-1990, wet periods occurred in 1520-1633 and 1933-2001, whereas dry intervals in 1429-1519, 1634-1741 and

after the 1990s.

East China and India

Documentary records from the precipitation in eastern China are analyzed by Zheng et al. (2006). On the centennial time scales, precipitation variation in eastern China exhibited four dry epochs (500s-870s, 1000s-1230s, 1430s-1530s and 1920s-1990s) and three wet epochs (880s-990s, 1240s-1420s and 1540s-1910s), with multi-decadal dry/wet fluctuations within each epoch. However, southeastern China (Zheng et al., 2006) indicates an inverse precipitation variability compared to central China (MCA tending to be drier than the LIA in southeastern China). Ge et al. (2007) review the proxy records of precipitation in China during the Holocene (especially the last two millennia) and find also significant regional differences in China, especially east China. Shen et al. (2009) analyze the eastern China summer precipitation in proxy data and a millennium run, and find an increased frequency of drought-in-north/flood-in-south spatial pattern over eastern China during the last two decades which is unusual in the past five centuries. Such a pattern of opposing variability in monsoon rainfall over southern and northern China is well documented and characterizes observed and simulated precipitation trends over the latter half of the twentieth century (Ding et al., 2008; Li et al., 2010).

In northern China in the last 1860 years, three intervals of high precipitation were identified at 138-450 AD, 730-1200 AD, and 1860-1960 AD (Tan et al., 2010). Two intervals of low precipitation occurred at 1320-1410 AD and 1530-1860 AD. The reconstructed monsoon precipitation variations correlate well with other records further east in the eastern Yellow River Basin, suggesting synchronous precipitation changes during the late Holocene in the semi-humid region of northern China on decadal to centennial scales.

The proxy records from the southern coast of China show a transition towards a pattern in which the driest periods during the last millennium occur early in the LIA (between about 1300 and the late 1500s) (Sinha et al., 2007; Wang et al., 2007a), which indicates early LIA aridity across much of monsoon Asia also noted by Buckley et al. (2010) and Graham et al. (2011). Sinha et al. (2007) present a near-annually resolved record of the Indian summer monsoon rainfall variations in India that spans from 600 to 1500, periods of severe drought, lasting decades, occurred during the 14th and mid 15th centuries and coincided with several of India's most devastating famines.

Periodicity

In northern and southern TP, the periodicities displayed in the ice core records are similar and correspond to the periodicities of the Quasi-Biennial Oscillation, the Southern Oscillation, the North Atlantic Oscillation, and the sunspot cycle (Wang et al., 2007a). In Delingha Qinghai province, Liu et al. (2005a) find a quasi-200-yr cycle during 1000-2001 being most intense in 1440-1640. From the end of the 18th century to the beginning of the 19th century, a quasi-120-yr cycle is found. In the

first half of the 19th century, the quasi-200-yr cycle is in positive phase and the quasi-120-yr negative while the reverse occurs in the second half century. In the 20th century, both are negative.

In eastern China, three statistically significant bi-decadal (15-35-yr), pen-dadecadal (40-60-yr), and centennial (65-170-yr) oscillation are found by Shen et al. (2009). Ding et al. (2008) find a near 80-yr oscillation using the 123-year (1880-2002) precipitation data at 35 stations in East China.

Correlations with temperature

With regards to the relationship between temperature and precipitation, on the longest, centennial time scales temperature was generally above average when dry climate conditions predominated on decadal to centennial timescales during the last 1000 years. The coldest decades of the last millennium (1630-1650s) matched with an anomalously wet period (Yang et al., 2009). Yao et al. (1996) find that the temperature is positively correlated with precipitation according to the Guliya ice core record. Negative correlations between temperature and precipitation are reported by Peng et al. (2010) for eastern China and by Holmes et al. (2007) for western China. In the YC there are obviously no fixed modes of climate changes such as warm-wet, cold-wet, warm-dry or cold-dry (Zhang et al., 2008b). In the arid central Asia (ACA), the multi-centennial precipitation changes show a generally inverse relationship with the temperature changes in the Northern Hemisphere including China and western central Asia (Chen et al., 2010).

3.4 Precipitation and runoff in Yangtze catchment in control run

The comparison between the simulated control climate for 800 AD to the present-day observed and NCEP/NCAR re-analysis data (in brackets, Kalnay et al., 1996) shows the following results: The average model river runoff is 50,600 m³/s (31 900m³/s), the catchment temperature is 12.1°C (10°-15°C) and the annual precipitation is 1730 mm/year (1500-2500mm/year). The soil wetness measured in volume fractions is 0.66 (0.3-0.4) and the mean snow depth on the TP is 0.009m (0.006m). The results reveal that, although the model simulates a past climate, the mean values are within the range of present-day observations. The differences are not only due to the model forcings and boundary conditions but also due to parameterizations of precipitation and soil hydrology, the low model resolution and the representation of the complex orography of East Asia.

In this section, results for short and long term memory are presented first and correlations on different time scales including a singular spectrum analysis are derived in the following subsections with a short summary at the end.

3.4.1 Short and long term memory

In the present section memory is used equivalently to variability to emphasize processes and time scales involved. Short term memory is characterized by the e-folding time τ . For the runoff and the soil wetness $\tau = 1$ year, while snow on the TP decays distinctly faster, $\tau < 1$ year. The remaining data does not reveal a detectable e-folding time scale.

LTM is present in a time series if the low frequency variability grows with decreasing frequency. In most practical circumstances the power spectrum follows a power-law $S(f) \sim f^{-\beta}$ with $0 < \beta < 1$ for low frequencies. Absence of LTM is given for a white spectrum with $\beta = 0$. The limit $\beta = 1$ (1/f spectrum or icker noise) constrains stationarity. The exponential decay of the auto-correlation function changes to a power law decay, $C(t) \sim t^{-\gamma}$, with an exponent γ determined by $\gamma = 1 - \beta$. LTM is determined by power spectra and detrended fluctuation analysis (DFA), see Section 3.2.

The long term variability varies substantially in the compartments and reveals three main types:

Yangtze runoff and soil wetness in the catchment show a power spectrum with a power-law for intradecadal frequencies (Fig. 3.3a), $S(f) \approx f^{-\beta}$, with $\beta \approx 0.6$. For low frequencies, the spectra of runoff, soil wetness, and temperature point to a weak memory on decadal time scales (Fig. 3.3b). For precipitation the spectrum is white in the accessible frequency range.

The scaling of the power spectrum is substantiated by DFA (Fig. 3.4). In the intradecadal range the fluctuation functions for runoff and soil wetness increase approximately according to a power law $F(t) \approx t^\alpha$ with $\alpha = 0.8$. Using $\beta = 2\alpha - 1$, this corresponds to $\beta = 0.6$ marked in Fig. 3.3a. For longer time scales soil wetness, Yangtze runoff, and temperature show $\alpha = 0.55$, slightly deviating from a white spectrum memory ($\alpha = 1/2$); this is lower than $\alpha = 0.65-0.7$ obtained in observations and in a high resolution version of the atmospheric model ECHAM5 (Blender and Fraedrich, 2006).

Neglecting the low-frequency scaling and assuming a (constant) white noise behavior, the power spectra of runoff, soil wetness, and temperature can be described by a modified red noise spectrum (Blender and Fraedrich, 2006).

$$S(f) = \frac{S_0}{1 + \left(\frac{f}{f_0}\right)^\beta}$$

where f_0 is the inverse time scale of the crossover between white noise for low frequencies and scaling memory for high frequencies. The standard red noise (Lorentzian) power spectrum is given for $\beta = 2$. This time scale is of the order of one decade for all variables in the YC (except for precipitation).

Tibetan Plateau: Weak memory

Snow depth and snow melt on the TP are considered to be main controls of the Yangtze discharge. The variability of snow depth and snow melt reveal negligible interannual memory and a weak non significant spectral peak at the ENSO cycle of 3-4 years (Fig. 3.5a). Simulated snow cover on the TP reveals no long term memory. Therefore, according to this simulation, the Yangtze discharge memory cannot be explained by the properties of snow on the TP. In the YC the long time scale of soil wetness appears to be the most likely process explaining the runoff variability. The absence of decadal periodicities detected by Qian et al. (2003), for example, the 70 years Gleißberg cycle, confirms their external origin. The dominant types of variability are the quasi periodic ENSO and long term memory in the YC.

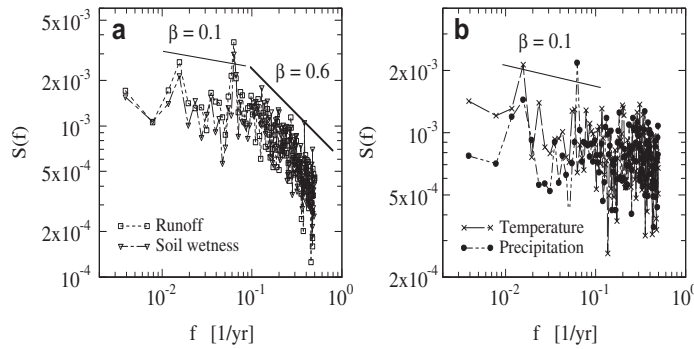


Fig. 3.3: Power spectra of (a) area averaged runoff and soil wetness, and (b) temperature and precipitation in the Yangtze catchment. The solid lines indicate power-laws $S(f) \approx f^{-\beta}$ with exponents $\beta = 0.6$ (bold), and $\beta = 0.1$ (thin line).

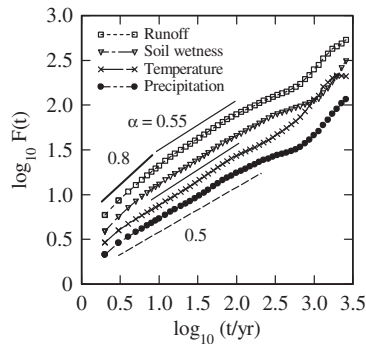


Fig. 3.4: Detrended fluctuation analysis (DFA) of area averaged runoff, soil wetness, temperature, and precipitation in the Yangtze catchment. The solid lines indicate power-laws in the fluctuation function $F(t) \approx t^\alpha$ with $\alpha = 0.8$ (bold), $\alpha = 0.55$ (thin solid), and $\alpha = 0.5$ (dashed, no memory).

Monsoon and ENSO: Periodicity

The monsoon indices EAMI, MHI, and ENSO show common characteristic spectra being constant for low frequencies and with a distinct peak in the range of the ENSO cycle, 3-4 years (Fig. 3.5b). For higher frequencies the spectra decay rapidly with high exponents $\beta > 2$. The ENSO cycle dominates the variability of both monsoon indices. There is no oceanic long term memory involved in the tropical sea surface temperature, in contrast to, for example, the mid-latitude northern Atlantic ocean (Fraedrich and Blender, 2003).

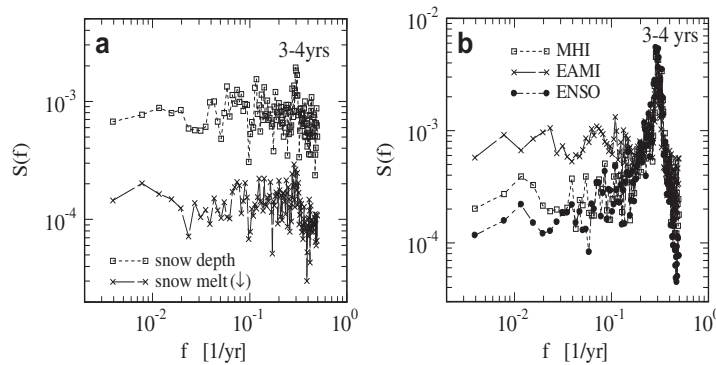


Fig. 3.5: Power spectra of (a) area averaged snow depth and snow melt (shifted) on the Tibetan Plateau and (b) monsoon indices and ENSO. All spectra in (b) are peaked at 3-4 years.

3.4.2 Local and remote relationships

The hydrological processes in the YC are controlled by the large scale circulation and snow melt on the TP. To derive dynamically consistent long term relationships correlation coefficients for annual and decadal data are derived. The length of 2800 years enables the calculation of highly significant correlation coefficients for annual data as small as $|r|=0.1$ with 99% significance (for decadal means with 95% significance). There is a large number of significant relationships within the YC and with snow on the TP, monsoon indices, and ENSO for annual data (Table 3.2, only values with 99% significance are included). For decadal means most of the relationships increase (Table 3.3, only values with 95% significance).

Yangtze catchment

The relationships between runoff, precipitation and soil wetness in the catchment are distinct and obvious. There is a high anti-correlation between temperature and soil wetness, in particular on decadal time scales. The correlation between temperature and precipitation is negative but weak. In West China Holmes et al. (2009) report a positive correlation between temperature and precipitation. In a simula-

ENSO cycle (Fig. 3.5a). For decadal means (Table 3.3) this changes significantly, probably due to the higher variability of snow melt on longer time scales.

The YC precipitation and TP snow depth are correlated on annual but not on decadal time scales. This agrees with the positive correlation between winter snow depth and subsequent summer rainfall in the catchment observed by Wu and Qian (2003) in station data during 1960-1998. According to the present analysis a possible underlying reason for the difference between annual and decadal data is the common correlation with ENSO: TP snow depth and YC precipitation are correlated with ENSO on annual but not on decadal time scales.

Impacts of monsoon and ENSO

The monsoon indices MHI, EAMI, and ENSO are highly correlated on annual time scales (Table 3.2). Negative correlations between monsoon indices and ENSO are caused by cold anomalies in the western tropical Pacific reducing monsoon strength during ENSO warm events. On decadal time scales all correlations are weaker.

A remarkable result is that the annual mean Yangtze runoff is neither correlated with southern and eastern Asian monsoon systems (MHI and EAMI) nor with ENSO; the decadal mean, however, shows the presumed monsoon control. Similarly, a significant relationship with the East Asian monsoon index EAMI exists for soil wetness only for decadal means. Further relationships are noted:

(a) The Indian summer monsoon index MHI determines annual YC precipitation, temperature, and TP snow melt variability. For decadal averages the impact decreases in the YC and increases for TP snow melt.

(b) On decadal time scales the hydrology in the YC is controlled by the East Asian summer monsoon index EAMI. There is a strong impact of ENSO on temperature in the YC, accompanied by reduced TP snow melt.

(c) Negative correlations between near surface land temperature and monsoon strength are found in global warming simulations and are ascribed to the reduction of upper level thermal contrast (see the discussion in Sun et al., 2010). However, this result depends crucially on the definition of the monsoon index, for example if the monsoon index is defined by the vertical shear (850-200hPA) of the zonal wind in 100°-130°E, 0°-10°N, the correlation with temperature in the YC is positive, $r = 0.23$, and vanishes for decadal means.

3.5 Precipitation variability in simulations and reconstructions

As summarized in Section 3.3, the reconstructions show regional dissimilarities in China which indicating a possibility of missing information in the averaged precipitation over the whole China. Therefore, the analysis starts with the centennial precipitation anomaly to reveal spatial patterns in the last millennium followed by regional anomalies in the four regions in China.

3.5.1 Centennial anomaly patterns

The simulated precipitation anomalies are assessed by geographical means for adjacent centuries (800-1000, 1000-1200, etc.) to obtain a complete overview of the climate evolution in East Asia (Fig. 3.6). To reveal possible links between warm/cold and wet/dry conditions, temperature anomalies (Fig. 2.8) are discussed along with precipitation anomalies.

(a-b) 800-1200 AD: During this period, which is considered as the warmest during the last two millennia in the Northern Hemisphere, moderate warming prevails in China (see Fig. 2.8a in Chapter 2), and wet conditions dominate (Fig. 3.6) while only in central and west China a precipitation deficit is found (Fig. 3.6b); in India and South Asia dryness dominates.

(c-e) 1200-1800 AD: The wet conditions prevail in China, only the west is drier than normal (the northeast after 1600). Interestingly, the precipitation in the monsoon areas, India and the South Asia, experiences a transition from deficit to abundance during these 600 years: In 1200-1400 the dryness has smaller amplitudes than 800-1000 in South Asia and even wetness in parts of India; in 1400-1600 the dryness is replaced by wetness in India while in the South Asia dryness remains; in 1600-1800, it is wet everywhere.

(f) 1800-2000 AD: The model shows a cold belt along 30°-40°N with anomalies of -0.1°C which are of the same magnitude as in the LIA. During the same time, humidity conditions reverse in China: The northwestern region becomes dry whereas large parts of China suffer from a severe precipitation deficit. Meanwhile, in India and South Asia, large amounts of rainfall are detected. In ensemble E2 with strong solar forcing, the precipitation bears an overall similarity in patterns (Fig. A.5 in Appendix). The amplitudes, however, are larger than E1 in the late MCA and the LIA (Fig. A.5c-e). The extreme drought in the last 200 years are the similar to ensemble E1 (Fig. A.5f).

3.5.2 Regional anomaly and ensemble spread

For a comparison with reconstructions, China is divided in four regions (see Fig. 3.1): Northeast (NE), Southeast (SE), Northwest (NW) and Southwest (SW) China.

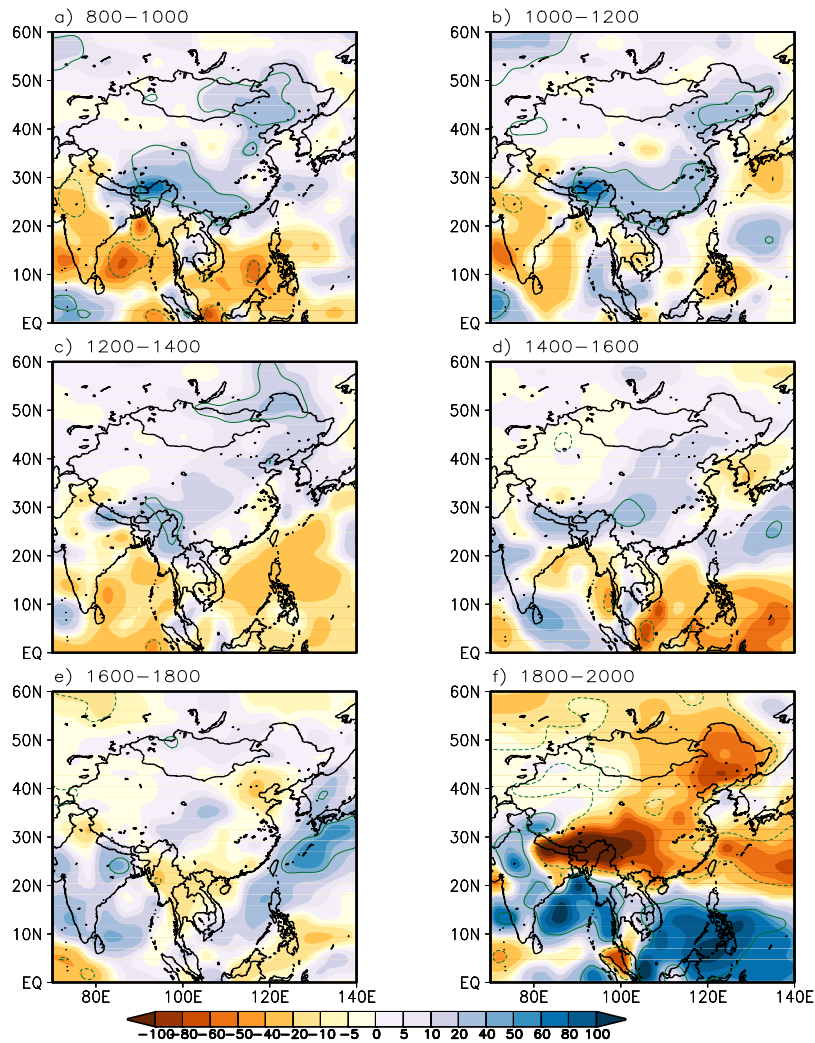


Fig. 3.6: Simulated total precipitation anomalies [mm/month] as bicentennial means (with respect to the overall mean in 800-2005 AD). The green contours mark the statistical significance as p-values (representing 90% confidence level) of the Student's t-test.

Precipitation is associated with interannual variability with some reminiscence of major volcanic eruptions in China in ensemble E1 (1258 and 1815, Fig. 3.7a). A first result is that the MCA is not related to below average precipitation. However, a persistent period with relatively low precipitation with small uncertainties assessed by the ensemble spread is observed during the LIA. The most distinct decrease in precipitation is simulated for the last two centuries. The four regions show similarities in the distinct decrease with the largest trend found in the SW China of about -150 mm/month (Fig. 3.7b-e). The warming during this period supports the synchronicity of reconstructed warm and dry periods. However, this relationship is not

found during the cold period 1200-1300 (except in SE Fig. 3.7c). The regional variability of precipitation shows the familiar maritime/continental contrast with lowest values in the West and highest values in SE China, where the decreasing amplitude after 1800 is the second largest.

Ensemble E2 with strong solar forcing reveals higher summer precipitation in the MCA and relatively low/high precipitation in the LIA in SE/NW China compared to ensemble E1. Besides that, no big difference is detected. The most distinguishing feature is also the summer rainfall deficits starting about 1800 AD as in ensemble E1 (Fig. 3.7b and e).

The reconstructed summer drought indices are shown in Fig. 3.7 using the data from CMB (Central Meteorological Bureau, 1981), Zheng et al. (2006) and Cook et al. (2010) indicated by 30-year running mean (see a detail description in Section 3.2). The drought index from Zheng et al. (2006) reveals high intra-annual variability, the dry periods are found in the 11th-13th centuries and 15th century in east China (Fig. 3.7a), which is not confirmed by Cook et al. (2010). The index from Cook et al. (2010) shows a dry period in the 19th century. The index from CMB (1981) shows small variability during the whole period. In the last two centuries, the summer in China has wet conditions with a decrease in the last 50 years shown by Zheng et al. (2006). However, the most distinguishing trend in the simulated precipitation, the rainfall deficits starting around 1800 AD in both ensembles, is not detected by any of the reconstructed data, although the index from Cook et al. (2010) has a sharp decrease in the last 30 years.

The results reveal high regional dissimilarities between simulations and reconstructions (Fig. 3.7b-e): Before 1500 AD, the dry periods in the 11th-13th centuries by Zheng et al. (2006) occur only in NE China (Fig. 3.7b, HB); in SE China (JH and JN in Fig. 3.7c) there is no dryness; on the contrary, the summer experiences wet conditions in the 13th century. The dry period in the 15th century occurs in all areas (HB, JH and JN in b and c, Zheng et al., 2006), which is confirmed by Cook et al. (2010) in NW and SW China (d and e). The index from Cook et al. (2010) in NE China (b) has the highest variability among all the four regions (compare b-e). From 1500 to 1800, drier summer in NW China (d) is found by CMB (1981) and Cook et al. (2010) with a higher variability. In SW (e), the precipitation has a rather small variability in both reconstructed data. In the last 20 years, Cook et al. (2010) find an increase in precipitation in NW China (d) and a decrease in NE and SE China (b and c).

Power Spectrum

The simulated summer precipitation in ensemble E1 (Fig. 3.8a, red) shows a flat spectrum ('white noise'), hence variability is without long-term memory present in the near surface temperature (see Fig. 2.6a, red). There is an increase in power within the frequency range corresponding to ENSO, which is the same as temperature (see Section 2.5 and Fig. 2.6). Obviously, temperature and precipitation are decoupled on long inter-annual time scales. The impact of the sea surface tem-

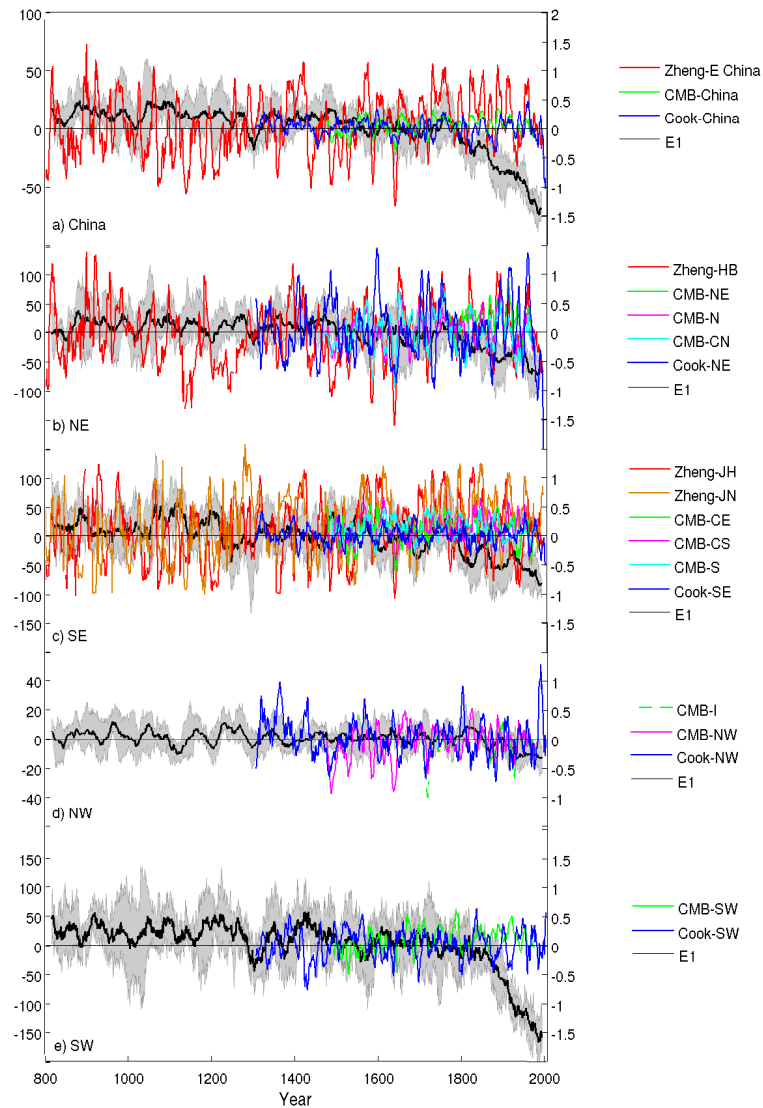


Fig. 3.7: Simulated precipitation [mm/month] anomalies (left axis) and reconstructed drought index (right axis) in **(a)** China, and in four regions **(b)** Northeast (NE) China, **(c)** Southeast (SE) China, **(d)** Northwest (NW) China and **(e)** Southwest (SW) China. Ensemble mean in E1 (black/bold) and spread are obtained by minimum and maximum (grey/shaded). Regions for reconstructed drought index in China see Section 3.2. The anomalies are calculated with respect to the time means in the corresponding data set during the whole period and smoothed by 30 years.

perature anomalies is restricted to air temperature, but not to precipitation intensity. The ensemble E2 with the increased solar irradiance variability (0.25%, Fig. 2.6a, blue) reveals a similar power-spectrum.

The reconstructed precipitation time series for East China (Zheng et al., 2006)

(Fig. 3.8b, red) shows periods $T \approx 2, 3, 4,$ and 7 years on a continuous background which decreases as $S(f) \sim f^{-2}$ (analyzed in 800-2000 AD). Periodic components in precipitation are not resolved in the available temperature data. The reconstructed precipitation by CMB (1981) and Cook et al. (2010) reveal similar power spectra with $\beta = 0.5$ and $\beta = 0.4$ (Fig. 3.8b, green/dashed and blue/dashed).

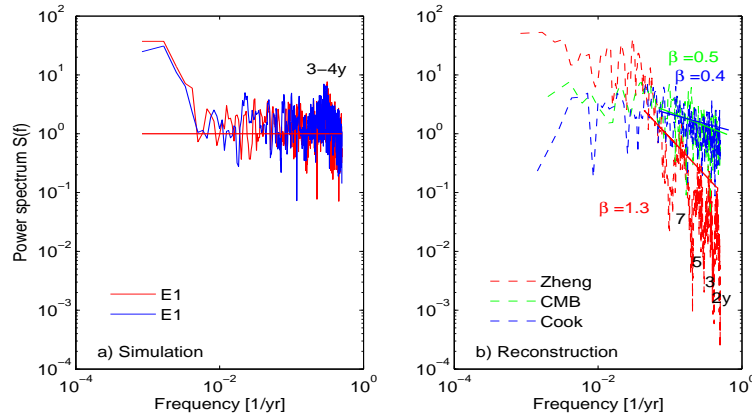


Fig. 3.8: Power spectra of (a) simulated total precipitation in ensemble E1 (red) and E2 (blue); (b) reconstructed drought index by Central Meteorological Bureau (CMB, 1981), Zheng et al. (2006) and Cook et al. (2010). The peaks are marked.

3.6 Possible causes for rainfall deficits after 1800 AD

As shown in the section above, the most distinguishing feature of the summer precipitation in the two full-forcings ensembles is the decreasing trend starting about 1800 AD in China. It is not detected in any of the reconstructed drought indices from the Central Meteorological Bureau (CMB, 1981), Zheng et al. (2006) and Cook et al. (2010). Therefore, this section focuses on discovering the possible causes for the simulated trend. A first look at the precipitation reveals that there are two exceptions: the 'no-decreasing' large scale precipitation in NE China and the increasing convective precipitation in SW China (Fig. 3.9a and d); the starting time of the decreasing differs in the four regions in China (for example about 1900 AD instead of 1800 AD in Fig. 3.9c). The decreasing trend has the biggest amplitude in SW, NE and SE China where the land cover experienced huge changes in the last hundred years. Therefore, the following section begins with the analysis of the comparison to sensitivity experiments which include the anthropogenic land cover change (ALCC) forcing.

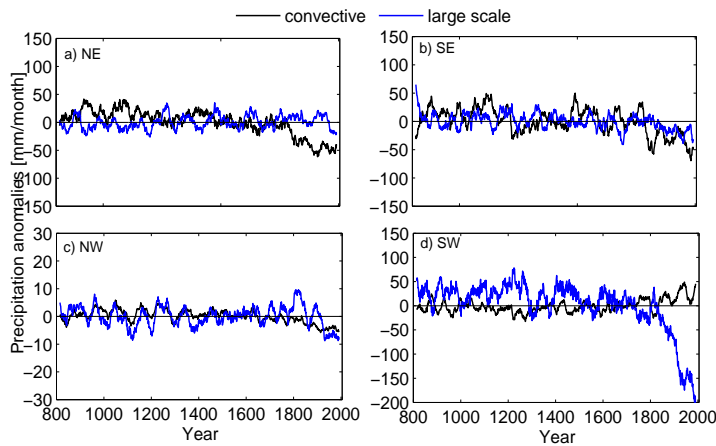


Fig. 3.9: Simulated summer convective (black) and large scale (blue) precipitation anomalies [mm/month] in four regions: **(a)** Northeast (NE) China, **(b)** Southeast (SE) China, **(c)** Northwest (NW) China, and **(d)** Southwest (SW) China in ensemble E1. The anomalies are calculated with respect to the overall mean in 800-2005 and smoothed by 30 years.

3.6.1 Internal forcing: anthropogenic land cover change and fossil fuel emissions

Single forcing experiments are adopted to analyze the possible causes, which include six sensitivity experiments (see the list of experiments in Table 3.1). Among all sensitivity experiments, only the precipitation related with ALCC shows the similar decreasing trend compared to the full-forcings ensembles; they are experiment 02, 03, 07 and 08, although the starting years and the precipitation amplitudes differ in four regions (see Fig. 3.10a-d, left panel).

The effect of ALCC on the climate system, which represents one of the most substantial human impacts on the Earth system, is revealed in experiments 02 and 03 forced by only ALCC (best guess and maximum estimation). In the present simulations, the ALCC is considered by applying the reconstruction of global agricultural areas and land cover, and the reconstruction merges published maps of agriculture from 1700 to 1992 AD and a population-based approach to quantify agriculture from 800 to 1700 AD (Pongratz et al., 2008; Jungclaus et al., 2010). In the experiments 02 and 03, the simulated total precipitation show distinguishing changes around year 1800 similar to the full-forcings ensemble E1, for example the drop in NE, SE and SW China (Fig. 3.10a, b and d, left panel). Similarly, the surface albedo in these three regions increases sharply in 02, 03 and E1 starting around 1800 AD or even earlier (Fig. 3.10a, b and d, middle panel) due to the ALCC caused by the growth of population and agriculture in the same regions in China at an unprecedented speed after the fall of the Ming Dynasty in 1644 (see Fig. 2.4 in Pongratz, 2009 and Pongratz et al., 2009). During this period, half of the national natural forest cover was transformed to cropland in most parts of China (except

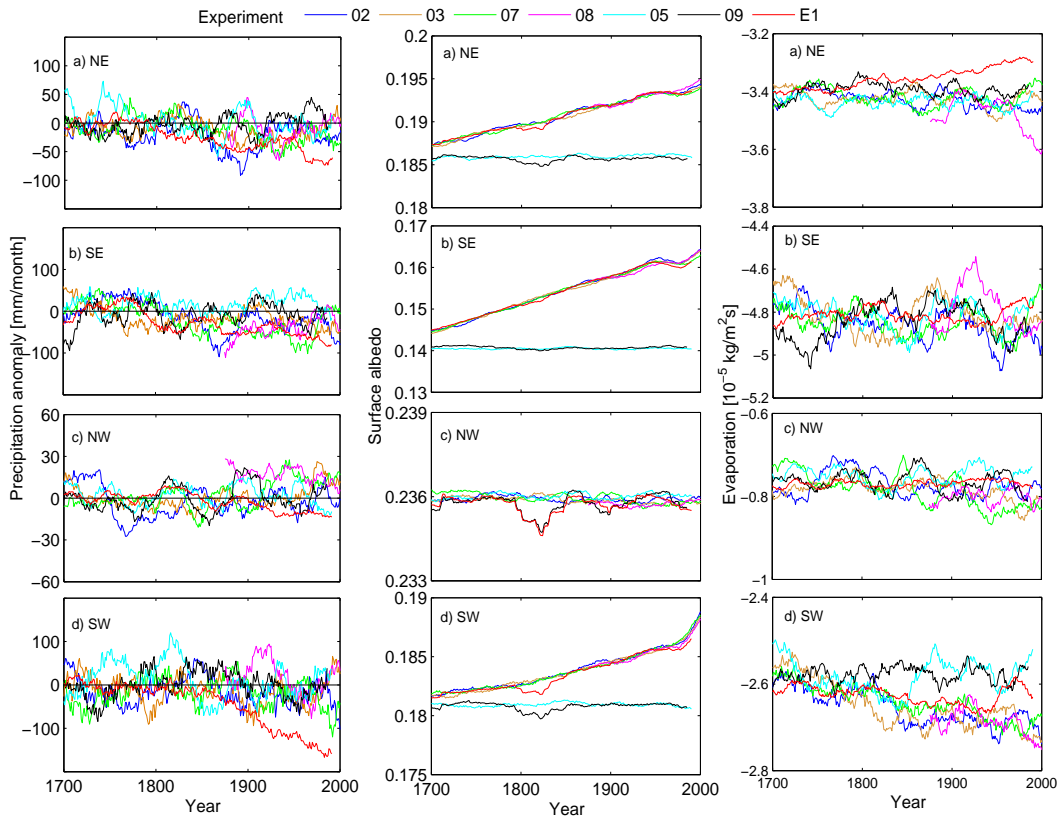


Fig. 3.10: Simulated summer total precipitation (left panel, mm/month), surface albedo (middle panel) and evaporation (right panel, $10^{-5} \text{ kg/m}^2 \text{ s}$) in four regions: **(a)** Northeast (NE), **(b)** Southeast (SE), **(c)** Northwest (NW), and **(d)** Southwest (SW) China in experiments as indicated (see Table 3.1). The anomalies are calculated with respect to the overall mean in 800-2005 and smoothed by 30 years. Depicted is only the time period after 1700, when clear temperature trends emerge.

NW, see Fig. 2.2-2.5 in Pongratz, 2009). This widespread deforestation caused the increase of the albedo due to the snow masking effect of forest as well as by the higher snowfree albedo of non-forest vegetation. The reduction of roughness, leaf area, and rooting depth (not shown) by deforestation reduces the evapotranspiration which is stronger in the tropics with the strong hydrological cycle than in the extra-tropics (confirmed by the larger amplitudes of reduction in evaporation in the SW and SE China than in the NE in Fig. 3.10a, b and d, right panel). In NE China, the missing energy caused by the overall increase in albedo and the reduction of absorbed radiation would be otherwise consumed by the precipitation while the evaporation increases anyhow.

The climate in China, therefore, is directly influenced by the modifications of the physical properties of the land surface, which are referred as the biogeophysical effects of ALCC. The increasing surface albedo leads to a local cooling. How-

ever, at a global scale, the other biogeophysical effects of ALCC other than albedo changes (for example, the loss of evaporative cooling) may compensate the albedo effect in the tropics, thus the balanced effects of ALCC may lead to a local warming (Pongratz, 2009). This warming is detected in most parts of China as shown in Chapter 2. The opposing biogeophysical effects of ALCC widely cancel each other on a global scale, but the regional climate is significantly influenced by ALCC and may even affect remote areas via teleconnections (see more discussions in Chase et al., 2000 and Pongratz, 2009). According to Wang et al. (2008), an increasing/decreasing in albedo in the TP leads to less/more precipitation in East Asia. An increase in albedo decreases the absorption of solar radiation (Fig. 3.11a, b and d, left and middle panels) and thereby reduces turbulent heat fluxes (Pongratz, 2009). A reduction in the latent heat flux (Fig. 3.12d, left panel) may decrease the water vapor content in the boundary layer, while holding back water in the soil or increasing runoff. A reduction in the sensible heat flux may reduce the heating of the boundary. Both may decrease cloud cover (Fig. 3.12a, b and d, right panel) and convection (Pongratz, 2009) as shown in Fig. 3.9b and c. In contrast, in NW China, where a small variability of ALCC is detected, hardly any changes are found in the precipitation, the albedo (except the minor fluctuations caused by volcanic forcing around 1800-1850 AD) and the evaporation in experiments 02, 03 and ensemble E1 (Fig. 3.10c, three panels).

On the other hand, another aspect of the effects of ALCC on the climate needs to be considered as well, i.e. the biogeochemical mechanisms represented by the experiments 07 (only the biogeochemical influence of ALCC). While the biogeophysical mechanism discussed above includes all modifications of the physical properties of the land surface (such as albedo, roughness, and evapotranspiration), the biogeochemical effect of ALCC has the most important influence from the carbon cycle, and the associated impact on the global CO₂ concentration. Altering atmospheric CO₂, ALCC modifies the Earth's energy balance and thus the climate. According to previous studies (Houghton, 2003; Pongratz, 2009), about one third of the anthropogenic CO₂ emissions over the last 150 years are estimated to be the direct consequence of ALCC. The biogeochemical effect of ALCC counteracts the biogeophysics (Brovkin et al., 2004), which is detected in NW/SE China, where the precipitation increases/decreases in experiment 07 while decreases/increases in experiment 02 after 1900 (Fig. 3.10b and c, left panel and right panel). However, all the carbon fluxes involved in the biogeochemical mechanism of ALCC are very uncertain. The uncertainty range assigned to estimates of ALCC emissions is about $\pm 70\%$ even for the last best-documented decades (Denman et al., 2007; Pongratz, 2009). Therefore, which of these two effects of ALCC dominates and its uncertainties are still under investigation.

Besides ALCC, the fossil fuel CO₂ emissions may be another cause for the precipitation deficits in China as seen in the experiment 08 (forced by ALCC plus fossil fuel CO₂ emissions prescribed, magenta curves in Fig. 3.10a-d, left panel). The carbon dioxide (CO₂) concentrations in the atmosphere increased from approximately 280ppm in pre-industrial times to 382ppm in 2006, Methane (CH₄) is more

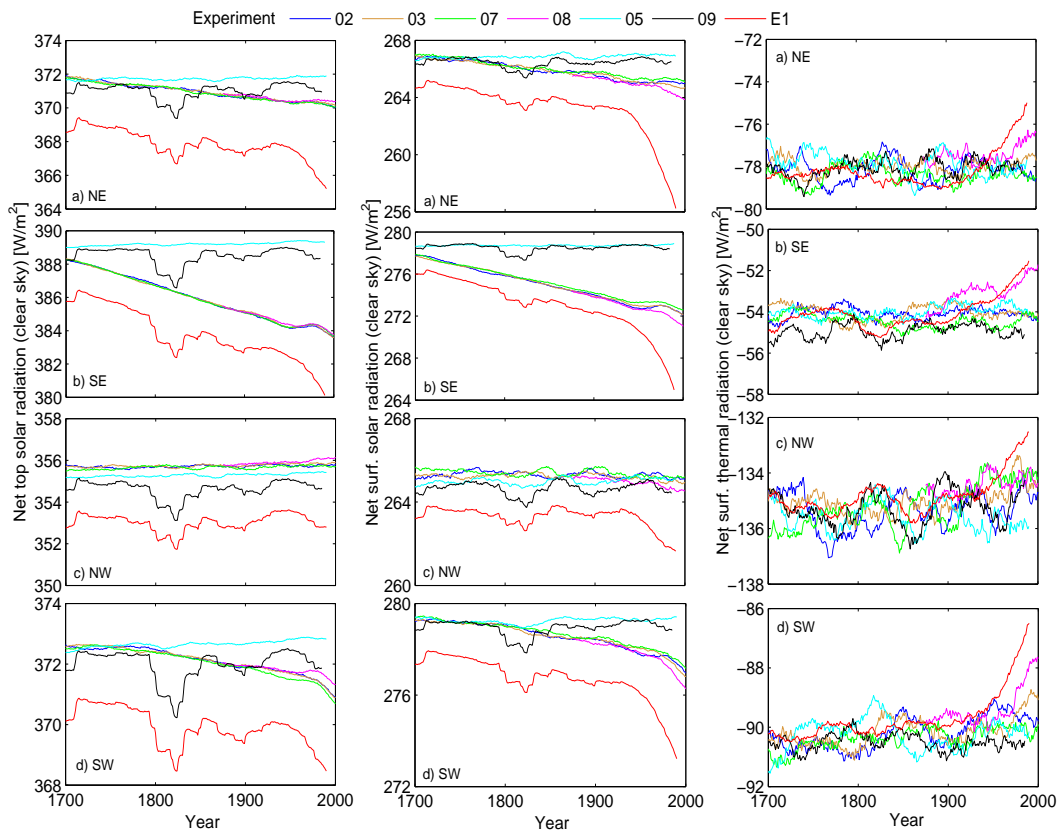


Fig. 3.11: Clear sky net top solar radiation (left panel, W/m^2), net surface radiation (middle panel, W/m^2) and net thermal radiation (right panel, W/m^2) in four regions: **(a)** Northeast (NE) China, **(b)** Southeast (SE) China, **(c)** Northwest (NW) China and **(d)** Southwest (SW) China in experiments as indicated (see Table 3.1). The anomalies are calculated with respect to the overall mean in 800-2005 and smoothed by 30 years. Depicted is only the time period after 1700, when clear temperature trends emerge.

abundant in the atmosphere now than at any time in at least the past 650,000 years and Nitrous oxide (N_2O) has increased approximately by 18 % in the past 200 years (Solomon et al., 2007). After 1900, all these three gases concentrations increase at a very high speed in the present simulations (Fig. 3.13).

These gases absorb and emit radiation which is the fundamental cause of the greenhouse effect, and thus can cool or warm the atmosphere depending on their properties. At the same time, they affect the clouds formation and thus change the cloud properties and the initiation of precipitation. The radiative effects of aerosols on clouds mostly act to suppress precipitation, because they decrease the amount of solar radiation that reaches the land surface, and therefore cause less heat to be available for evaporating water and convective rain clouds. However, they have also been reported to increase rainfall (see Menon et al., 2002, Lohmann and Feichter, 2005, and Rosenfeld et al., 2008 for a overview, Fig. 3.11 and Fig. 3.11 for a

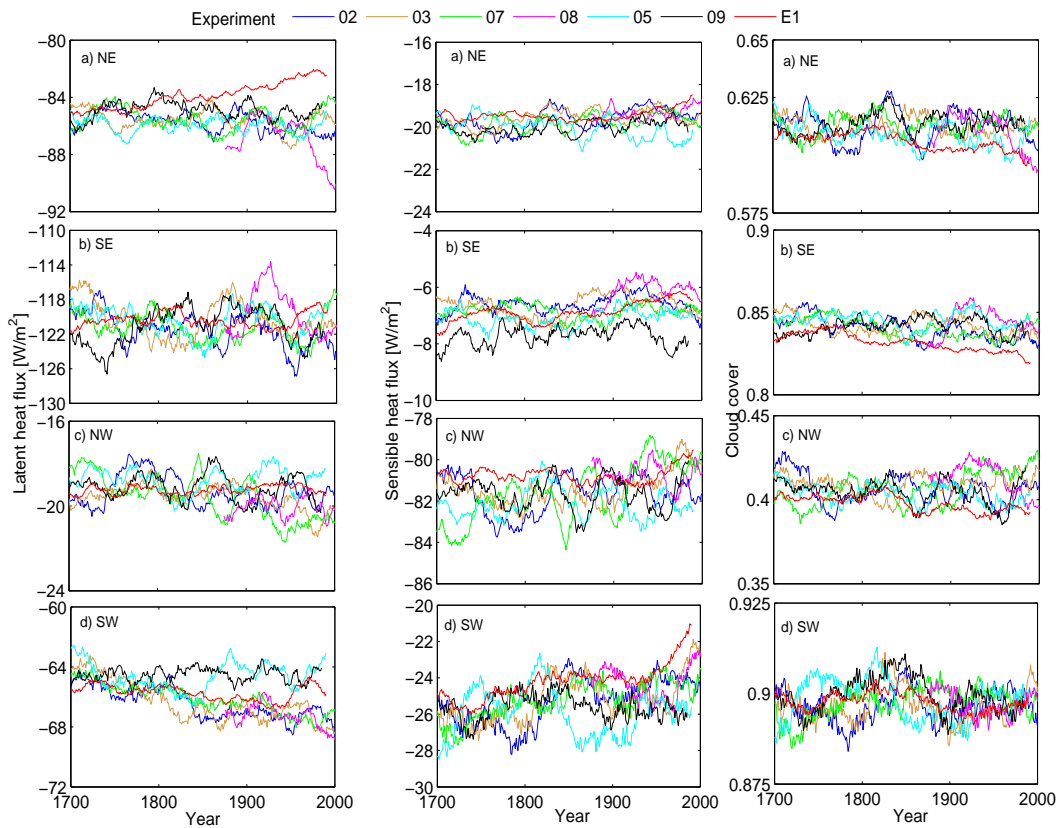


Fig. 3.12: Latent heat flux (left panel, W/m^2), sensible heat flux (middle panel, W/m^2) and cloud cover (right panel) in four regions: **(a)** Northeast (NE) China, **(b)** Southeast (SE) China, **(c)** Northwest (NW) China and **(d)** Southwest (SW) China in experiments as indicated (see Table 3.1). The anomalies are calculated with respect to the overall mean in 800-2005 and smoothed by 30 years. Depicted is only the time period after 1700, when clear temperature trends emerge.

comparison). In the experiment 08 (ALCC and CO_2) and the full-forcings ensemble E1, their influence dominate all four regions in China in the last 50 years (1950-2000) or 100 years (Fig. 3.12a-d, left and right panels, Fig. 3.11a-d, all panels). The big transitions of precipitation anomalies in parts of China (for example in NE and SW China in Fig. 3.10a and d, left panel) will be discussed in the following section about the dynamic cause (Asian monsoon).

To sum up, the total influence of ALCC is still unknown and it is unclear whether they impose a net cooling or warming effect; the same reasoning pertains to precipitation which is even less understood. All the uncertainties compromise the difficulties in quantifying and locating ALCC and further complexity is added by the interaction of biogeophysical and biogeochemical effects. Besides these, there are other problems, for example, the model differences and the coupling of the carbon cycle and the climate (Pongratz, 2009). Note that, there is no irrigated agriculture

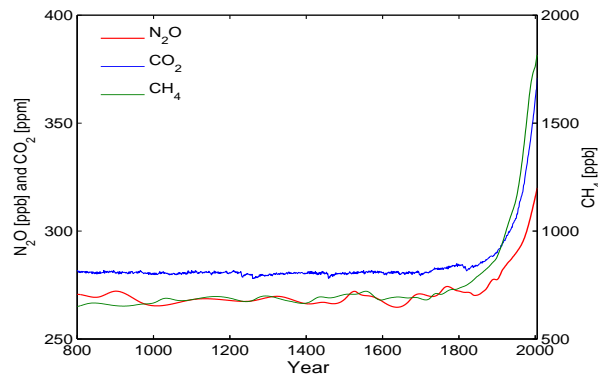


Fig. 3.13: Annual mean N_2O , CO_2 (left panel, unit: ppb and ppm) and CH_4 concentrations (right panel, ppb) in the atmosphere in ensemble E1.

in the simulations, instead it is parameterized as wheat or maize, which is rather important in eastern China.

3.6.2 Asian summer monsoon

Besides the ALCC and fossil fuel emissions discussed in the above sections, the precipitation in China is even more complex for its location in the areas with the strongest monsoon system in the world. The climate change may alter the Asian monsoon system. For example, the warming in the TP leads to less summer monsoon precipitation in East Asia (Wang et al., 2008). The latent heat released in the precipitation leads to ascent and shrinking of air columns above, strengthening the South Asia High in the upper levels (Rodwell and Hoskins, 1996; Wang et al., 2008). They strongly affect the Asian monsoon system in East Asia and therefore modify the precipitation. In the present analysis, the Asian summer monsoon is characterized by two indices: the Monsoon Hadley circulation index (MHI) and the East Asian Summer Monsoon Index (EAMI) (see Section 3.2 for a detailed method description). Both indices decrease after about 1800 AD, indicating the weakening east and south Asian summer monsoon in both ensembles (Fig. 3.15, left panel).

When compared to the single-forcing experiments (Fig. 3.15, right panel), the weakening of the east Asian monsoon occurs in the experiments 02 and 07 after the year 1800, while in the experiment 08 (plus fossil fuel CO_2), EAMI has a depression between two peaks around 1920 AD and decreases during the last 50 years. These are consistent with the trends of summer precipitation detected in the full-forcings experiments in NE and SW China (Fig. 3.10) where high correlations between EAMI and the summer precipitation are found (Fig. 3.16a). In the same period, EAMI is strengthened as a response to the solar forcing (after 1900 AD). The weakening of EAMI is due to an increase in the sea level pressure along longitude 110° and a strong decrease along 160° from 10° to 50°N (stronger in

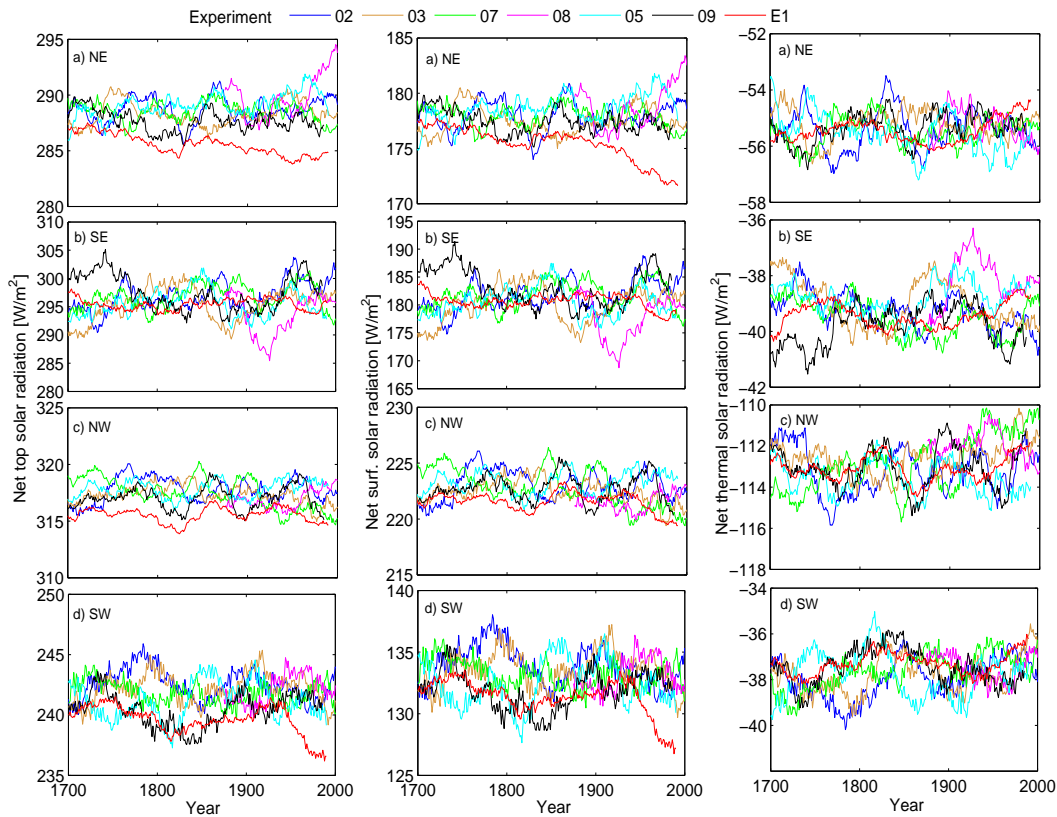


Fig. 3.14: Net top solar radiation (left panel, W/m^2), net surface radiation (middle panel, W/m^2) and net thermal radiation (right panel, W/m^2) in four regions: **(a)** Northeast (NE) China, **(b)** Southeast (SE) China, **(c)** Northwest (NW) China and **(d)** Southwest (SW) China in experiments as indicated (see Table 3.1). The anomalies are calculated with respect to the overall mean in 800-2005 and smoothed by 30 years. Depicted is only the time period after 1700, when clear temperature trends emerge.

poleward). The latter one has a similar sharp decrease around 1250 AD coinciding with the great unknown volcanic eruptions in 1258 AD (for the volcanic effects on the precipitation and the Asian summer monsoon see Chapter 4).

The weakening of the monsoon precipitation is also detected by Wang and Ding (2006) starting from 1950s. However, since 1980, the global land monsoon rainfall shows no significant trend, which contrasts with the rapid intensification of global warming during the same period. Meanwhile the oceanic monsoon precipitation shows an increasing trend after 1980. By considering a varying global monsoon domain, Hsu et al. (2011) obtained a consistently increasing trend in the global monsoon total precipitation over the past 30 years, which is different from the previous findings of Wang and Ding (2006) and Zhou et al. (2008) which are obtained for a fixed global monsoon domain. The weakening of the south Asian monsoon (MHI) in the present simulation starts about 100 years later, around 1900 AD compared

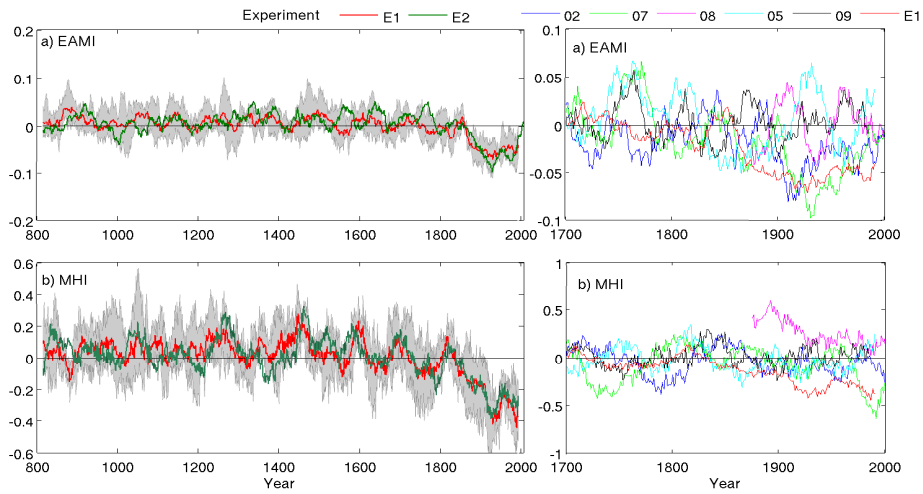


Fig. 3.15: (a) The East Asia summer Monsoon Index (EAMI) and (b) the Monsoon Hadley circulation Index (MHI) anomalies in ensemble E1/E2 (left panel) in 800-2005 AD and in sensitivity experiments after 1700 AD (right panel). Experiments are indicated (see Table 3.1). The right panel shows only the period after 1700 AD when clear EAMI and MHI trends emerge. All the anomalies are calculated with respect to the overall mean in 800-2005 and smoothed by 30 years.

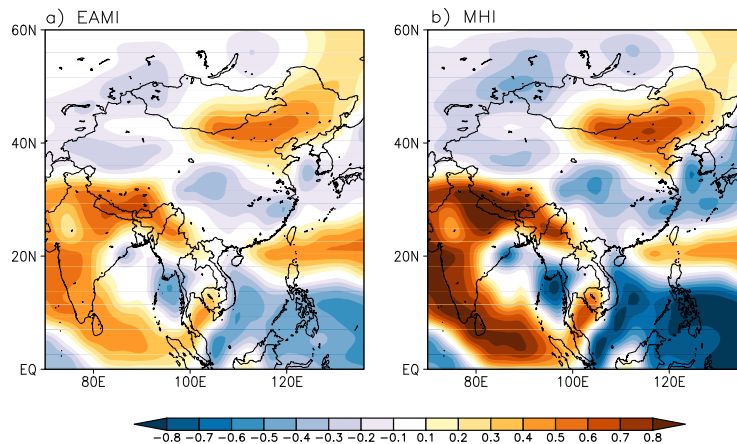


Fig. 3.16: Correlation coefficient between summer precipitation anomalies and (a) the East Asia summer Monsoon Index (EAMI) and (b) the Monsoon Hadley circulation Index (MHI) anomalies (at 95% level)

to EAMI (Fig. 3.15, right panel) and the severest weakening occur not in the experiment 02, but in experiment 08 (ALCC plus fossil fuel CO_2) indicating that the south Asian summer monsoon is more sensitive to CO_2 concentration than the east Asian monsoon. The weakening MHI has a strong positive correlation with precipitation

in NE and SW China and negative in SE China (Fig. 3.16b).

3.7 Summary and conclusion

The variability of the YC runoff and the embedding in regional and remote teleconnections is analyzed in a control simulation without variable external forcing using a complex atmosphere-ocean general circulation model (ECHAM5/MPIOM). The precipitation variability in China is investigated by two full-forcings ensemble simulations forced by different amplitudes total solar irradiance and compared to different reconstructed drought indices. The possible causes for the main simulated trend of precipitation in four regions in China is investigated in the view of internal forcings and dynamics. The ALCC, fossil fuel CO₂ emissions, and Asian summer monsoon changes in the last 200 years lead to the rainfall deficits with different combinations in the four regions.

Runoff and precipitation in Yangtze catchment

In the YC, the runoff, soil wetness, and temperature show memory up to decades with a scaling behavior (exponent $\beta \approx 0.6$), while precipitation reveals no memory. For longer time scales runoff, soil wetness, and temperature show weak long term memory similar to snow depth and snow melt on the TP. The variability of the monsoon is controlled by the ENSO mode. The ENSO cycle is detectable in the TP snow depth and snow melt, but not in the YC hydrology. The relationship analysis reveals that the YC temperature and the TP snow depth are correlated on annual but not on decadal time scales. There is strong impact of ENSO on temperature in the YC. For decadal means, the TP snow melt and Indian summer monsoon are correlated, and so do the YC temperature and ENSO. Temperature is anticorrelated with precipitation and soil wetness in the YC for annual and decadal means.

Precipitation variability and trend

From year 800 to 1800 AD, wet conditions dominate China, while a precipitation deficit is found only in central and west China (Fig. 3.6); In India and South Asia dryness dominates. From 1200 to 1800, the wet conditions prevail in eastern China (In Northeast after 1600). In the last 200 years (1800-2000), the model shows a reverse humidity conditions: the northwestern region becomes dry whereas large parts of China suffer from a severe precipitation deficit. Meanwhile, in India and South Asia, large amounts of rainfall are detected. In ensemble E2 with strong solar forcing, the precipitation bears an overall similarity in patterns. Regional anomalies are analyzed in four regions: NE, SE, NW and SW China. Precipitation is associated with interannual variability with some reminiscence of major volcanic eruptions in China in ensemble E1 (1258 and 1815). The MCA is not related to below average precipitation. However, a persistent period with relatively low precipitation with small uncertainties assessed by the ensemble spread is observed during the LIA.

The most distinct decrease in precipitation is simulated at about the 18th century. There is distinct rainfall decrease in all the four regions with the largest amplitude in SW China. The warming during this period supports the synchronicity of reconstructed warm and dry periods. However, this relationship is not found during the cold period 1200-1300. The regional variability of precipitation shows the familiar maritime/continental contrast with lowest values in the West and highest values in the Southeast, where the decreasing trend after 1800 is the second largest.

Reconstructed drought index from Zheng et al. (2006) reveals high intra-annual variability, the dry periods are found in the 11th-13th centuries and the 15th century in east China, which are not confirmed by Cook et al. (2010). The index from Cook et al. (2010) shows a dry period in the 19th century. The index from Central Meteorological Bureau (1981) shows small variability during the whole period. In the last two centuries, the summer in China has wet conditions with a decrease in the last 50 years shown by Zheng et al. (2006). However, the most distinguishing simulated precipitation feature, the decrease at the same period in both ensemble simulations, is not detected by neither of the reconstructed data, although the index by Cook et al. (2010) has a sharp decrease in the last 30 years.

The power spectrum analysis of ensembles E1 and E2 and the reconstructions show that the simulated total summer precipitation (Fig. 3.8a) shows a flat spectrum ('white noise'), hence variability is without the long-term memory present in the near surface temperature. The single deflection is an increase in power within the frequency range corresponding to ENSO, which is the same as temperature (see Section 2.5 and Fig. 2.6). Clearly, temperature and precipitation are decoupled on long inter-annual time scales. The reconstructed drought index for East China (Zheng et al., 2006) shows periods $T \approx 2, 3, 4,$ and 7 years on a continuous background which decreases as $S(f) \sim f^{-\beta}$ with $\beta \approx 2$ (analyzed in 800-2000 AD). Periodic components in precipitation are not resolved in the available temperature data. The reconstructed drought index from Central Meteorological Bureau (1981) and Cook et al. (2010) reveal similar power spectra with $\beta = 0.5$ and $\beta = 0.4$, indicating similar long term memory in both reconstructions.

Causes for the summer rainfall deficits

The possible causes for the weakening of summer rainfall in the four regions in China is summarized in Table 3.4. Sensitivity experiments are analyzed using the five sensitivity experiments. The ALCC turns out to be the one crucial factor through both the biogeophysical and biogeochemical effects. The biogeophysical effect refers to the modification of the physical properties of the land surface. The increasing surface albedo and the other biogeophysical effects of ALCC (other than surface albedo) compensate each other and lead to a local warming. This opposing effects widely cancel each other on a global scale, but the regional climate is significantly influenced by the second factor and may even affect via teleconnections (see more discussions in Chase et al., 2000 and Pongratz, 2009). The biogeochemical effect of ALCC has the most important influence from the carbon cycle, and the

associated impact on the global CO₂ concentration. By altering atmospheric CO₂, ALCC modifies the Earth's energy balance and thus the climate. The biogeophysical and biogeochemical effects of ALCC attribute to the rainfall deficits in NE, SE and SW China (the biogeochemical mechanism only in NW China).

Besides ALCC, the fossil fuel emissions is another plausible cause in all the four regions China. The CO₂, CH₄ and N₂O concentrations in the atmosphere increase at a very high speed in the present simulations and thus amplify the rainfall deficits caused by ALCC in the last several decades in different regions.

Furthermore, the east and south Asian monsoon system in the present simulations characterized by the Monsoon Hadley circulation index (MHI) and the East Asian Summer Monsoon Index (EAMI) both show significant decreasing trend in the same period as the precipitation deficit. They both have a positive influence on the summer rainfall in NE and SW China and a negative influence in SE China.

However, there are still uncertainties: First, the uncertainties from the internal part of biogeophysical effects of ALCC (e.g., the opposing effects from surface albedo and from the evaporation), the uncertainties from the combined effects of biogeophysical effect and biogeochemical effect. Thus the total influence of ALCC is still unknown and it is not clear whether they impose a drying effect in China or not. Secondly, the greenhouse gases can cool or warm the atmosphere depending on their properties; they can suppress precipitation, however, they have also been reported to increase rainfall. The Asian monsoon system is rather complex and the simulated results are far from satisfactory. All the uncertainties compromise the difficulties in quantifying and locating the causes for the rainfall deficits.

Table 3.4: Summary of: **(I)** the trend of climate variables after 1800 AD in Northeast (NE), Southeast (SE), Northwest (NW) and Southwest (SW) China: Precipitation (PRCP), large scale precipitation (APRL), convective precipitation (APRC), surface albedo (ALBEDO), evaporation (EVAP), latent heat flux (AHFL), sensible heat flux (AHFS), cloud cover (CC), net top radiation (clear sky, SRO), net surface radiation (clear sky, SR), net thermal radiation (clear sky, TR), net top radiation (SRO-c), net surface radiation (SR-c) and net thermal radiation (TR-c). Experiments are indicated by different colors: full-forcings ensemble E1 (red), sensitivity experiment 02 (blue), 07 (green) and 08 (magenta). Experiments details see Table 3.1. **(II)** the possible causes for precipitation decrease in four regions in China after 1800 AD. '+'/'-' indicates positive/negative influence and question marks indicate uncertainty.

[Summary I]

Regions	PRCP	APRL	APRC	ALBEDO	EVAP	AHFL	AHFS
NE	↘ ↙ ↗ ↖	→	↘	↗ ↘ ↙ ↖	↗ ↘ ↙ ↖	↗ ↘ ↙ ↖	↗ ↘ ↙ ↖*
SE	↘ ↙ ↗ ↖	↘	↘	↗ ↘ ↙ ↖	↗ ↘ ↙ ↖	↗ ↘ ↙ ↖	↗ ↘ ↙ ↖*
NW	↘ ↙ ↗ ↖	↘*	↘	↗ ↘ ↙ ↖	↘	↘	↗ ↘ ↙ ↖*
SW	↘ ↙ ↗ ↖	↘	↗	↗ ↘ ↙ ↖	↘ ↙ ↗ ↖	↘ ↙ ↗ ↖	↗ ↘ ↙ ↖*

Regions	CC	SRO-c	SRO	SR-c	SR	TR-c	TR
NE	↘ ↙ ↗ ↖	↗ ↘	↘ ↙ ↗ ↖	↘	↘ ↙ ↗ ↖	↗ ↘	↗ ↘ ↙ ↖*
SE	↘ ↙ ↗ ↖	↗ ↘	↘ ↙ ↗ ↖		↘ ↙ ↗ ↖	↗ ↘	↗ ↘ ↙ ↖*
NW	↘ ↙ ↗ ↖*		↘ ↙ ↗ ↖		↘ ↙ ↗ ↖	↗ ↘	↗ ↘ ↙ ↖*
SW		↗ ↘*	↘ ↙ ↗ ↖	↘*	↘ ↙ ↗ ↖	↗ ↘	↗ ↘ ↙ ↖*

[Summary II]

Regions	ALCC	(only biogeochemical effect)	Fossil fuels CO ₂	Monsoon	
				EAMI	MHI
NE	yes	(yes)	yes*	yes(+)	yes(+)
SE	yes	(yes)	yes*	yes(-)?	yes(-)
NW			yes*		
SW	yes	(yes)	yes*	yes(+)	yes(+)

*starting from 1900 AD

Chapter 4

Volcanic and ENSO effects: Global and East Asia

4.1 Introduction

Volcanic eruptions are the dominant external climate perturbations on the interannual time scale since the stratospheric dust veils reduce temperature for years and alter summer precipitation patterns globally (Angell and Korshover, 1985; Dai et al., 1991; Robock, 2000; Santer et al., 2001; Fischer et al., 2007; Robock et al., 2008; D'Arrigo et al., 2009; Timmreck et al., 2009). In the temperature record the most intense eruptions are detectable while impacts on precipitation and pressure are less clear (Mass and Portman, 1989; Shindell et al., 2004; Schneider et al., 2009). In general the winter temperature after an eruption is above normal in North America and Eurasia whereas North Africa and Southeast Asia are cooler (Robock and Mao, 1995; Thompson, 1995; Robock, 2000; Shindell et al., 2003; Schneider et al., 2009). However, while the majority of analyses of the post-volcanic climate pertain to Europe and North America, less is known about China/East Asia although there is a wealth of reconstructions and documentary sources (for a review on volcanic impacts during 1200-1700 AD see Atwell, 2001 and Yoshimori et al., 2005). In Northeast China a cooling and drying is found after volcanic eruptions (Mao et al., 2009). In Southeast Asia there are transitions from wetter conditions towards drier conditions (Anchukaitis et al., 2010; Peng et al., 2010) during the eruption year and the subsequent year. The data in this region is useful to validate atmosphere-ocean general circulation models (GCMs) simulations of volcanic eruptions (see the concerns put forward by Anchukaitis et al., 2010).

Large volcanic eruptions inject sulphur gases into the stratosphere, which convert to sulphate aerosols with an e-folding residence time of about one year, and the resulting disturbance to the Earth's radiation balance affects surface temperatures as well as the atmospheric circulation (Robock, 2000; Robock et al., 2008). The recovery of the climate after an abrupt external perturbation like a volcanic eruption proceeds on time scales determined by the memory of land surface and ocean, and that of the carbon cycle, which causes a multi-decadal decrease in atmospheric CO₂ (Frölicher et al., 2011). This time scale determines the accumulative effect of climate anomalies and is, for example, relevant for precipitation deficits. Robock and Mao (1995) find a time scale of two years in 140 year observations. In a model simulation Robock and Liu (1994) detect a time scale of four years for the relaxation of temperature to climatological means and less than three years for precipitation. Crowley et al. (2008) assume a 10 years recovery time scale for the ocean mixed layer in an analysis of the cumulative effect of sequences of eruptions during the 19th century. During the Dalton minimum (1790-1830) at the end of the Little Ice Age a series of volcanic eruptions occurred which lowered temperature persistently since the oceanic mixed layer could not recover (Crowley et al., 2008; Cole Dai et al., 2009). After the most intense volcanic eruptions of the last millennium, 1258 (unknown) and in 1815 (Tambora), the cold temperature anomalies recovered on decadal time scales, which is attributed to the ocean heat uptake in a coupled ensemble experiment (Stenchikov et al., 2009) and the carbon cycle feedback in the present model configuration (Brovkin et al., 2010; Frölicher et al., 2011).

Volcanic eruptions and El Niño/Southern Oscillation (ENSO) events can influence the climate on similar time scales and with comparable magnitudes. The combined signal can be greater in magnitude with different geographical patterns than suggested from a simple linear combination (Kirchner and Graf, 1995). Furthermore, an increase of the probability of El Niño events after volcanic eruptions is detected in reconstructions (Adams et al., 2003; McGregor et al., 2010), although an association between low-latitude volcanic events and lower SST in the tropical oceans is also found (D'Arrigo et al., 2009). Enhanced probability of occurrences for El Niños after eruptions is supported by simulations with the Zebiak-Cane model (Mann et al., 2005; Emile Geay et al., 2008), however, there remain uncertainties associated with the minimum intensity of eruptions and the enhancement of the likelihood (Emile Geay et al., 2008). This impact is highly relevant for Southeast Asia since the ENSO is related to drought during El Niño and wetness during La Niña phases, thus both phenomena can lead to either a partial cancellation or to an enhancement with even more disastrous consequences. Since reliable reconstructions of past El Niño events are restricted to the last three centuries (Quinn, 1993), AOGCM simulations are necessary to retrieve correlations and possible causal relationships.

The most intense eruption in historic time was Tambora in 1815 (Rampino and Self, 1982; Stothers, 1984) which caused the 'year without summer' in North America and Europe with dramatic consequences for food supply and health (Oppenheimer, 2003; Soon and Yaskell, 2003). As a major eruption located in the tropics

(D'Arrigo et al., 2009), the Tambora impact was global (Robock, 2000). Documentary reports exist in China which describe disasters in various regions after 1815 (Yang et al., 2005): In the province Yunnan (in the South), there was a three years famine (1815-1817) due to a poor harvest of rice and maize caused by low summer and autumn temperatures (anomalies range $-2...-3^{\circ}\text{C}$). In the province Hainan Dao a dry and cold winter is documented for 1815-1816 and in Taiwan and Zhanghua uncommon ice storms with 'thick ice on the road' have been observed in December. Summer snowfall was observed at various locations in Shuangcheng (in the Northeast, now in the Heilongjiang province) and in the provinces Jiangxi and Anhui (both in the South). Cold anomalies have also been found in the eastern parts of China, including the Yangtze catchment, but famines are not documented in these regions. In the decade after 1815, frequent and strong fluctuations of wet and arid conditions occurred in China, and increased numbers of floods and droughts are reported in the Yangtze delta (Jiang et al., 2006). Since famines and social disasters might have different causes an analysis of past temperature and precipitation anomalies on a regional scale yields useful hints to understand the evolution of historical events and to adapt to future natural catastrophes.

The aim of this chapter is to assess the impacts and the co-operative effects of volcanic eruptions and ENSO events in ensemble climate simulations for the last 1200 years with a complex atmosphere-ocean-land model and to compare it with reconstructions in east Asia. Section 2 describes the earth system model, the volcanic forcing, the methods and the reconstructed data. Section 3 presents the global patterns of the temperature and precipitation responses to volcanic eruptions without ENSO events. The relaxation time scales of the temperature decay are determined globally by exponential fits. Section 4 focuses on the comparison between simulated and reconstructed temperature and drought indices in East Asia for: (i) volcanic impacts without ENSO events, (ii) ENSO impacts without preceding eruptions and (iii) concurrent eruptions and ENSO events. A further focus lies on an analysis of the climate after the Tambora eruption (1815) to detect causes for famines reported in China/Southeast Asia (Section 5). As the eruptions in the ensemble simulations concur with different simulated ENSO states, a selection of an optimal combination is possible by comparing the model results with documented El Niño events (the selection of optimal ensemble members has been suggested by Goosse et al., 2006). The results are summarized and discussed in Section 6.

4.2 Data and methods

Model and simulations

The millennium experiments are carried out using the Earth System Model (Jungclaus, 2009; Jungclaus et al., 2010). The model includes the atmospheric model ECHAM5 (Roeckner et al., 2003), the ocean model MPIOM (Marsland et al., 2003)

and modules for land vegetation JSBACH (Raddatz et al., 2007) and ocean biogeochemistry HAMOCC (Wetzel et al., 2006), which are coupled via the OASIS3 coupler. The carbon cycle is interactively simulated. ECHAM5 is run at T31 resolution ($\approx 3.75^\circ$) with 19 vertical levels up to 10hPa. The ocean model MPIOM has a horizontal grid spacing of about 3° with 40 unevenly spaced vertical levels and applies a conformal mapping grid with a horizontal resolution ranging from 22 km to 350 km. This grid set-up is a low resolution version of the model used for the scenario simulations for the Intergovernmental Panel of Climate Change (IPCC, Solomon et al., 2007) and the Coupled Carbon Cycle Climate Modeling Intercomparison Project (CCMIP, Friedlingstein et al., 2006; Jungclaus et al., 2010). The model is forced by reconstructions of (I) Total solar irradiance (TSI), (II) volcanic forcing considering aerosol optical depth (AOD) and effective radius distribution, (III) land cover change, and (IV) anthropogenic green house gases and aerosols. More details on the model and forcings see Section 3.2 in Chapter 3.

The analysis uses two ensembles: ensemble E1 with five members forced by the state-of-the-art solar forcing reconstructed by Krivova et al. (2007) with a weak variation about 0.1% of the standard TSI value of 1367W/m^{-2} (given by the difference between present-day and Maunder minimum, Fig. 4.1a); ensemble E2 with three members forced by the solar forcing reconstructed by Bard et al. (2000) which has a higher variability of 0.25% (see (I) in Section 3.2 in Chapter 3); the remaining natural and anthropogenic forcings are identical. The full-forcings experiments cover the period from 800 to 2005 AD (Bard et al., 2000; Jungclaus et al., 2010). The different initial conditions for the ensemble members are derived from a 3000 years control integration forced by constant conditions for 1860. Zhang et al. (2010) compared both ensembles with climate reconstructions in China and concluded that ensemble E1 reproduces the reconstructed climate variability. Therefore, the present analysis is restricted to this five member ensemble E1 unless indicated otherwise. All anomalies are calculated with respect to the time means which are determined individually for each ensemble member in the whole period 800-2005 AD.

Volcanic eruption list for simulation

The volcanic effects are taken into account in a data set of Aerosol Optical Depth (AOD) at $0.55 \mu\text{m}$ and effective radius for 10-day time steps and split into four equal area segments ($30\text{-}90^\circ\text{N}$, $0\text{-}30^\circ\text{N}$, $0\text{-}30^\circ\text{S}$, $30\text{-}90^\circ\text{S}$) (Fig. 4.1b, c). Growth and decay time for each eruption is calibrated and fitted to recent observations. The data set includes information about mean particle radius evolution vs. time, a feature particularly important for large eruptions (Crowley et al., 2008; Timmreck et al., 2009, for details see) have shown for the 1258 eruption that a shift of the volcanic aerosol size distribution towards larger particles reduces the cooling effect and improves the consistency with temperature reconstructions.

In the annual top solar irradiance series, 21 large volcanic eruptions are defined for each member in ensemble E1 and E2 (see Table 4.1, 105 eruptions in total in E1 and 63 in E2) based on the strongest reduction in net top solar radiation

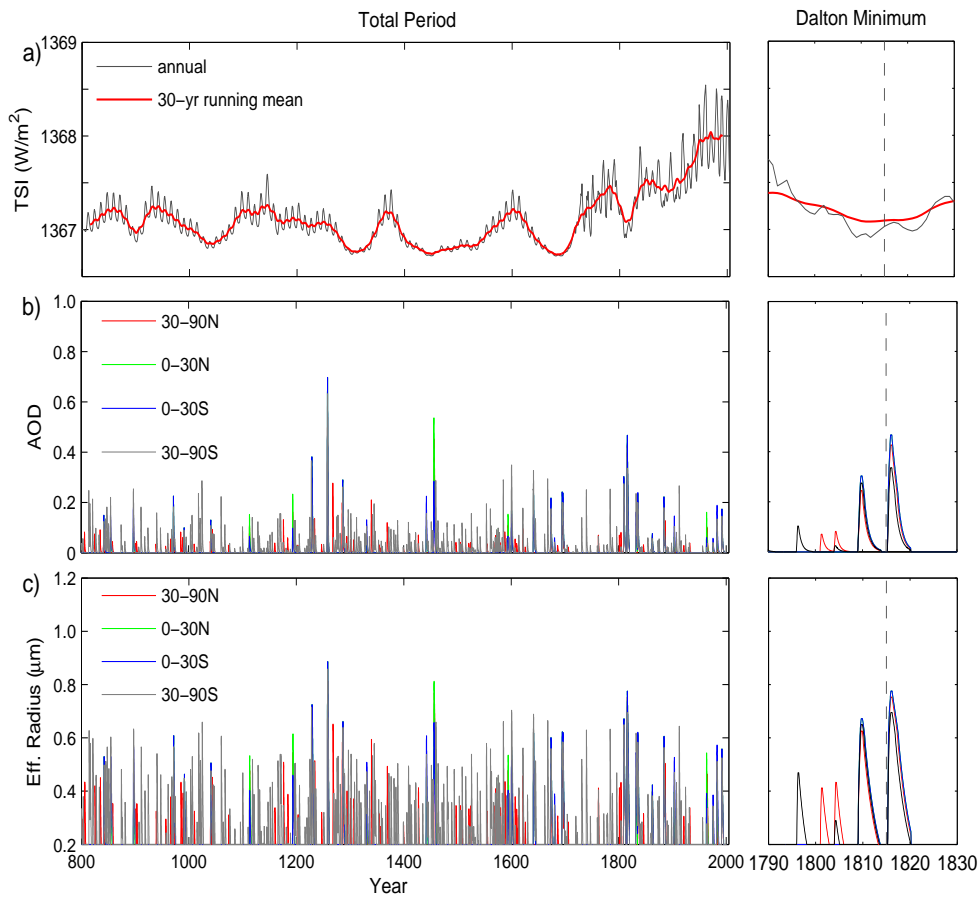


Fig. 4.1: (a) Annual mean total solar irradiation in ensemble E1 (30 years running mean: red) for the whole simulation period (left panel) and the Dalton minimum (1790-1830, right panel) based on the reconstruction by Krivova et al. (2007), (b) Aerosol optical depth (dimensionless fraction), and (c) Effective radius (μm), in (b) and (c) latitude belts are separated. The Dalton Minimum includes the Tambora eruption in 1815.

(for a detailed review on past eruptions see Newhall and Self, 1982, Peng et al., 2010 and Global Volcanism Program, Smithsonian National Museum of Natural History/Washington, 2011). The lowest reduction in this set is -2.0W/m^2 from Santa Maria in Guatemala in 1903 (average of all eight simulations), which is slightly larger than the observed reduction of -1.7W/m^2 . The highest reduction with values between -16.4 and -16.9W/m^2 in all eight members is caused by the volcanic eruption in 1258 (unknown volcano). Brovkin et al. (2010) find a global temperature drop of 1 K for this eruption and a relaxation time of 10 years within the present model setup. As in Peng et al. (2010) the year with the largest reduction in irradiance is defined as the volcanic eruption year. This definition may lead to a discrepancy between observation years and eruption years in the present analysis, since

the aerosol layer accumulates leading to a delayed response. A particular scheme for the removal of clustered eruptions is not implemented since there are only two pairs of eruptions within the recovery time scale which is below three years in China apart from the Northeast (eruptions pairs in 1809-1816 and 1832-1835, see Table 4.1 and recovery time scales in Fig. 4.5). Intensities and latitudes of the volcanoes are not considered. To determine the effects of volcanic eruptions, a composite analysis of surface temperature and precipitation are performed in the year after the eruption (if not indicated otherwise).

Table 4.1: List of the 21 selected volcanic eruptions in 800-2005 in the model simulations in each member (the eruption year is defined by a decrease in net top solar irradiation of at least -2.0 W/m^2). The Volcanic Explosivity Index (VEI) is included and question marks indicate uncertainty (Newhall and Self 1982; Peng et al. 2010; Smithsonian National Museum of Natural History/Washington, Global Volcanism Program, 2011).

No.	Year	Name	VEI
1	842	Unknown	
2	854	Unknown	
3	897	Unknown	
4	971	Unknown	
5	1193	Unknown	
6	1228	Unknown	
7	1258	Unknown	
8	1286	Unknown	
9	1442	Unknown	
10	1456	Pinatubo?	6
11	1600	Huaynaputina	6
12	1641	Parker	6
13	1673	Gamkonora	
14	1694	Serua?/Hekla?	
15	1809	St. Helen?	
16	1815	Tambora	7
17	1832	Babuyan Claro	4?
18	1835	Cosiguina	
19	1884	Krakatau	6
20	1903	Santa Maria/2 others	4
21	1992	Pinatubo	6

El Niño/Southern Oscillation (ENSO)

ENSO is defined by the principal component time series (PC1) of the first EOF of the tropical Pacific sea surface temperature (SST) variability in winter (DJF) and denoted as PC1-SST (see Hoerling et al. 2001). El Niño events are given for PC1-

$SST > 1$, La Niña events for $PC1-SST < -1$, and a neutral state for $|PC1-SST| < 1$.

The problem of removing ENSO-related variations from climate records has been addressed in previous studies using a variety of methods (see for example Penland and Matrosova 2006; Compo and Sardeshmukh 2010). Here the two ensemble simulations with eight members allow the identification of a sufficient number of intense eruptions with different ENSO responses. A simple and straightforward method is used to avoid years with overlaps: First the response of climate during the year after an eruption for neutral ENSO states ($|PC1-SST| < 1$) in two preceding winters is considered. Secondly, the ENSO impact is determined during years without preceding eruptions. The final analysis considers years with concurrent eruptions and ENSO events. To determine the co-operative effects of volcanic eruptions and ENSO anomalies, a composite analysis of surface temperature and precipitation are performed in the year after the eruption (if not indicated otherwise).

Standardized Precipitation Index (SPI)

A variety of indices are used to assess drought or to capture abnormal wetness. Sims et al. (2002) suggest that the Standardized Precipitation Index (SPI) is a better indicator for short-term precipitation anomalies and soil wetness than the Palmer Drought Severity Index (PDSI), while Zhai et al. (2010) suggest that the PDSI and the SPI can be used to describe dryness and wetness. In the present analysis, simulated precipitation anomalies are analyzed in terms of Standardized Precipitation Index (SPI, McKee et al., 1993). To obtain this index, the monthly precipitation is transformed to a standard normal distribution to yield monthly SPI values by preserving probabilities, which ensures that the SPI gives a uniform measure for dryness and wetness in different climate regimes. In the analysis we use the monthly time scale characterizing the meteorologically relevant period, and the summer SPI is averaged monthly SPI in JJA (June, July and August) during which the summer precipitation occupies 80% of the annual mean. The definition and classification of SPI are shown in Table 4.2, the transformation to SPI is shown in Fig. B.1 in Appendix and for a detailed method description see Bordi et al. (2004), Sienz et al. (2007) and Zhu et al. (2010).

Asian Summer Monsoon indices

The Asian summer monsoon is characterized by two indices: The Monsoon Hadley circulation index (MHI) is defined as $MHI = V_{850} - V_{200}$ (Goswami et al., 1999), where the meridional velocities V are determined at 850 and 200hPa in $70^\circ - 110^\circ E$ and $10^\circ - 30^\circ N$. The MHI describes the South Asian (Indian) summer monsoon as part of the Hadley cell. The East Asian Summer Monsoon Index (EAMI) which describes the subtropical circulation is defined by the difference in sea level pressure in $160^\circ E$ minus $110^\circ E$ in $10^\circ - 50^\circ N$ (Guo et al., 2004; Wei and Zhang, 2010).

All anomalies are with respect to the time means which are determined individually for each ensemble member in the whole period 800-2005 AD.

Table 4.2: Standardized Precipitation Index (SPI) classification and event-probability (P in %, McKee et al. 1993)

SPI	SPI-Classes	P-Value
$SPI \geq 2$	W3: extremely wet	2.3
$1.5 \leq SPI \leq 2$	W2: severely wet	4.4
$1 \leq SPI \leq 1.5$	W1: moderately wet	9.2
$-1 < SPI < 1$	W0, D0: normal	68.2
$-1.5 \leq SPI \leq -1$	D1: moderately dry	9.2
$-2 \leq SPI \leq -1.5$	D2: severely dry	4.4
$SPI \leq -2$	D3: extremely dry	2.3

Reconstructed temperature

The reconstructed temperature time series in the last millennium used in present analysis are from Yang et al. (2002), Ge et al. (2003), Wang et al. (2007b) and Mann et al. 2009. All anomalies are with respect to the time means in the corresponding data set during the whole period.

The temperature from Yang et al. (2002) is reconstructed in China for 800-1999 with 10-yr resolution (the complete reconstructed period is 0-1999 AD) based on ice core, tree rings, peat and lake chronologies, biota and other climate indices (Yang et al., 2002).

The winter half-year (October to April) from Ge et al. (2003) is reconstructed over eastern part of China with 30-yr resolution for 800-1999 AD (10-yr resolution in 960-1100, the complete reconstructed period is for 15-1999 AD) using the phenological cold/warm events recorded in Chinese historical documents (Ge et al., 2003).

The temperature from Wang et al. (2007b) is reconstructed in ten regions in China with 10-yr resolution spanning the time 1000-2005 AD using a variety of proxy data, such as ice core, tree-rings, stalagmites, peat, lake sediments, pollen and historical records validated with instrumental observations. It presents a detailed regional temperature reconstruction in Northeast, North, East, South China, Taiwan, Central, Southwest, Northwest China, Xinjiang, and Qinghai-Tibet Plateau (Wang et al., 2007b).

The temperature from Mann et al. (2009) is reconstructed for the last 800-2005 AD. The complete reconstructed period is 500-2006 AD at hemispheric and global scale using a greatly expanded set of proxy data for decadal-to-centennial climate changes, recently updated instrumental data, and complementary methods that have been tested and validated with model simulation experiments (Mann et al., 2008, 2009).

Reconstructed drought index

The reconstructed drought indices used in the present analysis are from the Central Meteorological Bureau (hereafter CMB, 1981), Zheng et al. (2006) and Cook et al. (2010). All anomalies are with respect to the time means in the corresponding data set during the whole period.

The annual drought index from the CMB (1981) is reconstructed for 1470-1979 AD (May-September) compiled from reports about the weather found in local gazettes in 120 districts in China. The index includes the averaged value in China and sub-regions, Northeast (NE), North China (N), central north (CN), central east (CE), central south (CS), south (S), northwest (NW), southwest (SW), and inner lands (In) (for the locations see CMB, 1981). The original index varies from 1 (extreme wet) to 5 (extreme dry).

The annual drought index from Zheng et al. (2006) is reconstructed for 501-2000 AD in the eastern part of China based on Chinese historical documents and instrument measurements. The index includes the averaged value in eastern part of China and four sub-regions, the Huaibei (HB, same location as N defined by CMB, 1981), Jianghuai (JH) and Jiangnan (JN) areas (for the locations see Zheng et al., 2006). The original index varies from -2 (extreme dry) to 2 (extreme wet).

The Palmer Drought Severity Index (PDSI) from Cook et al. (2010) is reconstructed for 1300-2005 AD in JJA based on tree rings in the forested areas of the Asian Monsoon area (see Cook et al., 2010 for details). The index varies from -4 (extreme dry) to 4 (extreme wet).

Volcanic eruption list for reconstruction

The volcanic eruptions are selected based on Ammann et al. (2007), Ammann and Naveau (2003), and Fischer et al. (2007) (see Table 4.3). The volcanic eruptions with El Niño events are selected based on the reconstructed El Niño from Gergis and Fowler (2006) (see Table 4.4). The lists are denoted using the initial of the first author plus the number of event years, e.g., the first list is denoted 'A15' according to Ammann et al. (2007) with 15 eruption years. The anomalies refer to the whole time period.

4.3 Global volcanic response

The global climate response during the year after a volcanic eruption is considered without ENSO events (neutral, $|\text{PC1-SST}| < 1$) in two preceding winters, which leads to 31 eruption years in total in ensemble E1 (22 in E2).

Table 4.3: List of volcanic eruptions without El Niño events used for the reconstructed temperature and the Palmer Drought Severity Index (PDSI) in summer (JJA). The sources for volcanic eruptions are ⁽¹⁾ Ammann et al. (2007), ⁽²⁾ Ammann and Naveau (2003) and ⁽³⁾ Fischer et al. (2007); * While the data is available after 1250, the reconstructed PDSI starts from 1300 (missing years in italics).

Name	A15 ⁽¹⁾		AN46 ⁽²⁾		F12 ⁽³⁾
Number of eruptions	15/10*		46		12
Eruption years	1258	1443	1665	1815	1596
	1259	1452	1674	1823	1600
	1269	1459	1680	1831	1641
	1278	1463	1693	1835	1673
	1279	1490	1712	1861	1809
	1452	1504	1721	1880	1815
	1453	1512	1728	1883	1823
	1600	1522	1744	1911	1831
	1601	1554	1749	1928	1835
	1641	1568	1752	1953	1883
	1809	1571	1760	1963	1963
	1810	1595	1774	1968	1982
	1815	1600	1789	1974	
	1816	1605	1794	1982	
	1884	1622	1808		
		1641	1813		

Table 4.4: List of volcanic eruptions with El Niño events used for the reconstructed temperature and the Palmer Drought Severity Index (PDSI) in summer (JJA). The sources for volcanic eruptions are ⁽¹⁾ Ammann et al. (2007), ⁽²⁾ Ammann and Naveau (2003) and ⁽³⁾ Fischer et al. (2007). The event years with reconstructed El Niño are according to Gergis and Fowler (2006).

Name	A1 ⁽¹⁾	AN7 ⁽²⁾	F2 ⁽³⁾
Number of eruptions	1	7	2
Eruption years	1903	1586	1586
		1619	1903
		1660	1903
		1737	
		1890	
		1902	
		1903	

4.3.1 Temperature and SPI

Volcanoes cool the northern Hemisphere in North America and Eurasia during the year after eruptions (Fig. 4.2a). Areas with weak positive amplitudes are found in

the tropical Pacific, the Bering Sea, and in parts of the Antarctic Ocean. Here the non-significant positive values in the tropical Pacific Ocean indicate an El Niño-like warming, which is consistent with Adams et al. (2003). Significant areas marked by 'x' are based on the Mann-Whitney test at the 95% level. The response pattern of the SPI is more complex than temperature (Fig. 4.2b). Drier conditions are found in central Asia, East China, Australia and North Africa. Drier ocean basins are in the east and the northwest Pacific, the central Atlantic and the Antarctic Ocean. In the central Pacific both drier and wetter conditions occur.

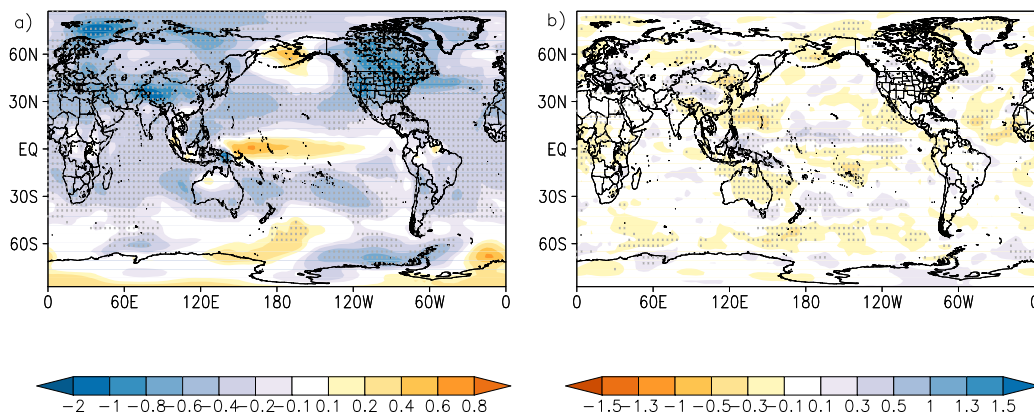


Fig. 4.2: (a) Global annual mean temperature anomalies [$^{\circ}\text{C}$] and (b) summer Standardized Precipitation Index (SPI, JJA) in ensemble E1 in the year after volcanic eruptions without ENSO events. Significant areas are marked by 'x'.

4.3.2 Winter warming

Stenchikov et al. (2006) observe warming in Eurasia for two winters following the eruption which appears to be weaker in the nine models used in the Intergovernmental Panel on Climate Change Fourth Assessment Report (IPCC AR4, 2007, Solomon et al., 2007). In our simulation, warming in the following winter is found in both ensembles in the Arctic Ocean, the Bering Sea, the tropical Pacific, and the Southern Pacific Ocean between 180° - 120°W (Fig. 4.3a and b). The warming in Eurasia, which is evident in observations (Stenchikov et al., 2006) and reconstructions (Fischer et al., 2007), is only partly simulated. In the east of the continent both ensembles show a weak warming. However, the expected warming over Europe is not simulated, which is a hint that the model is not able to simulate the dynamical response of the North Atlantic Oscillation (NAO) in a correct way (positive phase of the NAO after an eruption, see e.g., Stenchikov et al., 2006). For ensemble E2 with strong solar forcing, the warming extends to Siberia and central Asia. In Asia, warming is found in southeast China, Thailand and Malaysia in E1. In the second

winter, the warming amplitudes decrease in E1 but remain strong in E2 (in the Arctic Ocean). Note that the individual ensemble members show different amplitudes of warming.

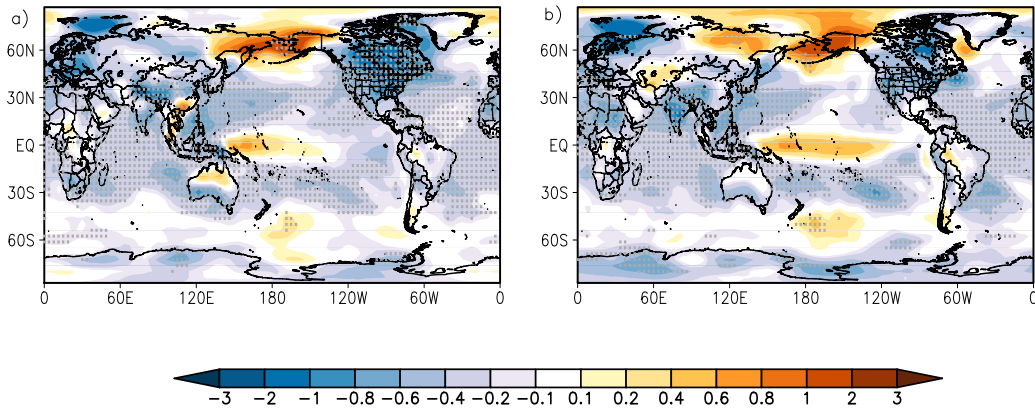


Fig. 4.3: Winter temperature anomalies [$^{\circ}\text{C}$] after volcanic eruptions without ENSO events (neutral, $|\text{PC1-SST}| < 1$) in ensemble (a) E1 and (b) E2. Significant areas are marked by 'x'.

4.3.3 Recovery timescale

The recovery of the local temperature drop after an eruption is described in terms of an exponential decay, $\Delta T(t) = \Delta T_0 * \exp(-t/\tau)$, beginning with the first year after the eruption ($t=0$) and ending at the tenth year ($t=9$) (see Fig. 4.4 for two examples of fitted temperature episodes). At every grid box, the amplitude ΔT_0 and the time scale τ are fit parameters for the average of the temperature relaxation anomalies.

The global distribution of the fitted decay amplitudes ΔT_0 and the relaxation time scales τ are shown in Fig. 4.5a and b at grid points where fits can be achieved (fits require a negative amplitude and a sufficient decay of the anomalies). Areas marked by 'x' have an R-Square value above 0.4 (Goodness-of-fit statistics at 95% level). Large amplitudes ΔT_0 reaching -2°C are found in North America, the Himalaya, and the Barents Sea, and in the Southern Pacific Ocean between 160° - 60°W . Land and ocean reveal similar amplitudes. Areas with negligible amplitudes inhibit fits (void in Fig. 4.5a and b); furthermore areas with weak positive amplitudes are excluded (mostly in the tropical Pacific, the Bering Sea, and in parts of the Southern Pacific as in Fig. 4.5a). Note that this amplitude is the result of a fit and not identical to the anomaly during the year after eruption, though similar. Ensemble E2 reveals similar results, not shown).

The recovery time scales τ (Fig. 4.5) reveal a long-lasting influence up to a decade in Southern Europe, Northeast China and in the Arctic Ocean. In China the time scales are mostly within 1-4 years and reach 10 years in the Northeast.

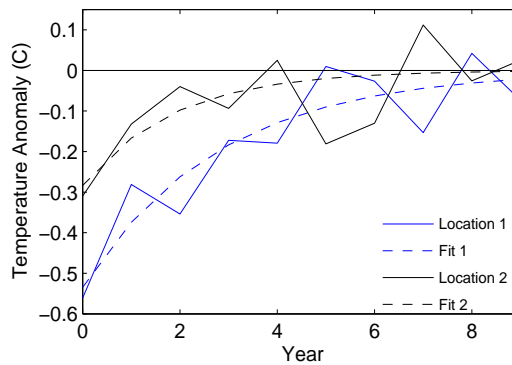


Fig. 4.4: Examples of exponential fits to averaged temperature anomalies. Location 1: $102^{\circ}\text{E}/22^{\circ}\text{N}$ (Northeast China, recovery time scale $\tau \approx 3$ yrs, $\Delta T_0 \approx -0.5^{\circ}\text{C}$), location 2: $116^{\circ}\text{E}/43^{\circ}\text{N}$ (Southwest China, $\tau \approx 2$ yrs, $\Delta T_0 \approx -0.3^{\circ}\text{C}$)

A remarkable coincidence of high amplitudes and large time scales appears in the Southern Pacific Ocean.

A possible physical mechanism for small amplitudes and short time scales on the ocean is rapid mixing in the ocean surface layer (for example in the North Atlantic where small amplitudes inhibit fits at some grid boxes). In regions with small amplitudes intense long term memory has been identified in preceding analyses of the global sea surface temperature (Fraedrich and Blender, 2003). On the continents the snow albedo feedback is a possible mechanism for long relaxation times; furthermore, soil wetness and permafrost may induce long memory. Since the snow cover on the Himalaya reveals short time scales (see Fig. 4.5a and b), the interpretation of long relaxation time scale as a snow albedo feedback is unclear.

4.4 East Asia: volcanic and ENSO effects

After the analysis of volcanic impacts on a global scale (Section 4.3), this section presents an analysis of the impacts and the co-operative effects of volcanic eruptions and ENSO events in simulations and reconstructions in East Asia.

4.4.1 Volcanic impacts without ENSO events

Volcanoes cool East Asian, especially the high altitude Himalayan region in West China with anomalies as low as -1°C in average (Fig. 4.6a for ensemble E1). Significant changes marked by 'x' are based on the Mann-Whitney test (95%). The mean in China is -0.54°C (-0.53°C in ensemble E2). During the year of the eruption the temperature anomaly reaches -0.54°C in E1 (E2: -0.38°C). The anomalies in both years are larger than twice the standard deviation.

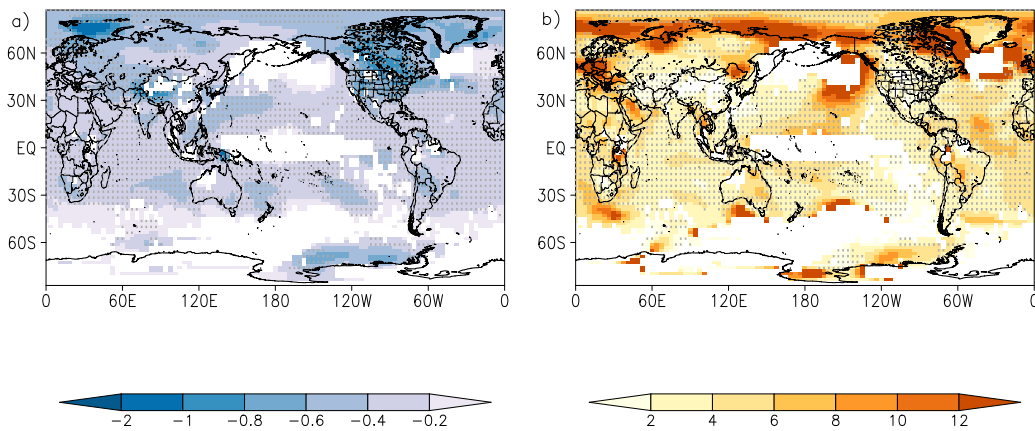


Fig. 4.5: (a) Temperature amplitude ΔT_0 [$^{\circ}\text{C}$] and (b) Relaxation time scale τ [years] of the temperature decay averaged after 31 volcanic eruptions in ensemble E1 without ENSO events (neutral, $|\text{PC1-SST}| < 1$) during the preceding two winters. Significant changes marked by 'x'.

Compared with the simulation result, the reconstructed temperature anomalies (Mann et al., 2009) show a similar cooling in most parts of China, however, with lower amplitudes (Fig. 4.7a, b and c). This can partly be explained by the smaller threshold for the intensity of volcanic eruptions used for reconstructions compared with simulations (compare Table 4.1, Table 4.3 and 4.4). Sporadic weak warming is found in Northwest China and central Asia for the volcanic eruption lists A15 and AN46 (Fig. 4.7a and b) and a significant warming for F12 (Fig. 4.7c), which is not simulated in the present experiments (4.6a).

Central China experiences anomalous wet summer (JJA) conditions (determined by the summer mean SPI) while a weak drought prevails in the South and the Northeast of China (Fig. 4.8a). The average summer rainfall anomaly in China during the year after the eruption is -56mm/month in E1 (-43mm/month in E2). In the eruption year (not shown) the anomaly is -47mm/month in E1 (-43mm/month in E2). Mao et al. (2009) report cool and dry periods after 11 volcanic eruptions. The rainfall deficit after the eruption year is 85%-significant in our analysis (a rainfall anomaly is also found by Anchukaitis et al. 2010; Peng et al. 2010).

The reconstructed drought index (Cook et al., 2010) shows drier conditions in most parts of China (significant in West China for list A10, in the North China Plain for AN46 and in Northeast China for F12, in Fig. 4.9a, b and c). In India, there is non-significant wetness except for list F12. Discrepancies occur in West China and central Asia with significant wetter conditions in simulations (compare Fig. 4.8a). While the wetness in India is also found in simulations the dryness in parts of Southeast Asia cannot be confirmed by reconstructions according to the three lists. Possible causes for the discrepancies are (i) that the direct influence of the reduction in shortwave radiation due to aerosol forcing on monsoon circulation (precipitation) is offset or overwhelmed by indirect or dynamical influences in reconstructions (sug-

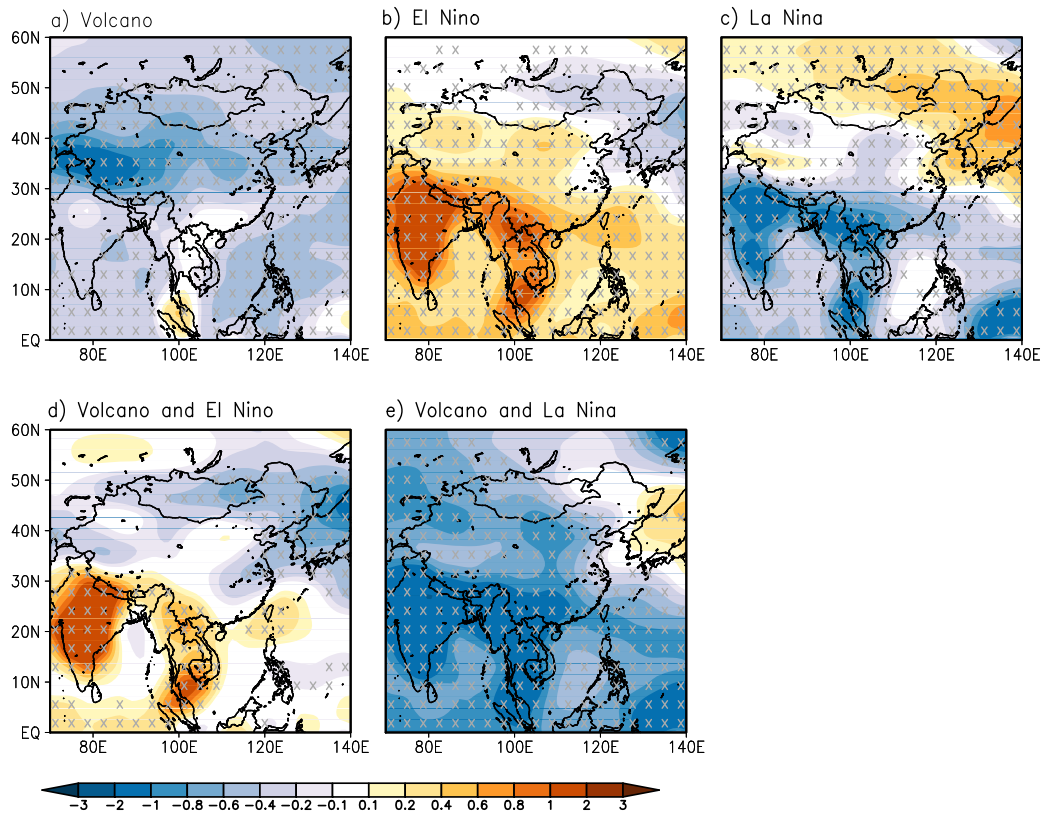


Fig. 4.6: Simulated annual mean temperature anomalies [$^{\circ}\text{C}$] in the ensemble E1 in East Asia in the year after: **(a)** volcanic eruptions with no ENSO events (neutral, $|\text{PC1-SST}| < 1$), **(b)** El Niño and **(c)** La Niña events without preceding eruption, **(d)** eruptions with El Niño events, **(e)** eruptions with La Niña events. Significant areas are marked by 'x'.

gested by Anchukaitis et al. (2010)) or (ii) the uncertainty of the parameterization of aerosol microphysics identified by Timmreck et al. (2010).

4.4.2 ENSO effects

In the analysis of the ENSO impact, years with a preceding volcanic eruption are excluded. The impacts of winter El Niño and La Niña events on temperature and precipitation anomalies in the subsequent year are almost anti-symmetric (determined in ensemble E1, Fig. 4.6b, c, Fig. 4.8b, c). This anti-symmetric image is consistent with Hagemann et al. (2006), supporting the view that interannual variations of precipitation at lower latitudes are largely driven by SST anomalies in the equatorial Pacific. El Niño warms the largest part of East Asia except for the North-east and temperature anomalies up to $\pm 1^{\circ}\text{C}$ are simulated (opposite for La Niña, Fig. 4.6c). The summer mean SPI for El Niño events shows a tripole pattern ori-

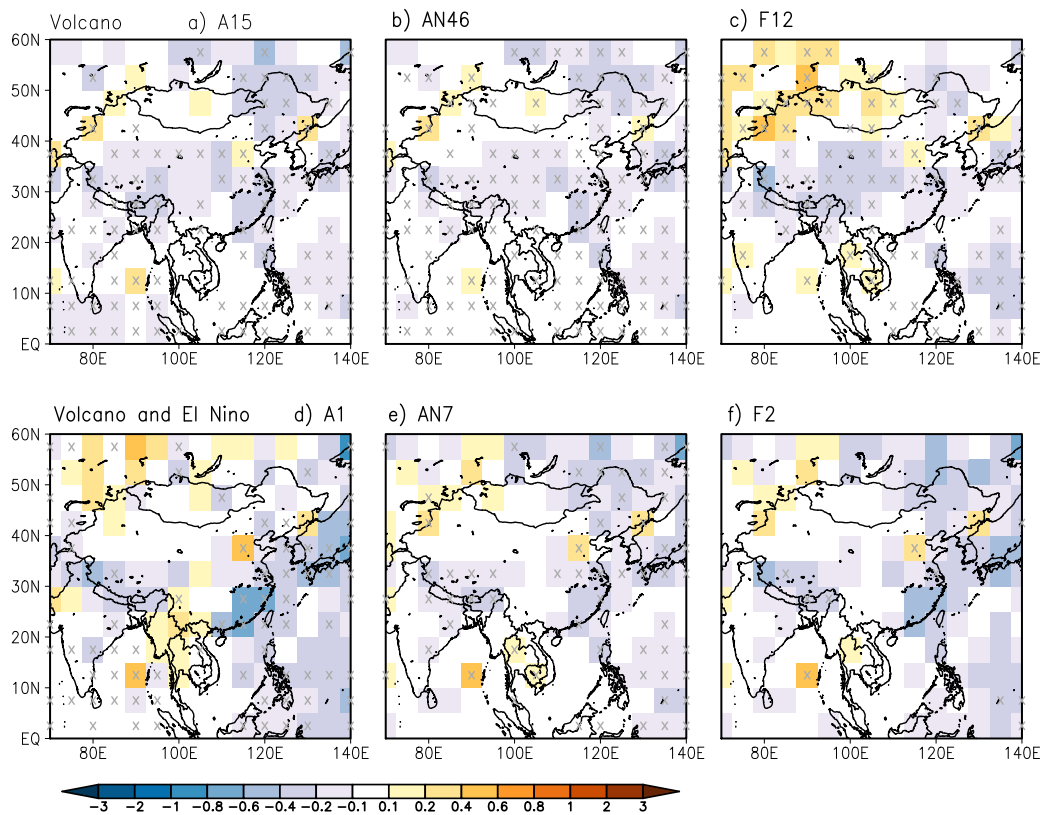


Fig. 4.7: Reconstructed temperature anomalies [°C] for volcanic eruptions without ENSO events according to list (a) A15 (Ammann et al., 2007), (b) AN46 (Ammann and Naveau, 2003) and (c) F12 (Fischer et al., 2007), and volcanic eruptions with El Niño events in the following winter according to list (d) A1 (Ammann et al., 2007), (e) AN7 (Ammann and Naveau, 2003) and (f) F2 (Fischer et al., 2007) (details of the list of eruptions see Table 4.3 and Table 4.4). Significant areas are marked by 'x'.

ented from Southwest to the Northeast (Fig. 4.8b, c): Whereas Southeast Asia experiences moderate summer wetness, India and Northeast China are drier (the La Niña impact is almost opposite). Clearly, the dominant impact is in the western tropical Pacific.

4.4.3 Volcanic response with ENSO events

To assess whether volcanic eruptions are linked to an increase of El Niño events, the numbers of concurrent events are analyzed: Among the 105 (E2: 63) volcanic eruptions, 23 in ensemble E1 (12 in E2), are accompanied by El Niño events in the following winter (with identical numbers of La Niña events). The sum of El Niño events in the whole simulated period amounts to 1249 in E1 (E2: 733) and La Niñas events to 1164 (704). A significant increase of El Niño events after volcanic

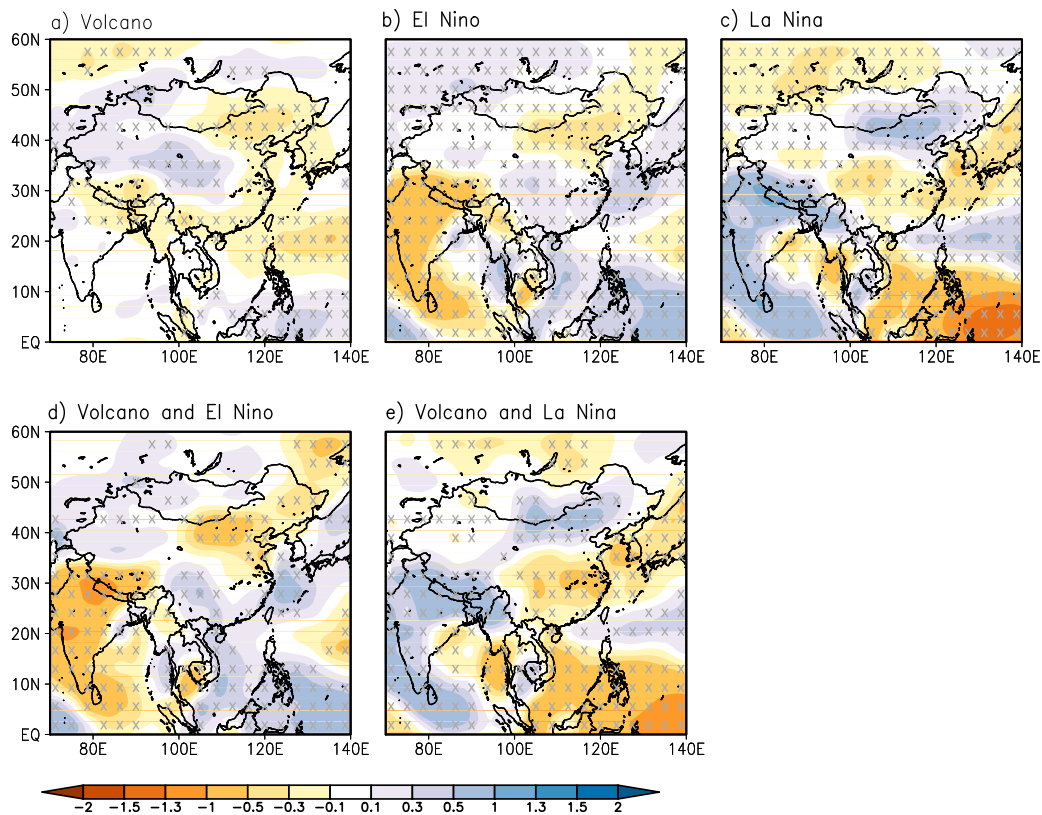


Fig. 4.8: As in Fig. 4.6 for summer (JJA) mean of the monthly Standardized Precipitation Index (SPI)

eruptions is not found in both ensembles; the p-values are 0.81 for El Niños in E1 (E2: 0.84), and 0.59 for La Niñas in E1 (E2: 0.94).

The temperature and SPI responses during the year after volcanic eruptions with a winter El Niño or La Niña event may reveal dramatic impacts. In China the cooling effect caused by volcanic eruptions (Fig. 4.6a) is almost compensated by the warming induced by El Niño events (Fig. 4.6d). The superposition of the La Niña and the volcano impact (Fig. 4.6e) yields enhanced cooling by the same order of magnitude. In the Northern Pacific the La Niña induced warming dominates. After the eruption with an accompanying El Niño event the temperature anomaly in ensemble E1 is -0.12°C (ensemble E2: -0.31°C) and for a La Niña event -0.73°C in E1 (E2: -0.68°C).

The compensation of the volcanic impacts by El Niño events is also found in reconstructions (Fig. 4.7d, e and f), resulting in rather weak anomalies in Northwest China. The Tibetan Plateau and the eastern parts of China remain cold. However, the simulated warming in South Asia (Fig. 4.6d) is not found in all lists A1, AN7, and F2.

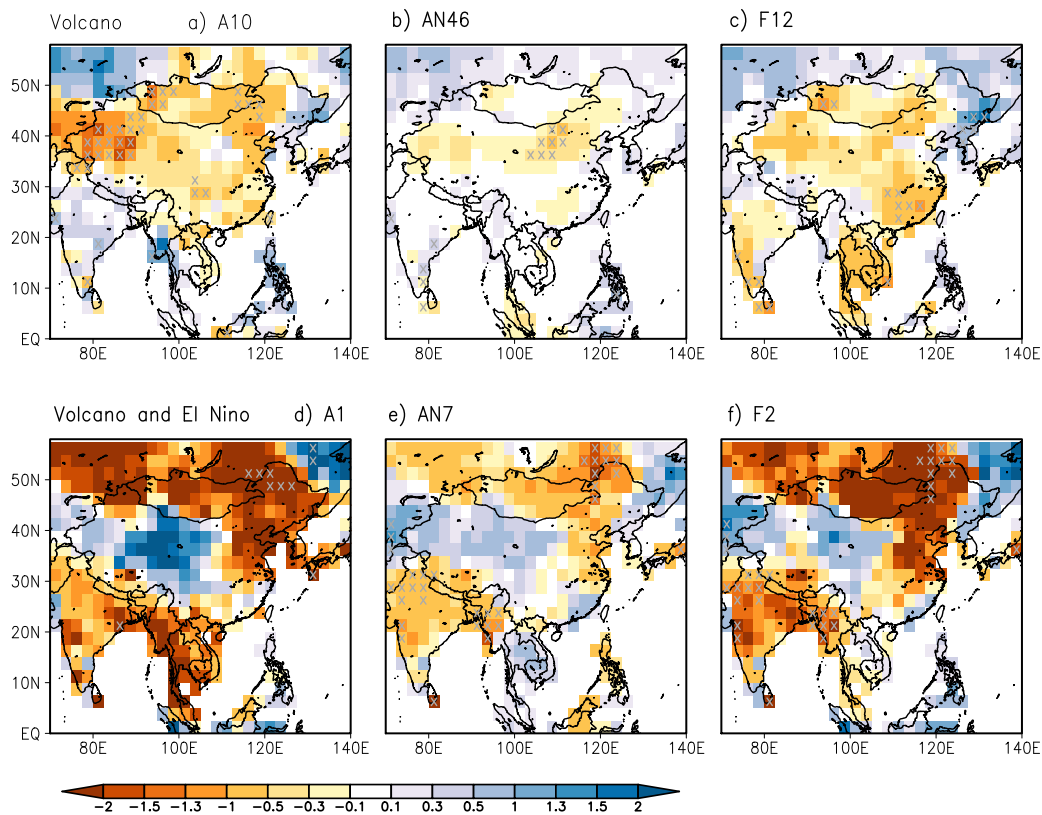


Fig. 4.9: As in Fig. 4.7 for summer (JJA) mean of the Palmer Drought Severity Index (PDSI). The list are for (a) A10 (Ammann et al., 2007), (b) AN46 (Ammann and Naveau, 2003) and (c) F12 (Fischer et al., 2007), and volcanic eruptions with El Niño events in the following winter according to list (d) A1 (Ammann et al., 2007), (e) AN7 (Ammann and Naveau, 2003) and (f) F2 (Fischer et al., 2007) (details of the list of eruptions see Table 4.3 and Table 4.4). Significant areas are marked by 'x'.

In the present simulations, the co-operative precipitation response of volcanoes and El Niños (Fig. 4.8d) reveals a quasi-linear superposition with a dominance of the El Niño pattern shaped as a tripole (Fig. 4.8b, Kirchner and Graf, 1995). In west and central China wetness caused by volcanic eruptions is unaltered by El Niños; in the North drought is even stronger in the combined case (Fig. 4.8d) than in the pure volcano or El Niño response. A similar superposition pertains to La Niña (Fig. 4.8e). Remarkable is that in West China (province Xinjiang), the volcano induced wetness is absent after La Niña events, although La Niñas do not cause dryness here. Thus, the major mutual interaction of volcanoes and ENSO anomalies can be understood as a linear superposition, with a few deviations, mainly in West China, which can possibly be interpreted as nonlinearities. The SPI (JJA) anomalies obtained in the second ensemble E2 (not shown) show similar results. The average summer rainfall anomaly in China in the year after an eruption and a subsequent El

Niño event in ensemble E1 is 64mm/month (E2: 68mm/month); for a subsequent La Niña event the anomaly is even positive with 29mm/month (E2: 29mm/month). Although there are suggestions that the GCMs may not completely capture the balance of important coupled ocean-atmosphere processes involved in the response of the Asian climate to radiative forcing (Anchukaitis et al., 2010), the reconstructions show similar tripole pattern in the simulations for all three lists (Fig. 4.9d, e and f): Drier conditions in Mongolia, Northeast China, and South Asia, and wetter conditions in central and Northeast China. Discrepancies between simulations and reconstructions occur in Northwest China and Mongolia. A noteworthy result is that compared to the volcanic effects with neutral ENSO events (Fig. 4.9a-c), the reconstruction reveals that the El Niño events after volcanic eruptions affect mainly central and Northeast China while the simulation indicates impacts in East China (Fig. 4.8a and b).

4.5 Tambora eruption in 1815

The eruption of the Tambora during April 1815 was the most intense eruption in historic times classified by the Volcanic Explosivity Index VEI=7 (on a scale from 0 to 8, see also Table 4.1). The Tambora eruption occurred during the Dalton minimum (1790-1830), an extreme cold period terminating the Little Ice Age and caused the 'year without summer' 1816. In the present simulations the Tambora eruption is the second most intense with a drop in solar radiation of -6.9 to -7.5 W/m² detected in the eight ensemble members.

4.5.1 Temperature and SPI

The Tambora eruption caused a long cold period in China. The temperature reduction (Fig. 4.10a) during the period 1780-1850 is clearly visible in the simulated annual mean temperature anomaly and in the reconstructions by Wang et al. (2007b) and Yang et al. (2002). The cooling started in 1809 (eruption of St. Helen) and reached an anomaly between -1.2 and -1.3°C in the two ensembles. The simulated anomalies reveal a recovery time scale of several years, which is distinctly longer than the mean calculated for 31 eruptions (Fig. 4.5b).

The simulated summer SPI in Southeast China (105° - 130°E , 25° - 30°N), as in the reconstruction by Zheng et al., (2006) is below the mean for more than two decades, 1795-1825, in both simulations, which add up to a climatological relevant humidity deficit at the end of the Dalton minimum (Fig. 4.10b). The reconstruction of an annual drought index by Central Meteorological Bureau (1981, CMB) averaged over Southeast China reveals high intra-annual variability and no relationship to the eruption in 1815. The decadal reconstructed dry/wet summer index from Zheng et al. (2006) which is based on historical documents and the annual drought index from Cook et al. (2010) reveal depressions during the Dalton Minimum which are neither reflected in the CMB index nor in the two ensemble simulations.

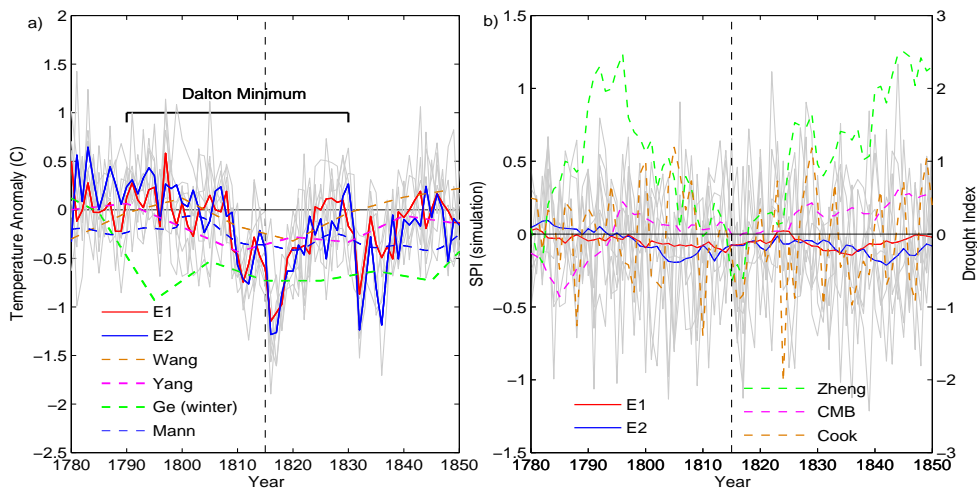


Fig. 4.10: (a) Temperature anomalies [$^{\circ}\text{C}$] in China in simulations and reconstructions for 1780-1850. The simulated (solid) curves are ensemble means for E1 and E2 (thin grey lines indicate all eight ensemble members), and the reconstructed (dashed) lines refer Yang et al. (2002), Ge et al. (2003), Wang et al. (2007b) and Mann et al. (2009); (b) Decadal mean simulated Standardized Precipitation Index (SPI, solid, as in (a), left axis) and reconstructed drought index in Southeast China (dashed, right axis, decadal means) from Zheng et al. (2006), Central Meteorological Bureau (CMB, 1981), and Cook et al. (2010). The Dalton minimum (1790-1830) and the Tambora eruption (1815) are marked

4.5.2 ENSO optimal realization

A closer look at the SPI time series in the eight ensemble members reveals that there is a possible likelihood for decreased precipitation after 1815. Its variability can be explained by ENSO (see Fig. 4.8b, c). Therefore, the eight PC1-SST time series in the period near the eruption (Fig. 4.11a) are compared to historic documents. Furthermore, extreme La Niña and El Niño as well as a neutral case are considered.

According to the reconstructed El Niño data (Quinn, 1993) there were no El Niño events in 1815 and 1816, but probably strong El Niño events in 1814 and 1817. In the respective time period, the reconstruction by McGregor et al. (2010) represents an El Niño in 1815/16 which deviates from Quinn (1993). The data of Mann et al. (2009) does not contradict Quinn (1993). For a comparison, four simulations with different ENSO states are selected out of the eight members in the ensembles E1 and E2: (i) a neutral ENSO ($|\text{PC1-SST}| < 1$) in 1813-1816 (simulation E1-3), (ii) a strong El Niño in 1816 (E1-4) which follows the reconstructed ENSO by McGregor et al. (2010), (iii) a strong La Niña in 1816 (E1-2), and (iv) an optimal realization which follows the historically reconstructed El Niño events by Quinn (1993) closely during 1814-1817 (E2-3, Fig. 4.11a). Note that although we favor the widely accepted reconstruction by Quinn (1993, referred to as 'Optimal'), we consider the data from McGregor et al. (2010) as well (E1-4, referred to as 'El Niño'). Due to the

absence of information about La Niña events, the reconstruction by Quinn (1993) does not exclude La Niña events to have occurred in 1815 and 1816.

These selected simulations reveal distinct patterns of temperature and precipitation anomalies in China during the decade 1810-1820 (Fig. 4.11b, c). A remarkable result is that the coldest simulated temperature anomalies for the optimal realization of the ENSO did not occur in 1816, but two years after the eruption, with a magnitude similar to the La Niña state. This persistence may explain long lasting impacts like the three years famine in the province Yunnan.

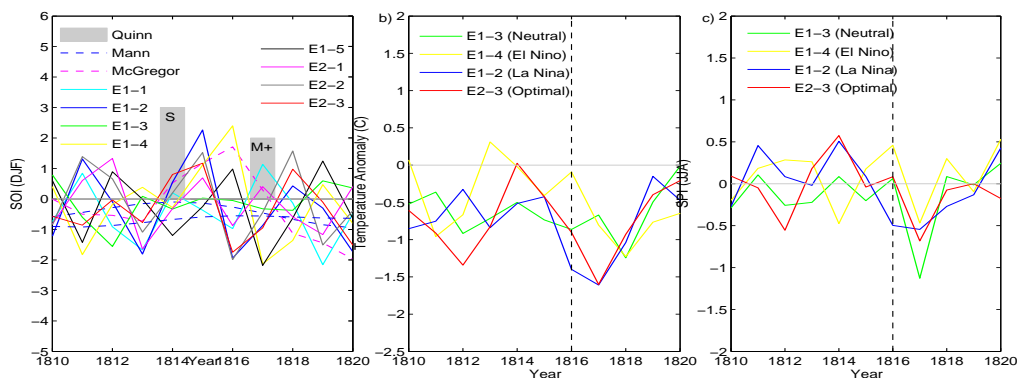


Fig. 4.11: ENSO (PC1-SST) and climate in China during the cold decade of 1810 to 1820 embedding the year without summer (1816): **(a)** PC1-SST in eight simulations of ensembles E1 and E2; grey shades indicate 'strong' (S) and 'moderate+' (M+) reconstructed El Niño events (see the definition by Quinn, 1993). Selected ENSO patterns: E1-3 (neutral, green, hidden by the red symbol), E1-4 (El Niño, yellow), E1-2 (La Niña, blue), E2-3 (optimal, red); **(b)** temperature anomalies in China and **(c)** SPI in Southeast China for selected ENSO patterns as in (a).

Spatial anomalies of temperature and precipitation corresponding to the four PC1-SST states reveal different response patterns in East Asia in 1816 (Fig. 4.12). (i) The neutral ENSO pattern shows a moderate cooling (compare with Fig. 4.6a) except in Tibet, Northeast, and Southeast China. The major impact is an extreme dryness in East China (compare Fig. 4.8a); there is agreement with reconstructions in Northeast China (Mao et al., 2009). (ii) The El Niño pattern (which is unlikely according to the reconstruction by Quinn (1993)) balances the volcanic cooling and the dryness effects in large parts of China (Fig. 4.6d and Fig. 4.8d). (iii) A La Niña state generates extreme coldness in East Asia and a moderate drought in the South and the Northeast (the strong volcano dominates the La Niña impact, compare Fig. 4.6 a and c); note that these regions are the most densely inhabited areas in China. (iv) The realization with the optimal ENSO pattern reveals a moderate cold anomaly in a large part of China (besides the South) and an extreme dryness in the Northeast.

Comparison of the simulation with historical documents excludes an El Niño event in the winter 1815/1816 for two reasons (in agreement with Quinn 1993): First, observations report coldness in most parts of China while the El Niño simu-

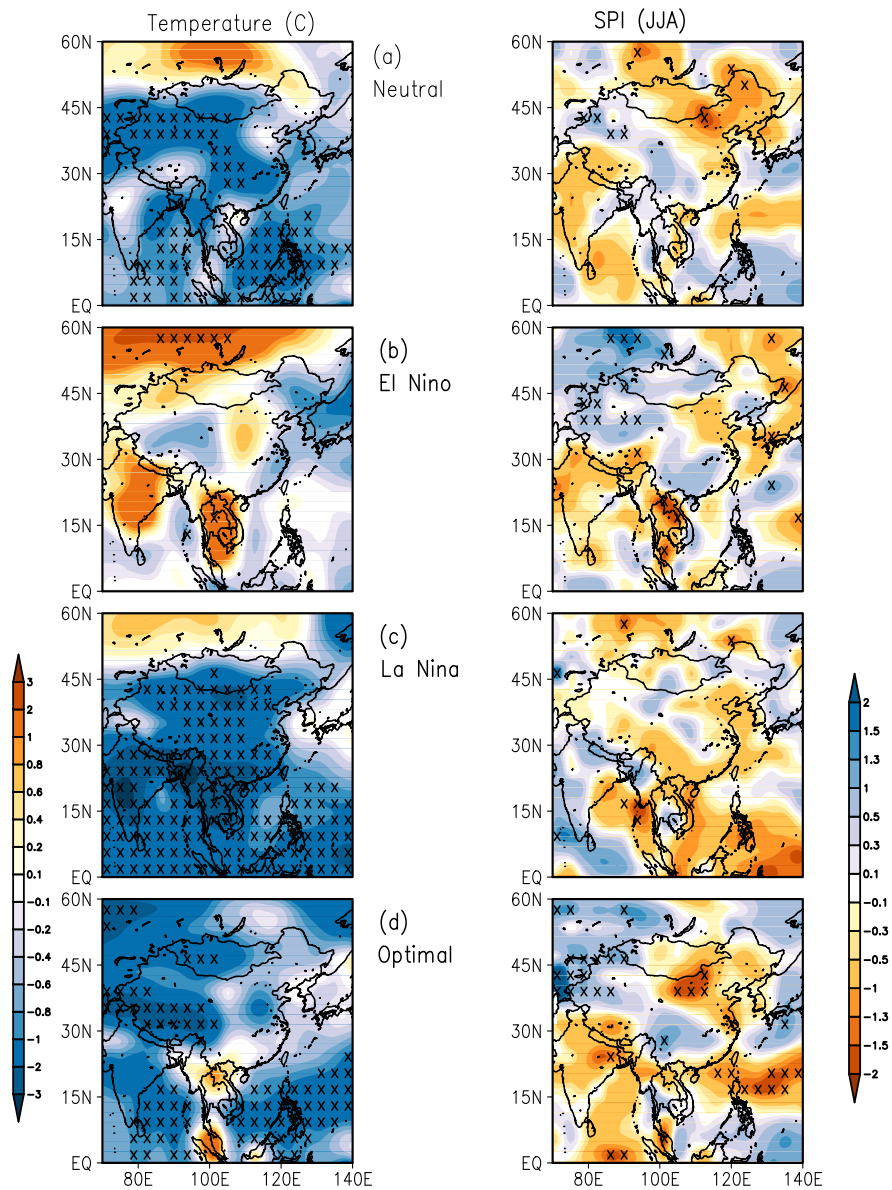


Fig. 4.12: Temperature anomalies in 1816 (annual mean [°C], left column) and SPI (JJA, right column) in four simulations with different ENSO patterns (see also Fig. 4.11): **(a)** Neutral ($|\text{PC1-SST}| < 1$), **(b)** El Niño, **(c)** La Niña, and **(d)** optimal realization (compare Quinn, 1993)

lation does not indicate a temperature anomaly. Secondly, the documents describe droughts in the East as it is simulated by all ENSO states besides El Niño. However, a caveat remains for the simulation with the optimal ENSO (which is close to reconstructions) since the simulated wetness and the absence of a temperature anomaly in Southeast China contradict historical documents reporting a dry and cold period.

A general conclusion is that temperature is dominated by the El Niño event, while precipitation remains dominated by the impact of the Tambora eruption.

4.6 Volcanic eruptions and Asian summer monsoon

In the present analysis, the Asian summer monsoon (ASM) is characterized by two indices: the Monsoon Hadley circulation index (MHI) presenting the south Asian summer monsoon and the East Asian Summer Monsoon Index (EAMI) presenting the east Asian summer monsoon (see Section 4.2 for a detailed method description).

Both indices are extracted from three years before to ten years after the events of: volcanic eruptions without ENSO events, El Niño/La Niña events without preceding eruptions, and eruptions with El Niño/La Niña events (Fig. 4.13). When there is volcanic eruptions (set as year zero), the ASM is weaker than average (non-significant) during the next three years (red curves in Fig. 4.13). After El Niño/La Niña events (set as year zero) without preceding eruptions, the ASM experiences a weak/strong year at year zero (significant for MHI, blue and green curves in Fig. 4.13). In the case of concurrence of eruptions and El Niños, both indices drop sharply at year zero indicating that the weakening of the ASM caused by volcanic eruptions is strengthened by El Niños; the negative anomalies remain significant until year one and reach the peaks one year later than only El Niño events (compare magenta and blue curves in Fig. 4.13). In the case of concurrence of eruptions and La Niñas, the weakening caused by volcanic eruptions is almost compensated by La Niña events at year zero; the peaks are also postponed by one year compared to only La Niña events (compare cyan and green curves in Fig. 4.13). Thus the volcanic eruptions without ENSO events can weaken the ASM (non-significant), El Niño events following the eruptions can cause a phase-locking of the ASM while La Niña events can enhance the ASM at year zero. In the two indices, the EAMI has a relatively stronger response compared to the MHI, which is also detected in their correlation coefficients with the summer precipitation in East Asia (Fig. 3.16).

4.7 Summary and conclusion

Due to the high population density China is extremely vulnerable to the climate impacts of volcanic eruptions, in particular if at the same time East Asia is influenced by ENSO events which may amplify (but also mitigate) the anomalies caused by eruptions. The present analysis uses ensemble simulations with a comprehensive state-of-the-art ESMs to (i) determine the impact of volcanic eruptions on temperature and summer precipitation anomalies (characterized by SPI), (ii) estimate the recovery time scale of temperature anomalies, and (iii) analyze the correlations and the co-operative effects of volcanoes and ENSO. A focus of this study is the Tambora eruption (1815) which had similar social impacts in China as the 'year without

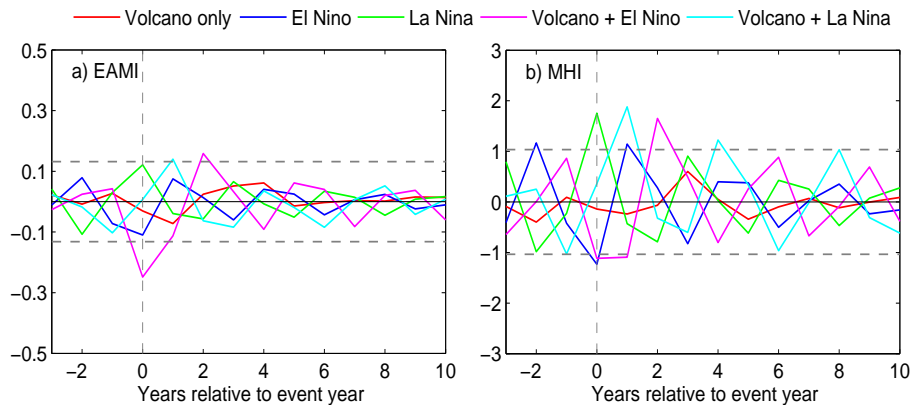


Fig. 4.13: (a) The East Asian Summer Monsoon Index (EAMI) and (b) the Monsoon Hadley circulation index (MHI) anomalies during the period from three years before to 10 years after the event year of: volcanic eruptions without winter ENSO events (neutral, $|\text{PC1-SST}| < 1$, red), El Niño (blue) and La Niña (green) events without preceding eruption, eruptions with El Niño events (magenta), and eruptions with La Niña events (cyan). Dashed lines are twice the standard deviations during the whole period 800-2005 AD.

summer' in Europe and North America. The ENSO state in different ensemble members is compared to historic information in 1814-1817 to select an optimal realization of the simulated climate.

For the present analysis the most intense 21 volcanic eruptions are selected to determine volcanic and ENSO impacts on the climate in China. ENSO is characterized by PC1-SST, defined by the principal component time series (PC1) of the first EOF of the tropical Pacific sea surface temperature (SST) variability in winter (DJF). The main results are:

Volcanoes without ENSO events

A global cooling is found as well as a non-significant El Niño-like warming in the tropical Pacific Ocean. The following winter is warmer in parts of Arctic Ocean, the tropical Pacific, the Bering Sea, and the Southern Pacific Ocean; in ensemble E2, this warming extends to Siberia and Central Asia. The recovery time scales of the cooling which describe the accumulated impact of the eruptions are determined locally by fitting an exponential function, $\Delta T(t) = \Delta T_0 * \exp(-t/\tau)$, with an amplitude ΔT_0 and a time scale τ . The recovery time varies between one and 12 years globally with the shortest times found on the oceans. In China the cooling decays mostly within the first four years, in the Northeast, however, 10 years are detected.

In East Asia, volcanoes cause a dramatic cooling in West China accompanied by drought in the eastern parts of China during the year after eruption. The mean temperature is reduced by -0.54°C in China and summer precipitation decreases by about -45mm/month . The reconstructions show similar cooling patterns with

smaller magnitudes and confirm the drought in East China.

ENSO without eruptions

After El Niño events warming is found in most parts of China apart from the Northeast. The summer precipitation decreases in the North, while South China becomes wetter. La Niña events cause opposite effects for temperature and precipitation.

Volcanic eruption and ENSO events

The simulated occurrence of El Niño events is not significantly increased after volcanic eruptions. As this result appears to be in disagreement with reconstructions (Adams et al., 2003), it may be model specific. El Niño events after eruptions yield moderate temperature anomalies in China in simulations (consistent with reconstructions), in particular the volcano-induced cooling in the West is almost compensated by El Niño and the precipitation deficit in the Southeast is inhibited. Both the simulated and reconstructed drought indices show tripole patterns which are altered by El Niño. La Niña events after eruptions, however, intensify the cooling (anomalies up to -3°C) and the drought in Southeast Asia. The combined signal of volcanoes and ENSO cannot be considered as a linear superposition of two distinct signals in East Asia. Note that, although the pattern of the precipitation response to ENSO is captured in ECHAM5 simulations (Hagemann et al., 2006), one of the model weaknesses is its regularity of 3-4 years (Blender et al., 2011), while observations indicate a variability of 2-7 years (Guilyardi et al., 2009). Furthermore, the present simulation reveals central Pacific ENSO anomalies.

Tambora eruption in 1815

Simulated temperature and SPI are compared with the reconstructed mean temperature in China (Yang et al., 2002; Ge et al., 2003; Wang et al., 2007b) and the drought indices in Southeast China (Central Meteorological Bureau, 1981; Zheng et al., 2006; Cook et al., 2010). The climate response to Tambora depends crucially on the ENSO state of the individual ensemble members. One of the simulations yields an ENSO pattern which can be associated with the historical El Niño reconstruction (Quinn, 1993, note that La Niña events are not included). This simulation caused a moderate temperature anomaly of -1.2°C , moderate wetness in south China and extreme drought in the North and the Northeast. Clearly, the results are constrained to a single optimal simulation; a large number of ensemble members in agreement with the optimal selection of ENSO would reduce the remaining internal noise and increase the credibility of the outcome.

Chapter 5

Climate change on the Tibetan Plateau and its effects on East Asia

5.1 Introduction

The Tibetan Plateau (TP) is the biggest and highest Plateau in the world. It has an average elevation exceeding 4500 metres above sea level and an area of 2.5 million km² covering most of the Tibet Autonomous Region and Qinghai Province in western China. It is also called 'The Third Pole' (Qiu, 2008). The plateau's pivotal role is due almost entirely to its height, which makes it peculiarly cold for its latitude – colder than anywhere else outside the polar regions (Qiu, 2008). The uplift of the TP leads to an elevated heat source, its extent presents a mechanical barrier (Hahn and Manabe, 1975; Bothe et al., 2011), and it has been known to have a profound influence on the formation of the Asian monsoon. The precipitation on the TP feeds the largest Asian rivers (Xu et al., 2008; Wang et al., 2008) and its climate variability has evident dynamic and thermodynamic effects on the general circulation and the climate in East Asia (Yao et al., 1996; Wang et al., 2007a, 2008; Yang et al., 2008; Bothe et al., 2011; Zhu et al., 2011).

The nature, timing, and spatial variability of climatic change over the TP for the last millennium has been constrained in plenty of researches: for example, ice cores and tree-ring sequences reveal marked temperature variability during the important climatic episodes, e.g. the Medieval Climate Anomaly (MCA), the Little

Ice Age (LIA) and the Modern Warming (MW) (Liu et al., 2005c; Holmes et al., 2007). Yang et al. (2002) suggest that the MCA occurred over the TP between about 1000-1300 AD, followed by the LIA (about 1350-1900 AD) and then the rapid 20th century warming. Ice-core accumulation and tree-ring records suggest that the frequency and intensity of droughts and/or reduced monsoon activity has been greater during the LIA (Wang et al., 2005; Davis et al., 2005; Shao et al., 2005). The observed data also show a rising trend with an average of 0.36° per decade over 90 stations in the TP during 1961-2007 (Wang et al., 2008). The simulated climate over the TP using the atmosphere-ocean General Circulation Model (GCM) ECHAM5 reveals a warming trend and a weakening monsoon precipitation on the TP as well as in eastern China during the last hundred years. The comparisons between simulations and proxy data reveal that the causes to the warming trend in the 20th century and the drying trend over the TP in the last two centuries are plausibly the anthropogenic land cover change (ALCC) and the increasing greenhouse gases (Zhang et al., 2010, see Chapter 2 and Chapter 3).

The biogeophysical effect of ALCC plays an important role, which involves the modification of the physical properties of the land surface; for example, the sharp changes in the surface albedo in the TP and in eastern China totally modify the climate in the last century. According to previous studies, these changes in surface albedo may even affect remote areas via teleconnections (Chase et al., 2000; Pongratz, 2009). Observations on the TP show that the local heating can intensify the East Asian monsoon by inducing the air pumping over the TP and producing cyclonic spiral zonal deviation circulation in the lower troposphere (Duan and Wu, 2005; Wu et al., 2007). The physical process by which an albedo-induced warming over the TP affects the precipitation in East Asia is illustrated by Wang et al. (2008) using ECHAM4. The teleconnections further confirm the influences of ALCC (in terms of surface albedo) on the climate in the TP and in eastern China. However, the balanced effects of ALCC are not fully understood (Pongratz, 2009) and are rather difficult to be explained simply by GCMs due to its large amount of components and interactions. The simpler models are becoming more attractive in this case. The diagnostic of the simulation is easier with fewer interactions occurring in the model. Meanwhile, the comparison between a model of intermediate complexity (Fraedrich et al., 2005) and GCMs would enhance the understanding of atmospheric phenomena and the identification of key mechanisms.

In the present chapter, the Planet Simulator, a model of intermediate complexity (Fraedrich et al., 2005) is used to analyze the effects of ALCC (in terms of surface albedo change) on the climate in the TP and its influences on the monsoon precipitation in eastern China. The analysis includes a control run and two sensitivity experiments with different surface albedo over the TP. For a comparison, the experiments are extended by two sensitivity experiments with identical settings but with lower atmospheric CO_2 concentration. The chapter is organized as follows: Section 2 describes the model and the experimental design, and gives a brief description of the climatology in the research area. The main results are analyzed and the dynamical mechanisms are discussed in Section 3. A short summary is concluded

in Section 4.

5.2 Model and experimental design

The present study uses the Planet Simulator (Fraedrich et al., 2005) at a T42 spectral resolution (approximately 2.8° on the corresponding Gaussian grid) with 10 non equally spaced sigma levels. The dynamical core is based on the Portable University Model of the Atmosphere (PUMA, Fraedrich et al., 1998). It can be freely downloaded from <http://www.mi.uni-hamburg.de/plasim>, where more comprehensive descriptions are available.

The experiments include a control and four sensitivity experiments. The control experiment is integrated for 10 years and the last 20 years are used to derive a reference state. It is forced by the annual cycle of monthly mean climatological values of sea surface temperature and sea ice distribution and by the prescribed atmospheric CO_2 concentration 360ppm. Both sensitivity experiments have 3 members in order to reduce the uncertainties arising from different initial conditions obtained from the control run. The only difference between the control and sensitivity experiments is a change in the land surface albedo over the TP region (27.5°N - 37.5°N , 75°E - 104°E , see Fig. 5.1): A 'Reduction' of the albedo by 50% is referred as experiment 'Red' while an 'Increase' of the albedo to 150% is referred as 'Inc'.

In order to analyze the effects of atmospheric CO_2 , the experiments are extended by two sensitivity experiments with less CO_2 concentration in the atmosphere, i.e. 280ppm, the remaining settings are identical. The corresponding names are, therefore, added with a 'C' ('Comparison', see Table 5.1).

Table 5.1: List of the experiments used in the present chapter carried out by the Planet Simulator. Experiment 'Red' refers to a 'Reduction' of 50% surface albedo in the TP, and 'Inc' refers to an 'Increase' of 50% of the surface albedo in the Tibetan Plateau, i.e. 150%. The atmospheric CO_2 concentration is prescribed at 360ppm level. For a 'Comparison', another two sensitivity experiments with identical settings but lower CO_2 concentration (280ppm) are performed and the corresponding experiment names are added by a 'C'.

Name	Surface albedo in the TP	Years	CO_2 (ppm)	Ensemble number
Control	100%	20	360	1
C	100%	20	280	1
Red	50%	20	360	3
Red-C	50%	20	280	3
Inc	150%	20	360	3
Inc-C	150%	20	280	3

Research regions

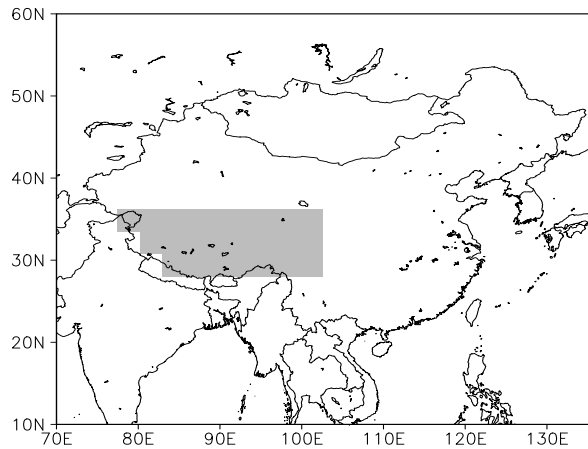


Fig. 5.1: Location of Tibetan Plateau in Planet Simulator in resolution T42 (approximately 27.5°N-37.5°N, 75°E-104°E) with altitudes higher than 3000m.

The Tibetan Plateau (TP) covers most of the Tibet Autonomous Region and the Qinghai Province in western China, as well as part of Ladakh in Jammu and Kashmir, India. It stretches approximately 1000 kilometres north to south and 2500 kilometres east to west. Its location in Planet Simulator is shown in Fig. 5.1. The region has less than 400 mm annual precipitation (mainly as hailstorms) in most parts of the TP except in the southeastern part and in high mountains, and less than 280 mm in large parts of the northern Plateau (Wang et al., 2007a). The winter temperatures can drop to -40°C . This dry climate results in desert formation in some areas of the Plateau, especially in the north. It is estimated that about 14% of the total area of the TP is occupied by land that has experienced desertification, and the region is suffering from the intensification of this process (Wang et al., 2007a). Fig. 5.2 shows the surface temperature and total precipitation in control runs in the Planet Simulator and ECHAM5. Generally speaking, the climatology in the Planet Simulator has similar patterns and amplitudes compared to ECHAM5. In the TP, the cooling and wetness patterns are consistent with ECHAM5, but the amplitudes are relatively larger. Note that the control run from the Planet Simulator has an atmospheric CO_2 concentration of 360ppm.

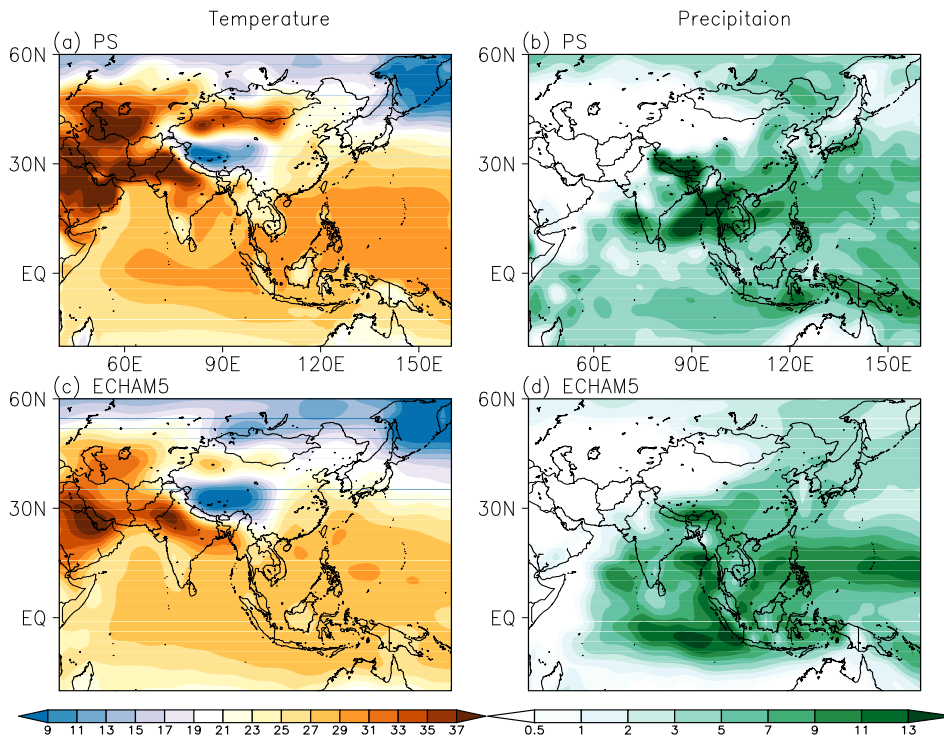


Fig. 5.2: Surface temperature [$^{\circ}\text{C}$] and total precipitation [mm/day] in summer in control run of model (a-b) Planet Simulator, (c-d) ECHAM5.

5.3 Climate change in the Tibetan Plateau and in eastern China

5.3.1 Surface albedo induced climate anomaly in the Tibetan Plateau and its influences in eastern China

In experiment 'Red' with the surface albedo reduced to 50% compared to the control run in the TP, there is a local warming up to 3°C in summer (ensemble mean shown in Fig. 5.3a); significant areas are marked by 'x' as p-values (representing 95% confidence level) of the Student's t-test. In this case, most parts of the TP are much wetter with amplitudes up to 2 mm/day compared to the control run (Fig. 5.3b). Sporadic cooling is detected in the North China Plain (NCP) and in Northwest China while drying conditions are simulated in Southeast China and in parts of NCP. When the surface albedo is increased to 150% of the control run, the ensemble mean surface temperature shows a symmetric pattern (Fig. 5.3c). The symmetric pattern of the summer precipitation is modified by the dry conditions in the western flank of the TP (Fig. 5.3d); in eastern China, the summer precipitation decreases with amplitudes up to 1 mm/day. Since the experiment 'Red' and 'Inc'

have similar spatial patterns but with opposite polarities, the ensemble means between them can be viewed as the impacts of surface albedo change. The warming and precipitation increase in the TP and in eastern China are quite outstanding (Fig. 5.3e and f). Therefore, we conclude that an increase in the surface albedo on the TP can induce an increase in the local precipitation (except the western flank) as well as an increase precipitation in eastern China.

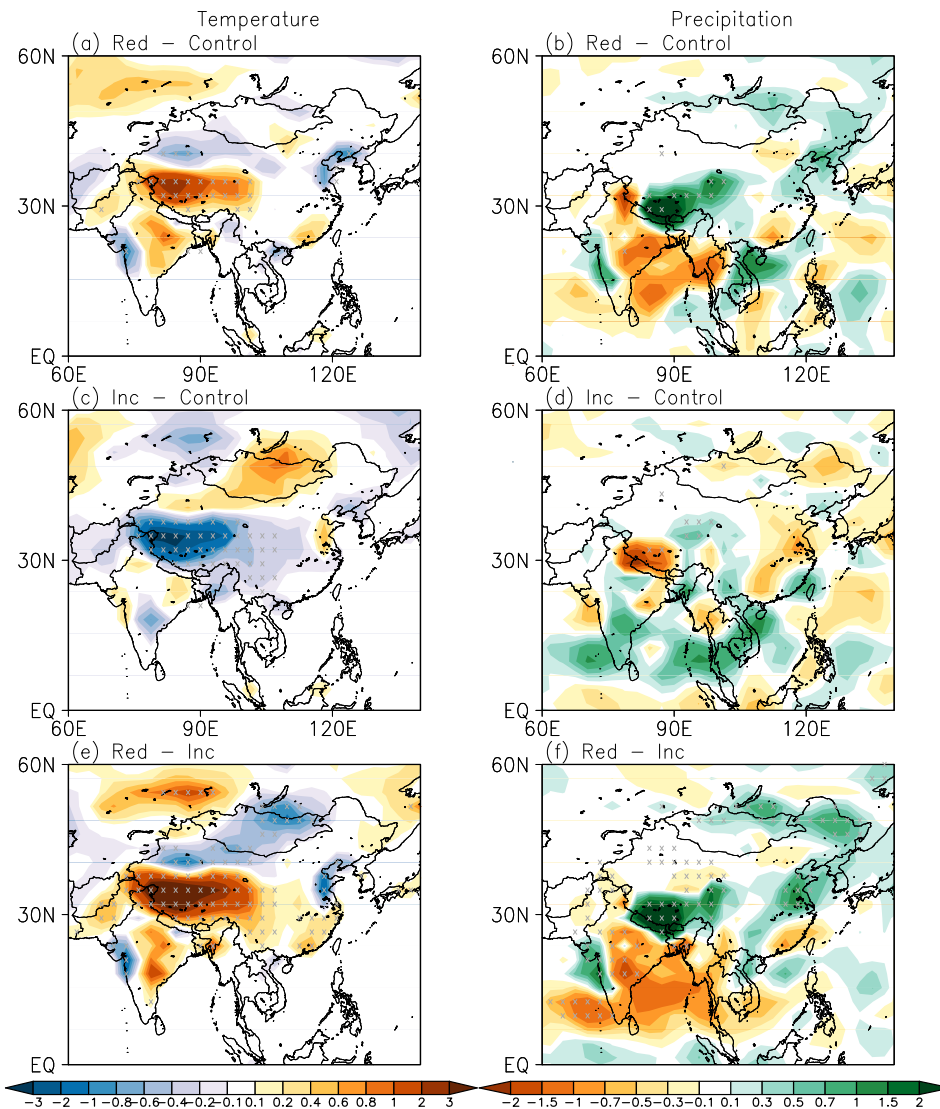


Fig. 5.3: The ensemble mean difference of surface temperature (left panel, °C) and total precipitation (right panel, mm/year) in summer between experiment (a-b) 'Red'-'Control', (c-d) 'Inc'-'Control' and (e-f) 'Red'-'Inc'. Experiment details see Table 5.1. Significant areas are marked by 'x'.

According to the observation by Wang et al. (2008) the rising temperature over

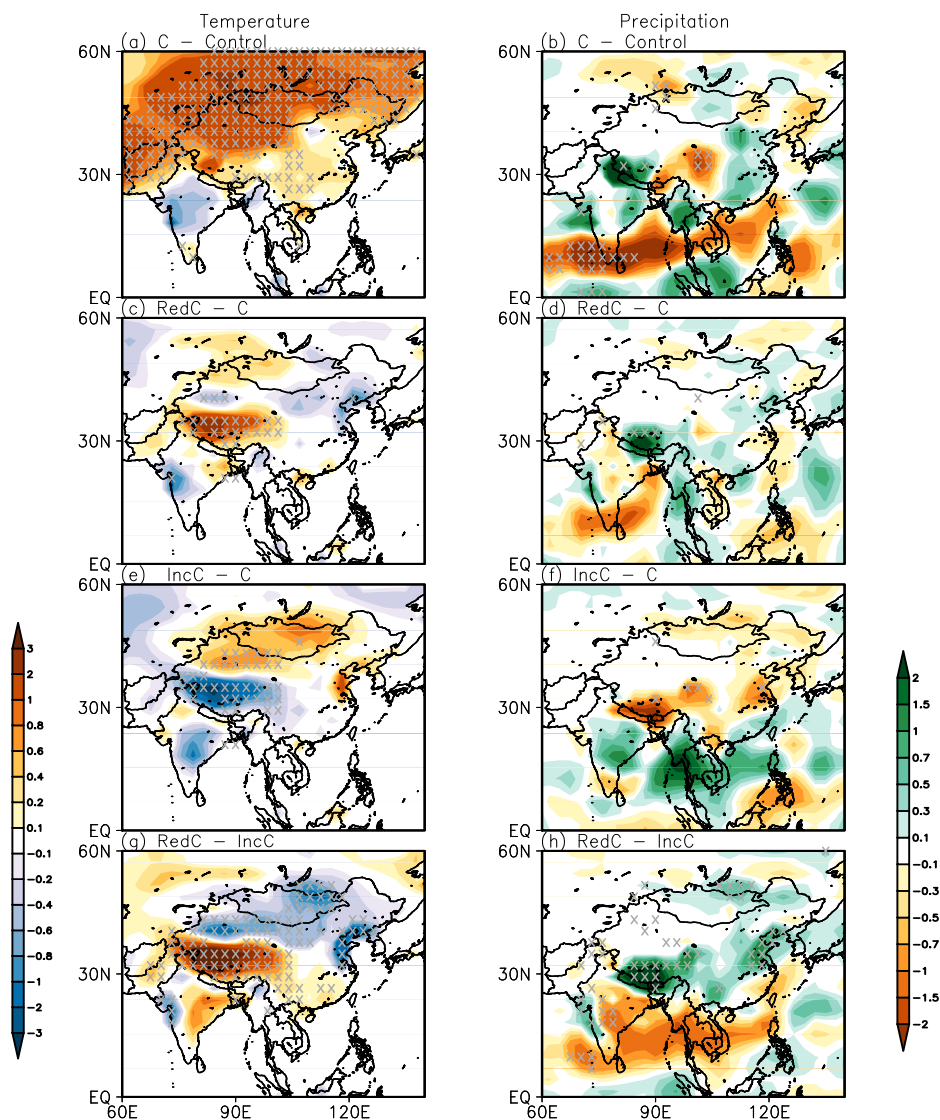


Fig. 5.4: The ensemble mean difference of surface temperature (left panel, °C) and total precipitation (right panel, mm/year) in summer between experiment (a-b) 'C'-'Control', (c-d) 'Red-C'-'C', (e-f) 'Inc-C'-'C', and (g-h) 'Red-C'-'Inc-C'. Experiment details see Table 5.1. Significant areas are marked by 'x'.

the TP in the past 50 years has a coherent pattern with the trend in the East Asia precipitation. Their model calculations using ECHAM4 suggest that the TP warming and East Asia summer precipitation are physically linked. In the present model (Planet Simulator), the ensemble mean difference between experiment 'Red' and 'Inc' can also be viewed as a 'TP warming' (Fig. 5.3e). The simulated warming has a similar pattern compared to the observed data with larger amplitudes up to

3°C (in Fig. 5.3e, in ECHAM4 by Wang et al. 2008 the amplitudes are up to 2°C). The simulated increase of the summer precipitation over the TP and in most parts of eastern China (Fig. 5.3f) bears also an overall similarity to the observed trend pattern and the model results by ECHAM4 (Wang et al., 2008). The drier condition in North China, however, is much smaller in the present simulation. Thus the Planet Simulator can capture the general patterns of the climate anomalies in East Asia induced by a surface albedo changes in the TP using ECHAM4.

The ALCC changes the climate in two aspects: the biogeophysical (including albedo, roughness, leaf area, and others) and biogeochemical effects (see Chapter 3). The results illustrate the positive effect of surface albedo changes on the precipitation in the TP and in eastern China. Meanwhile, the results using the full-forcings ensemble (ECHAM5, in Chapter 3) reveal that an increase in the surface albedo increase accompanies a summer precipitation decrease in the TP and in eastern China. Therefore, a conclusion is that in ECHAM5 the other biogeophysical effects of ALCC (other than surface albedo), or the biogeochemical effects of ALCC, or both are opposing to the effect of surface albedo. The balanced effects are negative on the summer precipitation in the TP and in eastern China as shown in Chapter 3. Furthermore, the dynamical link between the surface albedo changes over the TP and the summer monsoon precipitation in eastern China turns out to be another factor that can cause the precipitation changes in eastern China, although this factor may be opposing to the other causes discussed in Chapter 3.

The results in Chapter 3 using ECHAM5 also reveal that the rising fossil fuel emissions may be one factor that causes the summer precipitation deficits in China. In the present model (Planet Simulator) the difference of surface temperature and precipitation between the 'Control' run (CO₂ concentration at 360ppm level) and experiment 'C' (CO₂ concentration at 280ppm level) can be viewed as the influences of CO₂ concentration. When the CO₂ concentration in the atmosphere is higher, a warming is detected over the continents including most parts of China (with the maximum amplitudes in Northwest China) and central Asia (Fig. 5.4a, consistent with the results in Chapter 2). The summer precipitation responds with a complex tripole pattern. The TP is wetter in the western parts but drier in the eastern parts. Over most parts of eastern China, it is wetter except in Southeast China (Fig. 5.4b). Thus the Planet Simulator simulates a non-uniform response of precipitation in East Asia to the rising atmospheric CO₂ concentration. In the case of the surface albedo changes over the TP, the climate in the TP and in eastern China shows slight differences compared to the experiments with 360ppm CO₂ concentration (Fig. 5.4c-h). This reveals that the atmospheric CO₂ effect on the climate in East Asia is not linked to the effect of the surface albedo changes in East Asia. However, this result is restricted to the Planet Simulator and not applicable to the aerosols released by the land cover change, since the CO₂ is prescribed in Planet Simulator while it is interactively transported in the atmosphere and the ocean in ECHAM5.

5.3.2 Dynamical mechanisms

The model calculations suggest that the past changes in the TP temperatures and eastern China summer precipitation may be linked. The processes have been explained using ECHAM4 by Wang et al. (2008). In the present model, the process has similarities compared to ECHAM4: Over the TP, the surface warming caused by the reduction of the surface albedo (experiment 'Red') induces an upward transfer of sensible heat. It destabilizes the atmosphere and promotes convection, and results in more precipitation in the TP. Meanwhile, the latent heat released in the precipitation leads to ascent and shrinking of air columns above, strengthening the South Asian High in the upper troposphere (Rodwell and Hoskins, 1996; Wang et al., 2008, Fig. 5.5a). At the same time, the upper level westerly jet stream intensifies to the north of the TP while the easterly jet to the south. The diabatic heating in the TP region induces an anticyclone at upper levels and a cyclone at lower levels (Fig. 5.5), the mid-troposphere thus becomes warmer. When this thermal structure is far enough poleward to interact with the southern flank of the mid-latitude westerlies, this air moves down the isentropes on the western side of the TP (Rodwell and Hoskins, 1996; Wang et al., 2008) and moves up on the eastern side. Thus there is a upward motion over the TP accompanied by a notable descent to its northwest and an ascent to its northeast, forming a east-west symmetric pattern in vertical motion. This result is consistent with Wang et al. (2008) using the ECHAM5, although it differs from the classic conceptual model (see a discussion in Wang et al., 2008).

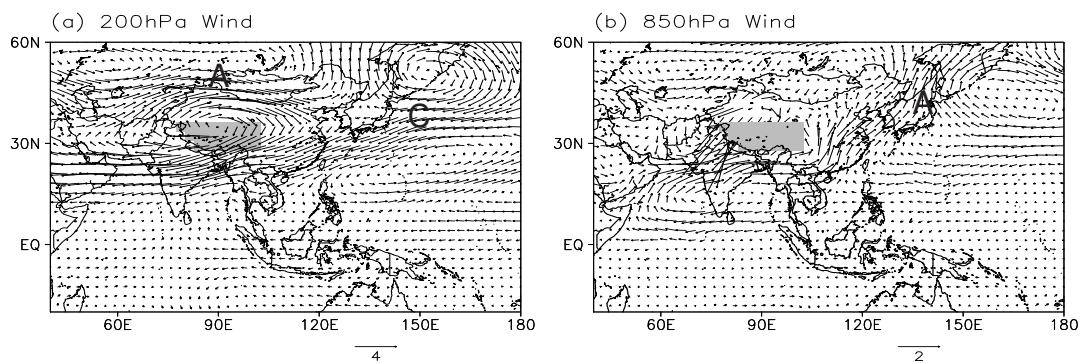


Fig. 5.5: The ensemble mean difference between experiment 'Red' and 'Inc' of (a) 200mb Wind [m/s] and (b) 850mb Wind [m/s] in summer. The letters 'A' and 'C' denote anticyclonic and cyclonic circulation center, respectively.

Therefore, the precipitation is increased due to the enhanced moisture flow over the east of the TP, which strengthens the East Asia subtropical front. In the subtropical Western North Pacific (WNP), the low-level anticyclone centered over Okinawa (Fig. 5.5b) is under the upper-level cyclone (Fig. 5.5a). The remote impacts of the TP warming on the climate in eastern China are explained by Wang et al.

(2008) through two distinct Rossby wave trains, one in the extratropics that moves along the upper-level westerly jetstream (Fig. 5.5a) and one in the tropics that moves westward along the low-level monsoon (Fig. 5.5b). Over the WNP, a nearly barotropic anticyclone is found to the east of Japan (Fig. 5.5a and b), which is a part of the vorticity wave train originating in the TP (Wang et al., 2008). The low-level anticyclonic ridge over the northern South China Sea is a part of the vorticity wave train along the South Asian monsoon westerly that is excited in the southwest periphery of the TP (Fig. 5.5b). The strengthened low-level anticyclonic circulation over the WNP reinforces the southwesterly along its northwestern flank, increasing water vapor transport toward East Asia subtropical front and the EA rain belt. These two wave trains are not as obvious as detected in the ECHAM4 by Wang et al. (2008), however, a similar response is captured by the Planet Simulator.

5.4 Summary and conclusion

Comparisons between simulations and reconstructions reveal that the anthropogenic land cover change (ALCC) is plausibly the cause for the warming/drying in the TP and eastern China in the last hundred years. Among all aspects of ALCC the surface albedo changes play the dominant role. In order to analyze the effects of the surface albedo on the climate in the TP and eastern China, numerical experiments are performed using a model of intermediate complexity, the Planet Simulator. The experiments include one control and two sensitivity experiments; the only difference between the control and sensitivity experiments is a change in the surface albedo over the TP: A 'Reduction' of 50% in experiment 'Red' and an 'Increase' to 150% in experiment 'Inc' compared to the control run. The results show a cooler/drier condition over the TP when the surface albedo is increased and a warmer/wetter (except western TP) condition when the surface albedo is decreased. The simulated warming reveals a similar pattern compared to the observed data and the model result using ECHAM4 (Wang et al., 2008). Similarly, there is a precipitation surplus in eastern China accompanied the TP warming, indicating that the surface albedo change and the summer precipitation in eastern China are physically linked.

The sensitivity experiments with the Planet Simulator reveal that the present model is able to capture the trends and patterns of the climate anomalies in eastern China due to the surface albedo changes over the TP. The result thus confirms the positive effects of surface albedo change on the TP on the summer precipitation in eastern China; furthermore, it confirms that the other biogeophysical effects of ALCC except the surface albedo, or the biogeochemical effects of ALCC, or both are opposing the effect of surface albedo change on the summer precipitation in eastern China.

The rising atmospheric CO₂ concentration induces a continental warming and a complex precipitation pattern in central and East Asia. However, its effects are independent from that of the surface albedo changes on the climate in East Asia. This conclusion is restricted to the present model which has prescribed CO₂.

The results with the Planet Simulator have similarities compared to the model results using ECHAM4 by Wang et al. (2008). In their analysis, the mechanism of the atmosphere response to the warming TP is illustrated by a schematic diagram (see Figure 4 in Wang et al., 2008). The westerly winds rising up the isentropes on the eastern side of the mid-tropospheric warm region give ascent over East Asia and South Korea, which results in enhanced precipitation there and enhances the Western North Pacific subtropical high centered at Okinawa through heating-induced Sverdrup balance. Meanwhile, two Rossby wave trains are excited due to the TP warming (Wang et al., 2008): one has a barotropic structure and propagates downstream along the upper-level westerly jet stream to enhance the anticyclonic circulation to east of Japan; another wave train developing along the low-level southwesterly monsoon propagates into the South China Sea and enhances the low-level anticyclonic ridge there. The two wave trains are well simulated in the Planet Simulator as in ECHAM4. They deform the Western North Pacific subtropical high in such a way that the low-level southwesterly monsoon strengthens moisture transport toward the East Asia subtropical front and reinforces the precipitation there (Wang et al., 2008).

Chapter 6

Summary and outlook

6.1 Summary and conclusion

This study investigates the climate variability in East Asia (EA) in the last 1200 years through model simulations and reconstructions. The millennium run is designed as two ensemble simulations using the COSMOS-Atmosphere-Surface (Land)-Ocean-Biogeochemistry (ASOB) Earth System Model (Jungclaus, 2009; Jungclaus et al., 2010). The model includes the atmospheric model ECHAM5 (Roeckner et al., 2003), the ocean model MPIOM (Marsland et al., 2003) and modules for land vegetation JSBACH (Raddatz et al., 2007) and ocean biogeochemistry HAMOCC (Wetzel et al., 2006), which are coupled via the OASIS3 coupler. The carbon cycle is interactively simulated. ECHAM5 is run at T31 resolution ($\approx 3.75^\circ$) with 19 vertical levels, and MPIOM at a horizontal grid spacing of about 3° with 40 unevenly spaced vertical levels. The model is forced by total solar irradiance (TSI), volcanic forcing (by aerosol optical depth and effective radius distribution), land cover change, and anthropogenic greenhouse gases and aerosols. The analysis includes a 3000-year control simulation, five single-forcing experiments, and two full-forcings ensembles: ensemble E1 with five members forced by a weak solar forcing and ensemble E2 with three members forced by a strong solar forcing.

The temperature variability obtained from ensembles E1 and E2 is compared with proxy data in China in terms of climate anomalies and spectrum analysis for the last 1200 years. Ensemble E1 and one reconstructed data set (from Wang et al., 2007b) are selected for regional analysis in terms of temperature anomalies and centennial spatial patterns (**Chapter 2**). The simulated hydrological conditions are compared with a variety of reconstructed drought indices in China. The possible

causes for the main trend in simulated precipitation, which is not detected in the reconstructions, are attributed to land cover change, greenhouse gases increasing and dynamical monsoon systems during the last hundred years. The variability of precipitation and runoff in the Yangtze Catchment (YC), its relationship with the snow cover in the Tibetan Plateau (TP), El Niño/Southern Oscillation (ENSO) and Asian summer monsoon in a model environment without variable external forcing (the control run) is also analyzed (**Chapter 3**). The climate variability in EA yields the dominant signal of volcanic eruptions in the last millennium, and due to its location in the largest monsoon system, EA is also vulnerable under the influence of ENSO events. ENSO may amplify (but also mitigate) the anomalies caused by eruptions. Therefore, we analyze the impact of volcanic eruptions on temperature and summer precipitation in EA, estimate the recovery time scales of temperature anomalies at a global scale, and analyze the co-operative effects of volcanoes and ENSO in simulations and reconstructions (**Chapter 4**). A focus of this chapter is the Tambora eruption which had similar social impacts in China as the 'year without summer' in Europe and North America. As the highest and biggest Plateau in the world, the TP is of importance to the atmospheric circulation and climate in EA. The climate change due to anthropogenic land cover change (ALCC) in terms of surface albedo changes over the TP is simulated using a model of intermediate complexity, the Planet Simulator. A control run and two sensitivity experiments are performed at T42 resolution. The influences of the climate changes in the TP on the summer monsoon precipitation in eastern China as well as the dynamical mechanism are analyzed (**Chapter 5**).

To conclude this study, I pursue the questions (Q1-10) raised in the introduction and summarize the main findings in the following:

(Q1-Q2) The temperature variability in simulations and reconstructions in China

Q1: Are the Medieval Climate Anomaly (MCA)/Little Ice Age (LIA)/Modern Warming (MW) consistent in the simulated and reconstructed data? Which ensemble does the mutual assessment favor?

Q2: Are these climatic episodes spatially uniform? Are they consistent with reconstructed temperature in different regions?

The near surface temperature data in two ensemble simulations (E1 and E2) are compared to three reconstructed temperature data sets in China. A mutual comparison indicates that the reconstruction from Wang et al. (2007b) is reconcilable with ensemble E1 forced by the weak solar forcing by Krivova et al. (2007). The long term anomalies of other reconstructions are beyond the uncertainty given by the simulations. The low frequency variability of the simulated mean temperature in China reveals a power-law scaling in the power-spectrum, $S(f) \sim f^{-\beta}$ with $\beta \approx 0.5$, indicating stationary long term memory (obtained for both ensembles E1 and E2). This agrees with the variability of the reconstructed mean temperature in China

by Wang et al. (2007b), whereas other reconstructions reveal nonstationary power spectra with $\beta \approx 2$.

The temperature in ensemble E1 is further compared to regional reconstructed temperature with decadal and centennial temporal resolution (Wang et al., 2007b) in Northeast (NE), Southeast (SE) and West (W) China. The regional temperature anomalies show high inter-annual variability on decadal time scales with volcanic eruptions as the dominant signature. The uncertainty of the simulated mean temperature is of the order of $\pm 0.5^\circ\text{C}$. Deviations from the reconstructions are: During the 11th century the model shows a moderate warming in China, whereas reconstructions indicate a zonal temperature contrast with a cooler western and a warmer eastern part. A further discrepancy is found in the 13th century when simulations are too cool in NE and W China (in SE China the simulations agree with reconstructions). During the LIA the simulated temperature anomaly agrees with reconstructions in the West and the Northeast. The annual cycle during the MCA was stronger on land but weaker on the East Pacific compared to the last two centuries. There is a strong land-sea contrast of the annual cycle change sign in the last two hundred years.

What must be beared in mind is that the results don't suggest that the simulated temperature in ensemble E1 and the reconstructed temperature by Wang et al. (2007b) are the 'true-history', but that they compare well with each other in all the simulated and reconstructed data discussed in the present chapter. The uncertainties assessed by the ensemble spread from the model allows the matching with the reconstructed data by Wang et al. (2007b) but not with the others. Different solar forcings used to force the two ensembles don't show significant differences in comparison with proxy data, however, this conclusion is restricted to EA/China. The other regions are beyond the scope of this study. In the view of the uncertainties from the proxy data, the proxy evidence is usually fragmentary, describes local conditions and the proxy indicators are influenced not only by environmental conditions but also by other non-climatic factors (Zorita, 2012). More proxy data would certainly decrease the uncertainties in 'optimal' selection and thus may alter the result.

(Q3-Q4) The variability of precipitation in East Asia and the precipitation and runoff in Yangtze catchment

Q3: In control simulation, what are the variabilities of runoff and precipitation in the Yangtze catchment? What are the relationships with ENSO, the Asian summer monsoon system as well as the snow cover on the TP?

Q4: What were the humidity conditions in China in the last 1200 years in the two full-forcings ensembles? Do different solar forcings show different trends and variabilities? Are they reconcilable with or are they captured in the reconstructed drought indices? What causes are responsible for the main trend in the simulated precipitation?

In the control simulation, the YC runoff, soil wetness in the TP, and the temperature in YC show memory up to decades, while precipitation reveals no memory. For longer time scales runoff, soil wetness, and temperature show weak long term memory similar to snow depth and snow melt on the TP. The variability of the monsoon is controlled by the ENSO mode. The ENSO cycle is detectable in the TP snow depth and snow melt, but not in the YC hydrology. The relationships between the YC runoff, the catchment hydrology, TP snow cover, Asian summer monsoon, and ENSO are analyzed. On an annual basis there are significant correlations between YC temperature and Indian summer monsoon, and between TP snow depth and ENSO. Noteworthy are the high correlation coefficients between decadal means of TP snow melt and Indian summer monsoon, and between YC temperature and ENSO. Temperature is anticorrelated with precipitation and soil wetness in the YC for annual and decadal means. The ENSO mode with the 3-4 year cycle exerts a dominating influence on the East Asian climate.

The simulated drought index obtained from two full-forcings ensembles E1 and E2 is compared with a variety of reconstructed drought indices in EA. In the simulations, from year 800 to 1800 AD, wet conditions dominate China, only in central and west China a precipitation deficit is found. From year 1200 to 1800, the wet conditions prevail in eastern China (in northeast after 1600). In the last 200 years, the model shows a severe precipitation deficit in most parts of China whereas the NW China becomes dry. The reconstructed drought indices reveal poor consistency between each other and the mutual assessment with two ensemble simulations yields no matching pair. The reconstructed drought index by Zheng et al. (2006) reveals high intra-annual variability, the dry periods are found in 11th-13th centuries and 15th century in east China, which is not confirmed by other reconstructions. The drought index from (Central Meteorological Bureau, 1981, hereafter CMB) shows small variability during the whole period. In the last two centuries, the summer in China has wet conditions with a decrease in the last 50 years (Zheng et al., 2006). However, the comparison between simulations and reconstructions indicates that the most distinguishing simulated feature, the precipitation deficits in the last hundred years, is not detected in neither of the reconstructed data, although a sharp decrease in the last 30 years is found in the drought index from Cook et al. (2010).

The comparison between simulated and reconstructed drought indices is further analyzed in terms of regional precipitation anomaly in four regions: Northeast (NE), Southeast (SE), Northwest (NW) and Southwest (SW) China. Precipitation is associated with interannual variability with some reminiscence of major volcanic eruptions in China (1258 and 1815). The MCA is not related to below average precipitation. However, a persistent period with relatively low precipitation with small uncertainties assessed by the ensemble spread is observed during the LIA. A distinct decrease in precipitation is simulated in the last century. The four regions show similarities in the distinct decrease with different starting years. The warming during this period supports the warm-dry climate mode. However, this relationship is not found during the cold period 1200-1300 (except in SE). The regional variability of precipitation shows the familiar maritime/continental contrast with lowest values

in the West and highest values in the Southeast. Comparisons with reconstructed drought indices reveal the following results: before 1500 AD, the dry periods in 11th-13th centuries by Zheng et al. (2006) occur only in NE China; in SE China there is no dryness. On the contrary, the summer experiences wet conditions in 13th century. The dry period in 15th century detected by Zheng et al. (2006) is confirmed by Cook et al. (2010) in NW and SW. The index by Cook et al. (2010) in NE China has the highest variability among all the four regions. From 1500 to 1800, drier summer in NW is detected by CMB (1981 and Cook et al. (2010) with a higher variability. In SW, the precipitation has a small variability in both reconstructed data. In the last 20 years, Cook et al. (2010) find an increase in precipitation in NW and a decrease in NE and SE China. In general, the reconstructions are far beyond the uncertainties given by the simulations, which is further confirmed by the power spectrum analysis. The simulated total summer precipitation shows a flat spectrum, hence there is no long-term memory present in the precipitation. The single deflection is an increase in power within the frequency range corresponding to 3-4 years, similar to the surface temperature. The reconstructed precipitation time series for East China (Zheng et al., 2006) shows periods $T \approx 2, 3, 4,$ and 7 years on a continuous background. The reconstructed precipitation from CMB (1981) and Cook et al. (2010) reveal similar power spectra with $\beta = 0.5$ and $\beta = 0.4$.

The causes for the precipitation deficits in eastern China and in the TP are analyzed using the single-forcing experiments. The results reveal that the most plausible causes are the ALCC and the rising greenhouse gases. The effects of ALCC can be explained in two ways: the biogeophysical and the biogeochemical effects. The first refers to the modification of the physical properties of the land surface. The increasing surface albedo and the other biogeophysical effects of land cover change other than albedo changes compensate each other and lead to a local warming and drying (see more discussions in Chase et al. 2000; Pongratz 2009). The biogeochemical effect of ALCC has the most important influence from the carbon cycle. The rising atmospheric CO_2 modifies the Earth's energy balance and thus the climate. Both effects of ALCC attribute to the precipitation deficits in NE, SE and SW China (the biogeochemical mechanism only in NW China). Besides ALCC, the fossil fuel CO_2 emission is another cause in all four regions China. The CO_2 concentrations, CH_4 and N_2O in the atmosphere increase at a very high speed in the present simulations and thus amplify the rainfall deficits caused by ALCC in the last several decades. Furthermore, the Asian summer monsoon system is weakening in the last two hundred years: the south and east Asian summer monsoon indices (characterized by the Monsoon Hadley circulation index (MHI) and the East Asian Summer Monsoon Index (EAMI)) obtained from ensembles E1 and E2 show significant decreasing trend in the last 200 years. The Asian summer monsoon system has a positive influence on the summer precipitation in NE and SW China and a negative influence in SE China.

The uncertainties of the causes remain: First, the uncertainties from the internal part of the biogeophysical effects of ALCC (for example, the opposing effects from surface albedo and from the evaporation), the uncertainties from the com-

bined effects of biogeophysical effects and biogeochemical effects. Thus the total influence of ALCC is still unknown whether they impose a net cooling or warming effect; the same reasoning pertains to precipitation which is even less understood. Second, the greenhouse gases can cool or warm the atmosphere depending on their properties; they can affect the clouds formation, change the cloud properties and thus the initiation of precipitation. Those can suppress precipitation, however, they can also increase precipitation. Furthermore, the complexity of precipitation in China is added due to its location in the Asian summer monsoon system. All the uncertainties compromise the difficulties in quantifying and locating the causes for the deficits. Future work may focus on the problems about the understanding in model differences, the interaction of biogeophysical and biogeochemical effects, the coupling of the carbon cycle, and the remote connections between the Asian summer monsoon system and ALCC. Since that there is no irrigated agriculture in the model and instead it is parameterized as wheat/maize, sensitivity experiments with different parameterizations is also an interesting topic for forthcoming studies.

The analysis in Q1-Q4 focus on the long term variability and may provide applications for climate comparisons with reconstruction based on proxy and documentary data. The high significance allows extracting relationships which can be masked by trends and long term variability in shorter data sets. The dynamically consistent relationships enable validation of climate reconstructions based on statistical approaches applied to proxy data. For a further analysis of the processes in EA a higher resolution atmospheric model version is preferable with a more detailed representation of the complex orography.

(Q5-Q8) Volcanic and ENSO effects: Global and East Asia

Q5: What are the volcanic impacts at a global and regional scale? How does the recovery of the temperature decay proceed and what time scales do they have? Is there winter warming and are they comparable with observations?

Q6: Do volcanoes cool/dry East Asia? Are they uniform in East Asia and are they consistent with reconstructed data?

Q7: Do eruptions increase the probability of El Niño events? When there are ENSO events in the following winter, how does the climate in East Asia respond compared to eruptions without ENSO events? Are the results consistent with proxy data?

Q8: What was the climate in East Asia after Tambora eruption? What was the ENSO state in history? Would the climate be different in East Asia if the ENSO state were different?

For the present analysis the most intense 21 volcanic eruptions in each member of ensemble E1 and E2 are selected to determine volcanic and ENSO impacts on the climate. ENSO is characterized by PC1-SST, defined by the principal component time series (PC1) of the first EOF of the tropical Pacific sea surface temperature (SST) variability in winter (DJF).

In the year after volcanic eruptions without ENSO events: A global cooling is detected and sporadic weak positive temperature anomalies are found in the Bering Sea, parts of the Antarctic Ocean as well as a non-significant El Niño-like warming in the tropical Pacific Ocean. The response pattern of Standardized Precipitation Index (SPI) is more complex than surface temperature. Drier conditions are simulated in central Asia, eastern parts of China, Australia and North Africa. The winter warming detected in observations in the following winter is simulated in parts of Arctic Ocean, the tropical Pacific, the Bering Sea, and the Southern Pacific Ocean; in ensemble E2, this warming has similarities in amplitudes and regions with only minor non-significant extensions to Siberia and Central Asia.

The recovery time scales of the cooling which describe the accumulated impact of the eruptions are determined locally by fitting an exponential function from year one to year ten, $\Delta T_{(t)} = \Delta T_0 * \exp(-t/\tau)$, with an amplitude ΔT_0 and a time scale τ . The fits require a negative amplitude and a sufficient temperature decay. The recovery time varies between one and 12 years globally with the shortest times found on the oceans. In China the cooling decays mostly within the first four years, in the Northeast, however, 10 years are detected.

In EA, simulated climate are compared with reconstructed temperature (Mann et al., 2009) and reconstructed summer drought index defined by the PDSI (Cook et al., 2010). The list used for volcanic eruptions without El Niño events are selected based on Ammann et al. (2007), Ammann and Naveau (2003), Fischer et al. (2007) and Gergis and Fowler (2006). The results show: Volcanoes cause a dramatic cooling in West China accompanied by drought in the eastern parts of China during the year after eruption. The mean temperature is reduced by -0.54°C in China and summer precipitation decreases by about -45mm/month . The reconstructions show similar cooling patterns with smaller magnitudes and confirm the drought in East China. This can partly be due to the lower threshold for the intensity of volcanic eruptions used for reconstructions compared to simulations. Central China experiences anomalous wet summer (JJA) conditions while a weak drought prevails in the South and the Northeast of China. The reconstructed drought index shows drier conditions in most parts of China. Discrepancies occur in West China and central Asia with significant wetter conditions in simulations. Possible causes for the discrepancies are (i) that the direct influence of the reduction in shortwave radiation due to aerosol forcing on monsoon circulation (precipitation) is offset or overwhelmed by indirect or dynamical influences in reconstructions (suggested by Anchukaitis et al. (2010)) or (ii) the uncertainty of the parameterization of aerosol microphysics identified by Timmreck et al. (2010). The cooling and drier condition is also reported by Mao et al. (2009), Anchukaitis et al. (2010) and Peng et al. (2010) but with different amplitudes and significant level.

The simulated occurrence of El Niño events is not significantly increased after volcanic eruptions. Among the 105 volcanic eruptions, 23 (E2:12) in ensemble E1 (E2: 63) are accompanied by El Niño events in the following winter (with identical numbers of La Niña events). A significant increase of El Niño events after volcanic

eruptions is not found in both ensembles. As this result appears to be in disagreement with reconstructions (Adams et al., 2003), it may be model specific.

El Niño events after eruptions yield moderate temperature anomalies in China in simulations (consistent with reconstructions), in particular the volcano induced cooling in the West is almost compensated by El Niño and the precipitation deficit in the Southeast is inhibited. Both the simulated and reconstructed drought indices show tripole patterns which are altered by El Niño. La Niña events after eruptions, however, intensify the cooling (anomalies up to 3°C) and the drought in Southeast Asia. The combined signal of volcanoes and ENSO cannot be considered as a linear superposition of two distinct signals in EA. Note that, although the pattern of the precipitation response to ENSO is captured in ECHAM5 simulations Hagemann et al. (2006), one of the model weaknesses is its regularity of 3-4 years (Blender et al., 2011), while observations indicate a variability of 2-7 years (Guilyardi et al., 2009). Furthermore, the present simulation reveals central Pacific ENSO anomalies.

Tambora eruption in 1815 caused a three-year famine in Yunnan province in China. The simulated temperature and SPI are compared with the reconstructed mean temperature in China (Yang et al., 2002; Ge et al., 2003; Wang et al., 2007b) and the drought indices in Southeast China (CMB, 1981; Zheng et al., 2006; Cook et al., 2010). The climate response to Tambora depends crucially on the ENSO state of the individual ensemble members. One of the simulations yields an ENSO pattern which can be associated with the historical El Niño reconstruction (Quinn, 1993) (note that La Niña events are not included). This simulation causes a moderate temperature anomaly of -1.2°C , moderate wetness in South China and extreme drought in the North and the Northeast. Clearly, the results are constrained to a single optimal simulation; a large number of ensemble members in agreement with the optimal selection of ENSO would reduce the remaining internal noise and increase the credibility of the outcome.

(Q9-Q10) Tibetan Plateau warming and rainfall patterns in eastern China

Q9: How do temperature and precipitation respond when the surface albedo increases/decreases on the Tibetan Plateau? Would the climate changes in the Tibetan Plateau increase the summer monsoon precipitation in eastern China?

Q10: What are the dynamical mechanisms behind? Is Planet Simulator, a model of intermediate complexity, able to capture what GCMs exhibit?

One control run and two sensitivity experiments are performed using a model of intermediate complexity, Planet Simulator, to illustrate the effects of ALCC (in terms of surface albedo) on the climate in the TP and eastern China. The only difference between the two sensitivity experiments is the surface albedo over TP: experiment 'Red' with 50% of the surface albedo in control, and experiment 'Inc' with 150%. The results indicate a cooling/drying trend when there is a higher surface albedo and a warming/wet trend vice versa. The simulated artificial warming has a similar

pattern of the observed data and the model simulation by ECHAM4 (Wang et al., 2008). Similarly, there is a rainfall surplus in eastern China accompanied with the TP warming, indicating that the surface albedo and the summer precipitation in eastern China are physically linked.

The sensitivity experiments reveal that the Planet Simulator is capable of capturing the climate anomaly patterns in eastern China due to the surface albedo changes over TP, although the Planet Simulator has less components than ECHAM4/5. The simulated result confirms the positive effects of surface albedo change over TP on the summer precipitation in eastern China; furthermore, it confirms that the biogeophysical effects of ALCC (other than surface albedo), or the biogeochemical effects of ALCC, or both are opposing the effect of surface albedo change on the summer precipitation in eastern China.

Meanwhile, the sensitivity experiments using identical settings but different atmospheric CO₂ concentration reveal that a higher CO₂ concentration can induce a continental warming and a complex rainfall patterns in central and East Asia. However, its effects are independent from the effects of the surface albedo changes in the TP on the climate in eastern China, although this conclusion is restricted to the present model.

The results shown by the Planet Simulator have similarities compared to that of GCMs ECHAM4 (Wang et al., 2008). The mechanism through which the atmosphere responds to the TP warming can be explained as follows: The westerly winds rising up the isentropes on the eastern side of the mid-tropospheric warm region give ascent over EA and South Korea, which results in enhanced rainfall there and enhances the Western North Pacific subtropical high centered at Okinawa through heating-induced Sverdrup balance. Meanwhile, two Rossby wave trains are excited due to the TP warming (Wang et al., 2008). One has a barotropic structure and propagates downstream along the upper-level westerly jet stream to enhance the anticyclonic circulation to east of Japan. Another wave train developing along the low-level southwesterly monsoon propagates into the South China Sea and enhances the low-level anticyclonic ridge there. The two wave trains deform the Western North Pacific subtropical high in such a way that the low-level southwesterly monsoon strengthens moisture transport toward the East Asia subtropical front and reinforces the precipitation there.

6.2 Outlook

The climate variations are a mixture of internal and external factors. In the present analysis, the role of the solar irradiance on the climate is illustrated by two ensemble simulations (ensemble E1 and E2) forced by a weak solar irradiance (the state-of-the-art reconstructed by Krivova et al., 2007) and a strong solar irradiance (reconstructed by Bard et al., 2000). The comparisons between the two ensembles and the reconstructed climate in EA reveal larger amplitudes in ensemble E2 than E1 during the late MCA and the LIA (see details in Chapter 2 and chapter 3). However,

the order of the uncertainties expressed by the ensemble spread is far beyond the reconstructions, especially in the case of precipitation. The internal variability is so large that the optimal selection result between the simulations and reconstructions must be used with great care. Furthermore, in the analysis of volcanic and ENSO effects (Chapter 4) given the same definition of volcanic eruptions, the difference between ensemble E1 and E2 is rather small as well. The only noticeable exception is the amplitude of winter temperature after eruptions. Considering that the LIA may be characterized not by a lower annual mean temperature but a larger variability (distinct annual cycles in LIA in Chapter 2, Schwarzschild, 2012 and Miller et al., 2012) and that in Europe the model simulates lower winter precipitation in the last millennium than the present (Luterbacher et al., 2010), future work may focus on the annual cycle anomalies, the frequency of extreme events with associated uncertainties in the relevant climatic periods. What are not considered in the current work are the locations and the intensities of the volcanic eruptions, which should be analyzed in forthcoming simulations with large numbers of ensemble members.

Compared to various reconstructed data discussed in the present analysis, the simulated temperature and precipitation in China shows less regional dissimilarities in the last 1200 years (Chapter 2 and chapter 3), these results reveal the necessity of a model with higher resolution. The improvements may be given to, e.g., a more detailed representation of the complex orography, especially over the TP (Blender et al., 2011; Dallmeyer, 2011). A regional model with more details may work as well. An increase in horizontal and vertical resolution normally will increase the credibility or reduce the uncertainties in the model simulations, however, this is not always the case (Zorita, 2012). A comprehensive comparison between models with different resolutions, or between GCMs and regional models, would certainly be welcome. In terms of the uncertainties in the reconstructed/proxy data, one important thing which has to be taken into consideration is the way to interpretate the original data. For example, Holmes et al. (2007) find that rising temperature will often lead to an increase in the oxygen-isotope values of precipitation and will tend to increase the oxygen-isotope of lake water through greater evaporative enrichment, and draw a conclusion that the variations obtained from the ostracode calcite from Suga Lake are not solely a function of changing effective precipitation, the model often used to interpret oxygen-isotope records from lakes in arid to subhumid regions. In other words, the original data sets should be interpreted with great care.

The east and south Asian summer monsoon is highly correlated with the surface temperature and precipitation, runoff in YC. In the full-forcings simulations, the Asian summer monsoon has great influences on the summer precipitation in Northeast China and the TP (Chapter 3). Although the analysis of the comparison between simulated and reconstructed drought index reveal consistency in most parts of China in the year after volcanic eruptions with and without following ENSO events (Chapter 4), the bias remain in central Asia. Therefore, the dynamics underlying the response to the extreme external inputs may be different in observations and simulations, not unlike the dynamic causes of extremes like drought and

wetness which may also be different for observations and simulations (Bothe et al., 2011) with obvious consequences for the estimation of climate change. Meanwhile, compared with the observation, the locations of the Asian monsoon areas is slightly northward-shifted in the present model.

The pattern of the summer precipitation response to ENSO in EA can be captured in ECHAM5 simulations (Hagemann et al., 2006), however, the amplitude of the variations is slightly larger than the observation. One evidence is that after a volcanic eruption with ENSO events in the following winter, the patterns of the simulated temperature and drought index reveal similarities to that of the ENSO events without preceding eruptions (Chapter 4), although this may partly due to the lower threshold of the intensity of eruptions. Meanwhile, one of the model weaknesses is its regularity of 3-4 years (Chapter 3 and 4, Blender et al., 2011), while observations indicate a variability of 2-7 years

The ALCC has a huge influence on the climate in EA and attributes as one plausible cause for the precipitation deficits in the TP and eastern China in the last century as well as the rising fossil fuel CO₂ concentraion. However, what remains unclear is the uncertainties of the two effects of ALCC: the biogeophysical and biogeochemical mechanism. Results from the Chapter 3 and Chapter 5 give us a hint on the positive effects of surface albedo (one facet of biogeophysical effect) over the TP on the summer precipitation in eastern China. The total influence (e.g., the combined effects resulting from the opposing effect from surface albedo and from the evaporation within the biogeophysical effects of ALCC, and the opposing effect from biogeophysical and biogeochemical effects of ALCC) on the East Asian precipitation is still unclear. Note that there is no irrigated agriculture in the simulations, instead it is parameterized as wheat/maize, and its parameterization is rather important in eastern China due to its large planting areas. Therefore, for future analysis sensitivity experiments involved with different parameterizations in the transformation of rice to wheat/maize, with the opposing effects mentioned above, are of essential importance to an improvement of the simulations of present climate and future projection.

Appendix A

Figures

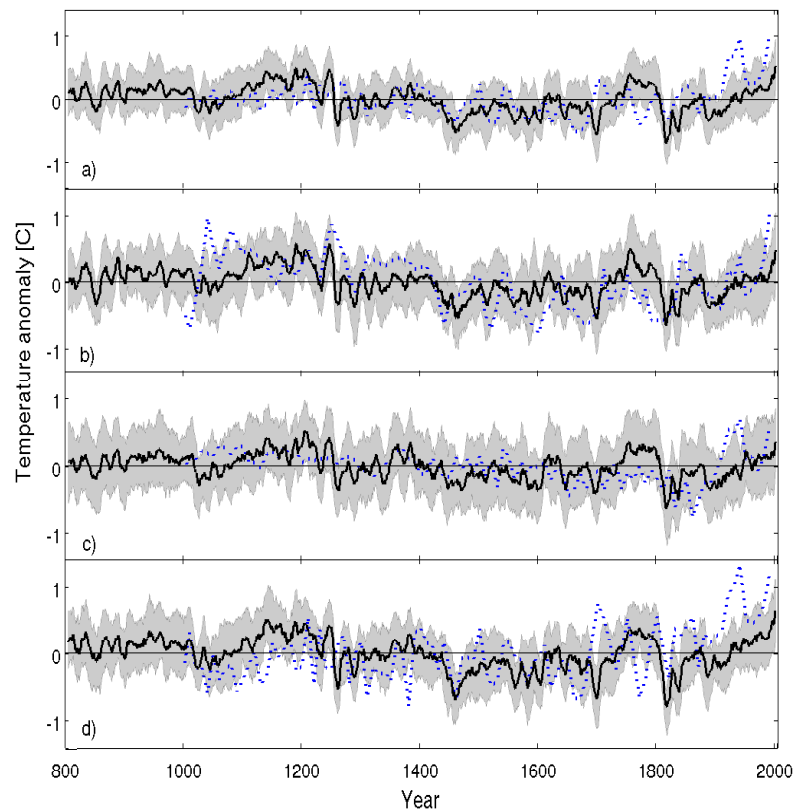


Fig. A.1: As in Fig. 2.7, for ensemble E2: Temperature anomalies [$^{\circ}\text{C}$] in **(a)** China, **(b)** Northeast, **(c)** Southeast, and **(d)** West from simulations and reconstructions: ensemble E2 (black/bold) and ensemble spread (grey/shaded) as 11-year running means of minimum and maximum. Reconstruction by Wang et al. (2007b, blue/dotted). Simulated (reconstructed) anomalies are with respect to the 800-2005 (1000-2000) mean.

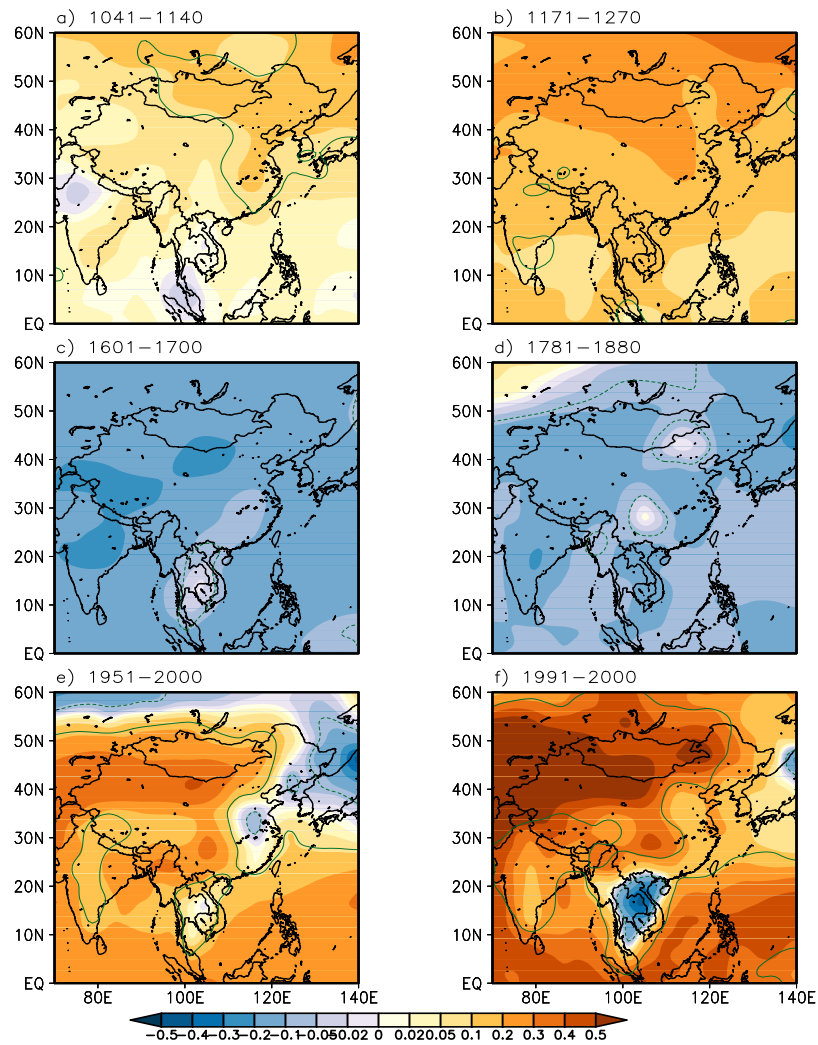


Fig. A.2: As in Fig. 2.8, for ensemble E2: Simulated temperature anomalies [°C] during the periods as indicated (with respect to the overall mean in 800-2005, compare with Fig. 5 in Wang et al. (2007b)). The green contours mark the statistical significance as p-values (representing 90% confidence level) of the Student's t-test.

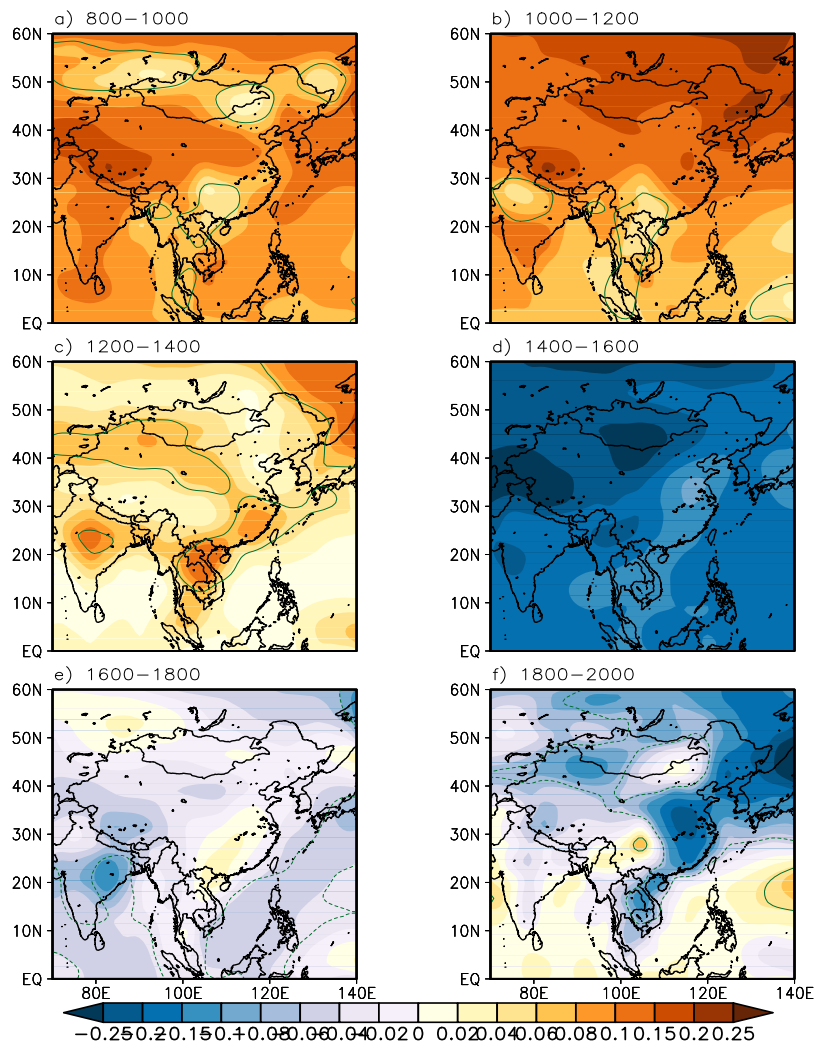


Fig. A.3: As in Fig. 2.9, for ensemble E2: Simulated temperature anomalies as bicentennial means (with respect to the overall mean in 800-2005). The green contours mark the statistical significance as p-values (representing 90% confidence level) of the Student's t-test.

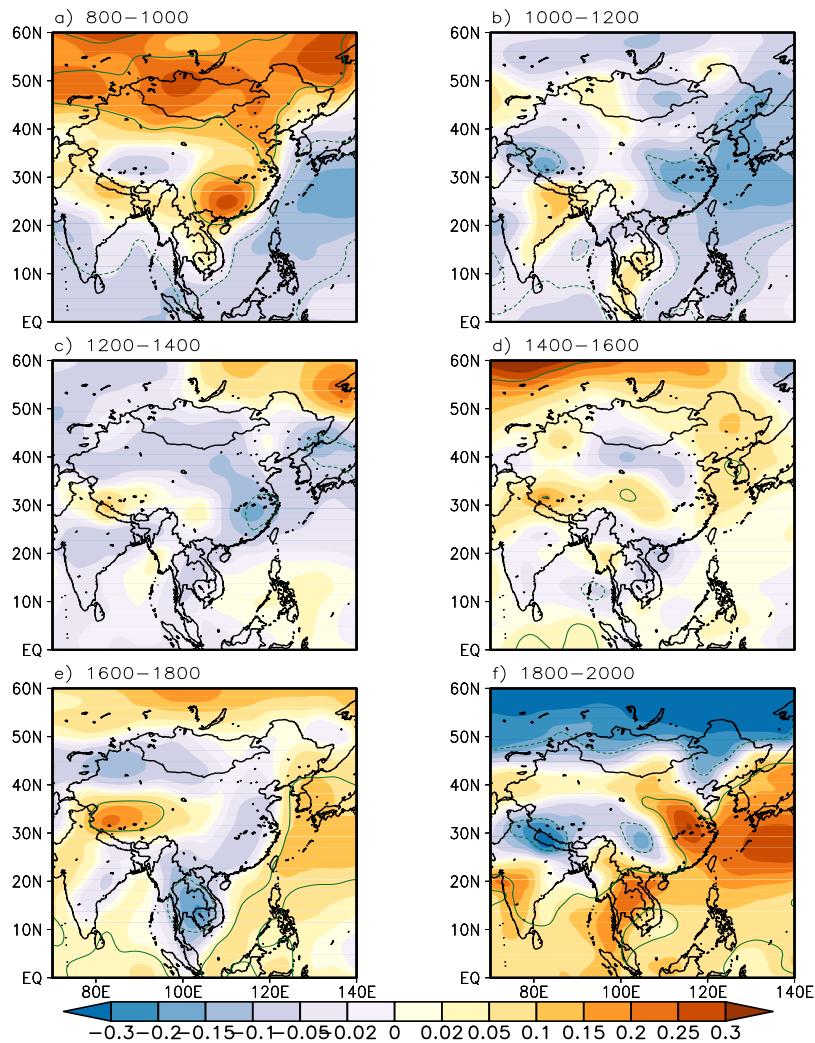


Fig. A.4: As in Fig. 2.10, for ensemble E2: Simulated annual cycle (defined as summer minus winter temperature) as bicentennial means [°C]. The mean annual cycle in 800-2005 is subtracted. The green contours mark the statistical significance as p-values (representing 90% confidence level) of the Student's t-test.

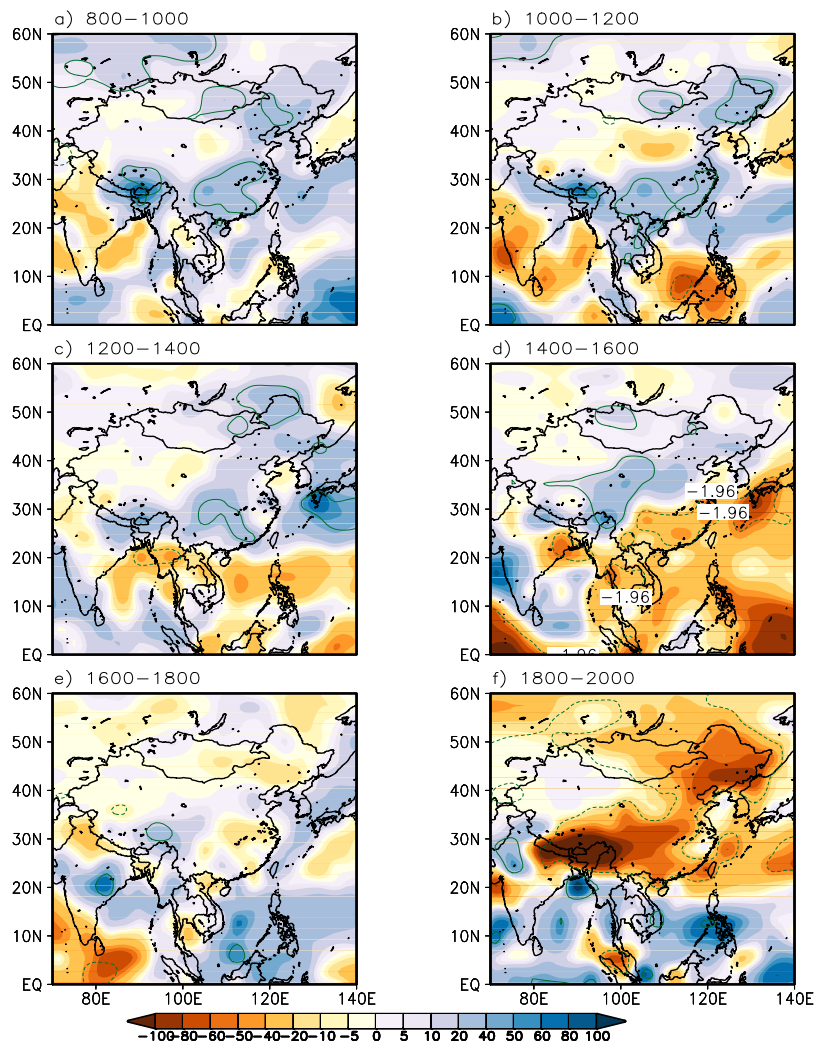


Fig. A.5: As in Fig. 3.6, for ensemble E2: Simulated total precipitation anomalies [mm/month] as bicentennial means (with respect to the overall mean in 800-2005). The green contours mark the statistical significance as p-values (representing 90% confidence level) of the Student's t-test.

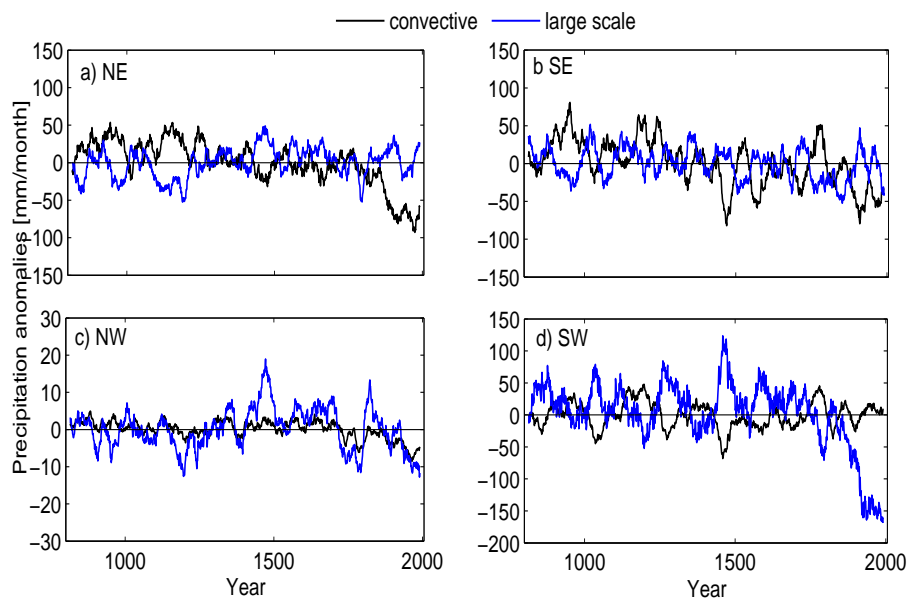


Fig. A.6: As in Fig. 3.9, for ensemble E2: Simulated boreal summer convective (black) and large scale (blue) precipitation anomalies [mm/month] in four regions: **(a)** Northeast (NE), **(b)** Southeast (SE), **(c)** Northwest (NW) and **(d)** Southwest (SW) China: ensemble mean in E2 (bold) and spread obtained by minimum and maximum (shaded). The anomalies are with respect to the overall mean in 800-2005 and smoothed by 30 years.

Appendix B

Methods and third party software

In the present work, two statistical tests are used: the Mann-Whitney U test (also called the Mann-Whitney-Wilcoxon or Wilcoxon rank-sum test) is a non-parametric statistical hypothesis test for assessing whether one of two samples of independent observations tends to have larger values than the other. It is one of the most well-known non-parametric significance tests. It was proposed initially by Gustav Deuchler in 1914 (Kruskal, 1957) and later extended to arbitrary sample sizes and in other ways (Mann and Whitney, 1947). In the present analysis, the method is adopted through matlab at a significance level of 95%.

The Student's t-test is a statistical hypothesis test in which the test statistic follows a Student's t distribution if the null hypothesis is supported. It was introduced by William Sealy Gosset (Box, 1987). It is most commonly applied when the test statistic would follow a normal distribution if the value of a scaling term in the test statistic were known. When the scaling term is unknown and is replaced by an estimate based on the data, the test statistic (under certain conditions) follows a Student's t distribution.

Various software packages are employed available from the Model and Data group at the Max Planck Institute for Meteorology including CDO, matlab, GrADS and PINGO. Standardized Precipitation Index (SPI) transformations and statistical analyses (see Section 4.2) are primarily performed with the statistical software R provided by 'The R Project for Statistical Computing' (Development Core Team, 2005). The respective scripts are to substantial extent due to work by Frank Sienz in the same Theoretical Meteorology group.

The SPI transformation depends on the assumed statistical distribution of monthly precipitation. A false distribution type leads to systematic errors, which are most severe at the upper and lower tails and, therefore, for the extreme values. The gamma distribution, as used by Bordi et al. (2007) to describe precipitation in Sicily, has lead to adequate results. However, this distribution does not hold for all months for the Iceland precipitation time series; for some months better fits can be achieved by the Weibull distribution. To still use a single unifying distribution type the 'Generalized Gamma Distribution' is applied instead:

$$f(x) = \frac{d}{\Gamma(k)} * b^{-dk} * x^{(dk-1)} * \exp(-(\frac{x}{b})^d)$$

with scale parameter b , two shape parameters d and k , and the gamma function $\Gamma(y)$. This version includes as special cases the gamma distribution (by setting $d = 1$) and the Weibull distribution (with $k = 1$). The two shape parameters make maximum likelihood estimation difficult and lead to convergence problems. Therefore, parameter estimation is performed by using the reparameterised version of the generalized gamma distribution. The transformation can also be used to identify possible dryness and wetness changes in terms of SPI values. The solid lines and arrows illustrate the transformation to SPI (Fig. B.1). Further details please see Sienz et al. (2007).

Fig. B.1: The transformation to SPI is illustrated by solid lines and arrows: a gamma distribution (Γ_1 , left) is transformed to the standard normal distribution (Φ , right). Another gamma distribution (Γ_2 , dashed lines, left) is transformed such that the probability differences remain the same on the both sides. Note that the resulting distribution (dashed lines, right) does not have the properties of the standard normal distribution (shown are cumulative distribution functions, figure is from Sienz et al., 2007).

List of Figures

1.1	Spatial pattern of the Medieval Climate Anomaly (MCA) minus the Little Ice Age (LIA) surface temperature difference [$^{\circ}\text{C}$] in reconstructions and model simulations. (A) Proxy-based temperature reconstructions (significant marked), (B) GISS-ER (using the same solar forcing difference as in the NCAR simulation-shown is the ensemble mean); and (C) NCAR CSM 1.4 simulation (Figure is from Mann et al. 2009, reprinted with permission from AAAS.)	3
2.1	Research regions in China: (1) Northeast (NE) China, (2) Southeast (SE) China, (3) West (W) China marked in grid cells in the ECHAM5 T31 model simulation ($\approx 3.75^{\circ}$).	13
2.2	Northern Hemispheric annual means (blue) of (a) net shortwave radiation at the top of the atmosphere [W/m^{-2}] and (b) surface temperature [$^{\circ}\text{C}$] in ensemble E1. 30-year running means are indicated (red).	16
2.3	Annual mean temperature difference [$^{\circ}\text{C}$] of the Medieval Climate Anomaly (MCA) minus the Little Ice Age (LIA, approximately 950-1250 AD minus 1400-1700 AD) in ensemble (a) E1 and (b) E2. . . .	17
2.4	As Fig 2.3 for each ensemble member E1: 10, 12-15, and E2: 21, 25 and 26. Experiment details see Table 2.1.	18
2.5	Temperature anomalies [$^{\circ}\text{C}$] in China from simulations and reconstructions: ensemble E1 (black/solid) and E2 (blue/solid), and reconstructions by Wang et al. (2007b, dotted/red), Yang et al. (2002, dashed/brown), and Ge et al. (2003, dashed/green). The ensemble spread (from ensemble E1) is indicated by the 11-year running means of simulated minimum and maximum anomalies in the ensemble (grey/shaded).	20
2.6	Power spectra of the mean temperature in China: (a) simulation (ensemble E1 with weak solar irradiance), (b) reconstruction by Wang et al. (2007b), and (c) reconstruction by Yang et al. (2002, solid) and Ge et al. (2003, dashed). In (a) the 3-4 year ENSO cycle is marked.	21

2.7	Temperature anomalies [$^{\circ}\text{C}$] in (a) China, (b) Northeast China, (c) Southeast China, and (d) West China from simulations and reconstructions: ensemble E1 (black/bold) and ensemble spread (grey/shaded) as 11-year running means of minimum and maximum; Reconstructions (blue/dotted) by Wang et al. (2007b). Simulated (reconstructed) anomalies are with respect to the 800-2005 (1000-2000) mean.	22
2.8	Simulated temperature anomalies [$^{\circ}\text{C}$] during the periods as indicated (with respect to the overall mean in 800-2005, compare with Fig. 5 in Wang et al., 2007b). The green contours mark the statistical significance as p-values (representing 90% confidence level) of the Student's t-test.	24
2.9	Simulated temperature anomalies [$^{\circ}\text{C}$] as bicentennial means (with respect to the overall mean in 800-200). The green contours mark the statistical significance as p-values (representing 90% confidence level) of the Student's t-test.	26
2.10	Simulated annual cycle (defined as summer minus winter temperature) as bicentennial means [$^{\circ}\text{C}$]. The mean annual cycle in 800-2005 is subtracted. The green contours mark the statistical significance as p-values (representing 90% confidence level) of the Student's t-test.	27
3.1	Research regions in China: (1) Northeast (NE) China, (2) Southeast (SE) China, (3) Northwest (NW) China and (4) Southwest (SW) China marked in grid cells in the ECHAM5 T31 model simulation ($\approx 3.75^{\circ}$).	34
3.2	Research regions in China: (1) Yangtze catchment and (2) Tibetan Plateau in the grid cells of the ECHAM5 T31 model simulation ($\approx 3.75^{\circ}$).	34
3.3	Power spectra of (a) area averaged runoff and soil wetness, and (b) temperature and precipitation in the Yangtze catchment. The solid lines indicate power-laws $S(f) \approx f^{-\beta}$ with exponents $\beta = 0.6$ (bold), and $\beta = 0.1$ (thin line).	40
3.4	Detrended fluctuation analysis (DFA) of area averaged runoff, soil wetness, temperature, and precipitation in the Yangtze catchment. The solid lines indicate power-laws in the fluctuation function $F(t) \approx t^{\alpha}$ with $\alpha = 0.8$ (bold), $\alpha = 0.55$ (thin solid), and $\alpha = 0.5$ (dashed, no memory).	40
3.5	Power spectra of (a) area averaged snow depth and snow melt (shifted) on the Tibetan Plateau and (b) monsoon indices and ENSO. All spectra in (b) are peaked at 3-4 years.	41

- 3.6 Simulated total precipitation anomalies [mm/month] as bicentennial means (with respect to the overall mean in 800-2005 AD. The green contours mark the statistical significance as p-values (representing 90% confidence level) of the Student's t-test. 45
- 3.7 Simulated precipitation [mm/month] anomalies (left axis) and reconstructed drought index (right axis) in **(a)** China, and in four regions **(b)** Northeast (NE) China, **(c)** Southeast (SE) China, **(d)** Northwest (NW) China and **(e)** Southwest (SW) China. Ensemble mean in E1 (black/bold) and spread are obtained by minimum and maximum (grey/shaded). Regions for reconstructed drought index in China see Section 3.2. The anomalies are calculated with respect to the time means in the corresponding data set during the whole period and smoothed by 30 years. 47
- 3.8 Power spectra of **(a)** simulated total precipitation in ensemble E1 (red) and E2 (blue); **(b)** reconstructed drought index by Central Meteorological Bureau (CMB, 1981), Zheng et al. (2006) and Cook et al. (2010). The peaks are marked. 48
- 3.9 Simulated summer convective (black) and large scale (blue) precipitation anomalies [mm/month] in four regions: **(a)** Northeast (NE) China, **(b)** Southeast (SE) China, **(c)** Northwest (NW) China, and **(d)** Southwest (SW) China in ensemble E1. The anomalies are calculated with respect to the overall mean in 800-2005 and smoothed by 30 years. 49
- 3.10 Simulated summer total precipitation (left panel, mm/month), surface albedo (middle panel) and evaporation (right panel, 10^{-5}kg/m^2) in four regions: **(a)** Northeast (NE), **(b)** Southeast (SE), **(c)** Northwest (NW), and **(d)** Southwest (SW) China in experiments as indicated (see Table 3.1). The anomalies are calculated with respect to the overall mean in 800-2005 and smoothed by 30 years. Depicted is only the time period after 1700, when clear temperature trends emerge. 50
- 3.11 Clear sky net top solar radiation (left panel, W/m^2), net surface radiation (middle panel, W/m^2) and net thermal radiation (right panel, W/m^2) in four regions: **(a)** Northeast (NE) China, **(b)** Southeast (SE) China, **(c)** Northwest (NW) China and **(d)** Southwest (SW) China in experiments as indicated (see Table 3.1). The anomalies are calculated with respect to the overall mean in 800-2005 and smoothed by 30 years. Depicted is only the time period after 1700, when clear temperature trends emerge. 52

3.12	Latent heat flux (left panel, W/m^2), sensible heat flux (middle panel, W/m^2) and cloud cover (right panel) in four regions: (a) Northeast (NE) China, (b) Southeast (SE) China, (c) Northwest (NW) China and (d) Southwest (SW) China in experiments as indicated (see Table 3.1). The anomalies are calculated with respect to the overall mean in 800-2005 and smoothed by 30 years. Depicted is only the time period after 1700, when clear temperature trends emerge. . . .	53
3.13	Annual mean N_2O , CO_2 (left panel, unit: ppb and ppm) and CH_4 concentrations (right panel, ppb) in the atmosphere in ensemble E1.	54
3.14	Net top solar radiation (left panel, W/m^2), net surface radiation (middle panel, W/m^2) and net thermal radiation (right panel, W/m^2) in four regions: (a) Northeast (NE) China, (b) Southeast (SE) China, (c) Northwest (NW) China and (d) Southwest (SW) China in experiments as indicated (see Table 3.1). The anomalies are calculated with respect to the overall mean in 800-2005 and smoothed by 30 years. Depicted is only the time period after 1700, when clear temperature trends emerge.	55
3.15	(a) The East Asia summer Monsoon Index (EAMI) and (b) the Monsoon Hadley circulation Index (MHI) anomalies in ensemble E1/E2 (left panel) in 800-2005 AD and in sensitivity experiments after 1700 AD (right panel). Experiments are indicated (see Table 3.1). The right panel shows only the period after 1700 AD when clear EAMI and MHI trends emerge. All the anomalies are calculated with respect to the overall mean in 800-2005 and smoothed by 30 years. . .	56
3.16	Correlation coefficient between summer precipitation anomalies and (a) the East Asia summer Monsoon Index (EAMI) and (b) the Monsoon Hadley circulation Index (MHI) anomalies (at 95% level)	56
4.1	(a) Annual mean total solar irradiation in ensemble E1 (30 years running mean: red) for the whole simulation period (left panel) and the Dalton minimum (1790-1830, right panel) based on the reconstruction by Krivova et al. (2007), (b) Aerosol optical depth (dimensionless fraction), and (c) Effective radius (μm), in (b) and (c) latitude belts are separated. The Dalton Minimum includes the Tambora eruption in 1815.	65
4.2	(a) Global annual mean temperature anomalies [$^{\circ}C$] and (b) summer Standardized Precipitation Index (SPI, JJA) in ensemble E1 in the year after volcanic eruptions without ENSO events. Significant areas are marked by 'x'.	71
4.3	Winter temperature anomalies [$^{\circ}C$] after volcanic eruptions without ENSO events (neutral, $ PC1-SST < 1$) in ensemble (a) E1 and (b) E2. Significant areas are marked by 'x'.	72

- 4.4 Examples of exponential fits to averaged temperature anomalies. Location 1: 102°E/22°N (Northeast China, recovery time scale $\tau \approx 3$ yrs, $\Delta T_0 \approx -0.5^\circ\text{C}$), location 2: 116°E/43°N (Southwest China, $\tau \approx 2$ yrs, $\Delta T_0 \approx -0.3^\circ\text{C}$) 73
- 4.5 **(a)** Temperature amplitude ΔT_0 [$^\circ\text{C}$] and **(b)** Relaxation time scale τ [years] of the temperature decay averaged after 31 volcanic eruptions in ensemble E1 without ENSO events (neutral, $|\text{PC1-SST}| < 1$) during the preceding two winters. Significant changes marked by 'x'. 74
- 4.6 Simulated annual mean temperature anomalies [$^\circ\text{C}$] in the ensemble E1 in East Asia in the year after: **(a)** volcanic eruptions with no ENSO events (neutral, $|\text{PC1-SST}| < 1$), **(b)** El Niño and **(c)** La Niña events without preceding eruption, **(d)** eruptions with El Niño events, **(e)** eruptions with La Niña events. Significant areas are marked by 'x'. . 75
- 4.7 Reconstructed temperature anomalies [$^\circ\text{C}$] for volcanic eruptions without ENSO events according to list **(a)** A15 (Ammann et al., 2007), **(b)** AN46 (Ammann and Naveau, 2003) and **(c)** F12 (Fischer et al., 2007), and volcanic eruptions with El Niño events in the following winter according to list **(d)** A1 (Ammann et al., 2007), **(e)** AN7 (Ammann and Naveau, 2003) and **(f)** F2 (Fischer et al., 2007) (details of the list of eruptions see Table 4.3 and Table 4.4). Significant areas are marked by 'x'. 76
- 4.8 As in Fig. 4.6 for summer (JJA) mean of the monthly Standardized Precipitation Index (SPI) 77
- 4.9 As in Fig. 4.7 for summer (JJA) mean of the Palmer Drought Severity Index (PDSI). The list are for **(a)** A10 (Ammann et al., 2007), **(b)** AN46 (Ammann and Naveau, 2003) and **(c)** F12 (Fischer et al., 2007), and volcanic eruptions with El Niño events in the following winter according to list **(d)** A1 (Ammann et al., 2007), **(e)** AN7 (Ammann and Naveau, 2003) and **(f)** F2 (Fischer et al., 2007) (details of the list of eruptions see Table 4.3 and Table 4.4). Significant areas are marked by 'x'. 78
- 4.10 **(a)** Temperature anomalies [$^\circ\text{C}$] in China in simulations and reconstructions for 1780-1850. The simulated (solid) curves are ensemble means for E1 and E2 (thin grey lines indicate all eight ensemble members), and the reconstructed (dashed) lines refer Yang et al. (2002), Ge et al. (2003), Wang et al. (2007b) and Mann et al. (2009); **(b)** Decadal mean simulated Standardized Precipitation Index (SPI, solid, as in (a), left axis) and reconstructed drought index in Southeast China (dashed, right axis, decadal means) from Zheng et al. (2006), Central Meteorological Bureau (CMB, 1981), and Cook et al. (2010). The Dalton minimum (1790-1830) and the Tambora eruption (1815) are marked 80

- 4.11 ENSO (PC1-SST) and climate in China during the cold decade of 1810 to 1820 embedding the year without summer (1816): **(a)** PC1-SST in eight simulations of ensembles E1 and E2; grey shades indicate 'strong' (S) and 'moderate+' (M+) reconstructed El Niño events (see the definition by Quinn, 1993). Selected ENSO patterns: E1-3 (neutral, green, hidden by the red symbol), E1-4 (El Niño, yellow), E1-2 (La Niña, blue), E2-3 (optimal, red); **(b)** temperature anomalies in China and **(c)** SPI in Southeast China for selected ENSO patterns as in (a). 81
- 4.12 Temperature anomalies in 1816 (annual mean [°C], left column) and SPI (JJA, right column) in four simulations with different ENSO patterns (see also Fig. 4.11): **(a)** Neutral ($|PC1-SST| < 1$), **(b)** El Niño, **(c)** La Niña, and **(d)** optimal realization (compare Quinn, 1993) . . . 82
- 4.13 **(a)** The East Asian Summer Monsoon Index (EAMI) and **(b)** the Monsoon Hadley circulation index (MHI) anomalies during the period from three years before to 10 years after the event year of: volcanic eruptions without winter ENSO events (neutral, $|PC1-SST| < 1$, red), El Niño (blue) and La Niña (green) events without preceding eruption, eruptions with El Niño events (magenta), and eruptions with La Niña events (cyan). Dashed lines are twice the standard deviations during the whole period 800-2005 AD. 84
- 5.1 Location of Tibetan Plateau in Planet Simulator in resolution T42 (approximately 27.5°N-37.5°N, 75°E-104°E) with altitudes higher than 3000m. 90
- 5.2 Surface temperature [°C] and total precipitation [mm/day] in summer in control run of model **(a-b)** Planet Simulator, **(c-d)** ECHAM5. . . . 91
- 5.3 The ensemble mean difference of surface temperature (left panel, °C) and total precipitation (right panel, mm/year) in summer between experiment **(a-b)** 'Red'-'Control', **(c-d)** 'Inc'-'Control' and **(e-f)** 'Red'-'Inc'. Experiment details see Table 5.1. Significant areas are marked by 'x'. 92
- 5.4 The ensemble mean difference of surface temperature (left panel, °C) and total precipitation (right panel, mm/year) in summer between experiment **(a-b)** 'C'-'Control', **(c-d)** 'Red-C'-'C', **(e-f)** 'Inc-C'-'C', and **(g-h)** 'Red-C'-'Inc-C'. Experiment details see Table 5.1. Significant areas are marked by 'x'. 93
- 5.5 The ensemble mean difference between experiment 'Red' and 'Inc' of **(a)** 200mb Wind [m/s] and **(b)** 850mb Wind [m/s] in summer. The letters 'A' and 'C' denote anticyclonic and cyclonic circulation center, respectively. 95

- A.1 As in Fig. 2.7, for ensemble E2: Temperature anomalies [$^{\circ}\text{C}$] in **(a)** China, **(b)** Northeast, **(c)** Southeast, and **(d)** West from simulations and reconstructions: ensemble E2 (black/bold) and ensemble spread (grey/shaded) as 11-year running means of minimum and maximum. Reconstruction by Wang et al. (2007b, blue/dotted). Simulated (reconstructed) anomalies are with respect to the 800-2005 (1000-2000) mean. 111
- A.2 As in Fig. 2.8, for ensemble E2: Simulated temperature anomalies [$^{\circ}\text{C}$] during the periods as indicated (with respect to the overall mean in 800-2005, compare with Fig. 5 in Wang et al. (2007b). The green contours mark the statistical significance as p-values (representing 90% confidence level) of the Student's t-test. 112
- A.3 As in Fig. 2.9, for ensemble E2: Simulated temperature anomalies as bicentennial means (with respect to the overall mean in 800-2005. The green contours mark the statistical significance as p-values (representing 90% confidence level) of the Student's t-test. 113
- A.4 As in Fig. 2.10, for ensemble E2: Simulated annual cycle (defined as summer minus winter temperature) as bicentennial means [$^{\circ}\text{C}$]. The mean annual cycle in 800-2005 is subtracted. The green contours mark the statistical significance as p-values (representing 90% confidence level) of the Student's t-test. 114
- A.5 As in Fig. 3.6, for ensemble E2: Simulated total precipitation anomalies [mm/month] as bicentennial means (with respect to the overall mean in 800-2005). The green contours mark the statistical significance as p-values (representing 90% confidence level) of the Student's t-test. 115
- A.6 As in Fig. 3.9, for ensemble E2: Simulated boreal summer convective (black) and large scale (blue) precipitation anomalies [mm/month] in four regions: **(a)** Northeast (NE), **(b)** Southeast (SE), **(c)** Northwest (NW) and **(d)** Southwest (SW) China: ensemble mean in E2 (bold) and spread obtained by minimum and maximum (shaded). The anomalies are with respect to the overall mean in 800-2005 and smoothed by 30 years. 116
- B.1 The transformation to SPI is illustrated by solid lines and arrows: a gamma distribution ($\Gamma 1$, left) is transformed to the standard normal distribution (Φ , right). Another gamma distribution ($\Gamma 2$, dashed lines, left) is transformed such that the probability differences remain the same on the both sides. Note that the resulting distribution (dashed lines, right) does not have the properties of the standard normal distribution (shown are cumulative distribution functions, figure is from Sienz et al., 2007). 118

List of Tables

2.1	List of the millennium experiments used in the present chapter carried out with ECHAM5/MPIOM/JSBACH at T31 resolution.	13
2.2	Summary of reconstructed centennial regional temperature anomalies [$^{\circ}\text{C}$] in China in 800-2000 AD.	15
3.1	List of the millennium experiments used in the present chapter carried out with ECHAM5/MPIOM/JSBACH at T31 resolution.	33
3.2	Correlations of annual hydrological time series within the Yangtze catchment and with Tibetan Plateau snow, monsoon indices and ENSO (only 99%-significant values are shown, $ r > 0.1$).	42
3.3	Correlations of decadal hydrological time series within the Yangtze catchment and with Tibetan Plateau snow, monsoon indices and ENSO (only 95%-significant values are shown, $ r > 0.1$).	42
3.4	Summary of: (I) the trend of climate variables after 1800 AD in Northeast (NE), Southeast (SE), Northwest (NW) and Southwest (SW) China: Precipitation (PRCP), large scale precipitation (APRL), convective precipitation (APRC), surface albedo (ALBEDO), evaporation (EVAP), latent heat flux (AHFL), sensible heat flux (AHFS), cloud cover (CC), net top radiation (clear sky, SRO), net surface radiation (clear sky, SR), net thermal radiation (clear sky, TR), net top radiation (SRO-c), net surface radiation (SR-c) and net thermal radiation (TR-c). Experiments are indicated by different colors: full-forcings ensemble E1 (red), sensitivity experiment 02 (blue), 07 (green) and 08 (magenta). Experiments details see Table 3.1. (II) the possible causes for precipitation decrease in four regions in China after 1800 AD. '+'/'-' indicates positive/negative influence and question marks indicate uncertainty.	60

4.1	List of the 21 selected volcanic eruptions in 800-2005 in the model simulations in each member (the eruption year is defined by a decrease in net top solar irradiation of at least -2.0 W/m^2). The Volcanic Explosivity Index (VEI) is included and question marks indicate uncertainty (Newhall and Self 1982; Peng et al. 2010; Smithsonian National Museum of Natural History/Washington, Global Volcanism Program, 2011).	66
4.2	Standardized Precipitation Index (SPI) classification and event-probability (P in %, McKee et al. 1993)	68
4.3	List of volcanic eruptions without El Niño events used for the reconstructed temperature and the Palmer Drought Severity Index (PDSI) in summer (JJA). The sources for volcanic eruptions are ⁽¹⁾ Ammann et al. (2007), ⁽²⁾ Ammann and Naveau (2003) and ⁽³⁾ Fischer et al. (2007); * While the data is available after 1250, the reconstructed PDSI starts from 1300 (missing years in italics).	70
4.4	List of volcanic eruptions with El Niño events used for the reconstructed temperature and the Palmer Drought Severity Index (PDSI) in summer (JJA). The sources for volcanic eruptions are ⁽¹⁾ Ammann et al. (2007), ⁽²⁾ Ammann and Naveau (2003) and ⁽³⁾ Fischer et al. (2007). The event years with reconstructed El Niño are according to Gergis and Fowler (2006).	70
5.1	List of the experiments used in the present chapter carried out by the Planet Simulator. Experiment 'Red' refers to a 'Reduction' of 50% surface albedo in the TP, and 'Inc' refers to an 'Increase' of 50% of the surface albedo in the Tibetan Plateau, i.e. 150%. The atmospheric CO ₂ concentration is prescribed at 360ppm level. For a 'Comparison', another two sensitivity experiments with identical settings but lower CO ₂ concentration (280ppm) are performed and the corresponding experiment names are added by a 'C'.	89

Bibliography

- Adams, J., M. Mann, and C. Ammann, 2003: Proxy evidence for an El Niño-like response to volcanic forcing. *Nature*, **426**, 274–278.
- Ammann, C., F. Joos, D. Schimel, B. Otto Bliesner, and R. Tomas, 2007: Solar influence on climate during the past millennium: Results from transient simulations with the NCAR Climate System Model. *Proceedings of the National Academy of Sciences*, **104** (10), 3713–3718.
- Ammann, C. and P. Naveau, 2003: Statistical analysis of tropical explosive volcanism occurrences over the last 6 centuries. *Geophysical Research Letters*, **30** (5), 1210.
- Anchukaitis, K., B. Buckley, E. Cook, B. Cook, R. D'Arrigo, and C. Ammann, 2010: Influence of volcanic eruptions on the climate of the Asian monsoon region. *Geophysical Research Letters*, **37** (22), L22 703.
- Angell, J. and J. Korshover, 1985: Surface Temperature Changes Following the Six Major Volcanic Episodes between 1780 and 1980. *Journal of Applied Meteorology*, **24**, 937–951.
- Atwell, W., 2001: Volcanism and short-term climatic change in East Asian and world history, c. 1200-1699. *Journal of World History*, **12** (1), 29–98.
- Bard, E., G. Raisbeck, F. Yiou, and J. Jouzel, 2000: Solar irradiance during the last 1200 years based on cosmogenic nuclides. *Tellus B*, **52** (3), 985–992.
- Bauer, E., M. Claussen, V. Brovkin, and A. Huenerbein, 2003: Assessing climate forcings of the Earth system for the past millennium. *Geophysical Research Letters*, **30** (6), 1276.
- Berkelhammer, M., A. Sinha, M. Mudelsee, H. Cheng, R. Edwards, and K. Cannariato, 2010: Persistent multidecadal power of the Indian Summer Monsoon. *Earth and Planetary Science Letters*, **290**, 166–172.
- Blender, R. and K. Fraedrich, 2006: Long-term memory of the hydrological cycle and river runoffs in China in a high-resolution climate model. *International Journal of Climatology*, **26** (12), 1547–1565.

- Blender, R., X. Zhu, D. Zhang, and K. Fraedrich, 2011: Yangtze Runoff, Precipitation, and the East Asian Monsoon in a 2800 years Climate Control Simulation. *Quaternary International*, **244**, 194–201.
- Bordi, I., K. Fraedrich, J. Jiang, and A. Sutera, 2004: Spatio-temporal variability of dry and wet periods in eastern China. *Theoretical and Applied Climatology*, **79 (1)**, 81–91.
- Bordi, I., K. Fraedrich, M. Petitta, and A. Sutera, 2007: Extreme value analysis of wet and dry periods in Sicily. *Theoretical and applied climatology*, **87 (1)**, 61–71.
- Bothe, O., K. Fraedrich, and X. Zhu, 2011: Large-scale circulations and Tibetan Plateau summer drought and wetness in a high-resolution climate model. *International Journal of Climatology*, **31 (6)**, 832–846.
- Box, J., 1987: Guinness, Gosset, Fisher, and small samples. *Statistical Science*, **2 (1)**, 45–52.
- Bradley, R., 2000: 1000 years of climate change. *Science*, **288**, 1353–1354.
- Bradley, R., M. Hughes, and H. Diaz, 2003: Climate in medieval time. *Science*, **302**, 404–405.
- Brovkin, V., S. Lorenz, J. Jungclaus, T. Raddatz, C. Timmreck, C. Reick, J. Segschneider, and K. Six, 2010: Sensitivity of a coupled climate-carbon cycle model to large volcanic eruptions during the last millennium. *Tellus B*, **62B**, 674–681.
- Brovkin, V., S. Sitch, W. Von Bloh, M. Claussen, E. Bauer, and W. Cramer, 2004: Role of land cover changes for atmospheric CO₂ increase and climate change during the last 150 years. *Global Change Biology*, **10 (8)**, 1253–1266.
- Buckley, B., K. Anchukaitis, D. Penny, R. Fletcher, E. Cook, M. Sano, L. Nam, et al., 2010: Climate as a contributing factor in the demise of Angkor, Cambodia. *Proceedings of the National Academy of Sciences*, **107 (15)**, 6748–6752.
- Büntgen, U., W. Tegel, K. Nicolussi, M. McCormick, D. Frank, V. Trouet, J. Kaplan, et al., 2011: 2500 years of European climate variability and human susceptibility. *Science*, **331**, 578–582.
- Burgman, R., R. Seager, A. Clement, and C. Herweijer, 2010: Role of tropical Pacific SSTs in global medieval hydroclimate: A modeling study. *Geophysical Research Letters*, **37 (6)**, L06705.
- Central Meteorological Bureau, (Ed.) , 1981: *Yearly charts of dryness/wetness in China for the last 500 years (in Chinese)*. Cartographic Publishing House, Beijing, China, 201 pp.

- Chase, T., R. Pielke Sr, T. Kittel, R. Nemani, and S. Running, 2000: Simulated impacts of historical land cover changes on global climate in northern winter. *Climate Dynamics*, **16 (2)**, 93–105.
- Chen, F., J. Chen, J. Holmes, I. Boomer, P. Austin, J. Gates, N. Wang, et al., 2010: Moisture changes over the last millennium in arid central Asia: a review, synthesis and comparison with monsoon region. *Quaternary Science Reviews*, **29**, 1055–1068.
- Clift, P. and R. Plumb, 2008: *The Asian monsoon: causes, history and effects*. Cambridge University Press Cambridge, 270 pp.
- Cole Dai, J., D. Ferris, A. Lanciki, J. Savarino, M. Baroni, and M. Thiemens, 2009: Cold decade (AD 1810–1819) caused by Tambora (1815) and another (1809) stratospheric volcanic eruption. *Geophysical Research Letters*, **36 (6)**, L22 703.
- Compo, G. and P. Sardeshmukh, 2010: Removing ENSO-related variations from the climate record. *Journal of Climate*, **23 (8)**, 1957–1978.
- Cook, E., K. Anchukaitis, B. Buckley, R. D'Arrigo, G. Jacoby, and W. Wright, 2010: Asian monsoon failure and megadrought during the last millennium. *Science*, **328**, 486–489.
- Crowley, T., S. Baum, K. Kim, G. Hegerl, and W. Hyde, 2003: Modeling ocean heat content changes during the last millennium. *Geophysical Research Letters*, **30 (18)**, 1932.
- Crowley, T., G. Zielinski, B. Vinther, R. Udisti, K. Kreutz, J. Cole Dai, and E. Castellano, 2008: Volcanism and the Little Ice Age. *PAGES news*, **16 (2)**, 22–23.
- Dai, J., E. Mosley Thompson, and L. Thompson, 1991: Ice core evidence for an explosive tropical volcanic eruption 6 years preceding Tambora. *Journal of Geophysical Research*, **96 (D9)**, 17 361–17 366.
- Dallmeyer, A. F., 2011: Holocene climate and vegetation change in the Asian monsoon region. Ph.D. thesis, School of Integrated Climate System Sciences; University Hamburg.
- D'Arrigo, R., R. Wilson, and A. Tudhope, 2009: The impact of volcanic forcing on tropical temperatures during the past four centuries. *Nature Geoscience*, **2 (1)**, 51–56.
- Davis, M., L. Thompson, T. Yao, and N. Wang, 2005: Forcing of the Asian monsoon on the Tibetan Plateau: Evidence from high-resolution ice core and tropical coral records. *Journal of Geophysical Research*, **110**, D04 101.
- Denman, K., G. Brasseur, A. Chidthaisong, P. Ciais, P. Cox, R. Dickinson, D. Hauglustaine, et al., 2007: *Couplings between changes in the climate system*

- and biogeochemistry. Climate change 2007: The physical science basis. Contribution of Working Group I to the Fourth Assessment Report of the Intergovernmental Panel on Climate Change.* Cambridge University Press, Cambridge, United Kingdom and New York.
- Development Core Team, R., 2005: R: A language and environment for statistical computing. <http://www.r-project.org>.
- Diaz, H., R. Trigo, M. Hughes, M. Mann, E. Xoplaki, and D. Barriopedro, 2011: Spatial and temporal characteristics of climate in Medieval Times revisited. *Bulletin of the American Meteorological Society*, **92**, 1487–1500.
- Ding, Y. and J. Chan, 2005: The East Asian summer monsoon: an overview. *Meteorology and Atmospheric Physics*, **89 (1)**, 117–142.
- Ding, Y., G. Ren, Z. Zhao, Y. Xu, Y. Luo, Q. Li, and J. Zhang, 2007: Detection, causes and projection of climate change over China: An overview of recent progress. *Advances in Atmospheric Sciences*, **24 (6)**, 954–971.
- Ding, Y., Z. Wang, and Y. Sun, 2008: Inter-decadal variation of the summer precipitation in East China and its association with decreasing Asian summer monsoon. Part I: Observed evidences. *International Journal of Climatology*, **28 (9)**, 1139–1162.
- Duan, A. and G. Wu, 2005: Role of the Tibetan Plateau thermal forcing in the summer climate patterns over subtropical Asia. *Climate dynamics*, **24 (7)**, 793–807.
- Duan, K., T. Yao, and L. Thompson, 2004: Low-frequency of southern Asian monsoon variability using a 295-year record from the Dasuopu ice core in the central Himalayas. *Geophysical Research Letters*, **31**, L16 209.
- Emile Geay, J., R. Seager, M. Cane, E. Cook, and G. Haug, 2008: Volcanoes and ENSO over the past millennium. *Journal of Climate*, **21**, 3134–3148.
- Fischer, E., J. Luterbacher, E. Zorita, S. Tett, C. Casty, and H. Wanner, 2007: European climate response to tropical volcanic eruptions over the last half millennium. *Geophysical Research Letters*, **34 (5)**, L05 707.
- Foley, J., M. Costa, C. Delire, N. Ramankutty, and P. Snyder, 2003: Green surprise? How terrestrial ecosystems could affect earth's climate. *Frontiers in Ecology and the Environment*, **1 (1)**, 38–44.
- Fraedrich, K., 1986: Estimating the dimensions of weather and climate attractors. *Journal of the atmospheric sciences*, **43 (5)**, 419–432.
- Fraedrich, K. and R. Blender, 2003: Scaling of atmosphere and ocean temperature correlations in observations and climate models. *Physical Review Letters*, **90 (10)**, 108 501.

- Fraedrich, K., H. Jansen, E. Kirk, U. Luksch, and F. Lunkeit, 2005: The Planet Simulator: Towards a user friendly model. *Meteorologische Zeitschrift*, **14 (3)**, 299–304.
- Fraedrich, K., E. Kirk, and F. Lunkeit, 1998: PUMA: Portable University Model of the Atmosphere. *Technical Report 16*, Deutsches Klimarechenzentrum.
- Friedlingstein, P., et al., 2006: Climate-carbon cycle feedback analysis: Results from the C4MIP model intercomparison. *Journal of Climate*, **19 (14)**, 3337–3353.
- Frölicher, T., F. Joos, and C. Raible, 2011: Sensitivity of atmospheric CO₂ and climate to explosive volcanic eruptions. *Biogeosciences*, **8**, 2317–2339.
- Ge, Q., S. Wang, X. Wen, C. Shen, and Z. Hao, 2007: Temperature and precipitation changes in China during the Holocene. *Advances in Atmospheric Sciences*, **24 (6)**, 1024–1036.
- Ge, Q., S. Wang, and J. Zheng, 2006: Reconstruction of temperature series in China for the last 5000 years (in Chinese). *Progress in Natural Science*, **16 (6)**, 838–845.
- Ge, Q. and W. Wu, 2011: Climate during the Medieval Climate Anomaly in China. *PAGES news*, **19**, 24–26.
- Ge, Q., J. Zheng, X. Fang, Z. Man, X. Zhang, P. Zhang, and W. Wang, 2003: Winter half-year temperature reconstruction for the middle and lower reaches of the Yellow River and Yangtze River, China, during the past 2000 years. *The Holocene*, **13 (6)**, 933–940.
- Ge, Q., J. Zheng, Z. Hao, X. Shao, W. Wang, and J. Luterbacher, 2010: Temperature variation through 2000 years in China: An uncertainty analysis of reconstruction and regional difference. *Geophysical Research Letters*, **37 (3)**, L03 703.
- Gergis, J. and A. Fowler, 2006: How unusual was late 20th century El Niño-Southern Oscillation (ENSO)? Assessing evidence from tree-ring, coral, ice-core and documentary palaeoarchives, AD 1525-2002. *Advances in Geosciences*, **6**, 173–179.
- Gershunov, A., N. Schneider, and T. Barnett, 2001: Low-frequency modulation of the ENSO-Indian monsoon rainfall relationship: Signal or noise? *Journal of Climate*, **14 (11)**, 2486–2492.
- Global Volcanism Program, 2011: Smithsonian National Museum of Natural History, Washington. Last access in November 2011 at http://www.volcano.si.edu/world/find_eruptions.cfm.
- Goldewijk, K., 2005: Three centuries of global population growth: A spatial referenced population (density) database for 1700–2000. *Population and Environment*, **26 (4)**, 343–367.

- González Rouco, F., L. Fernández Donado, C. Raible, D. Barriopedro, J. Luterbacher, J. Jungclaus, D. Swingedouw, et al., 2011: Medieval Climate Anomaly to Little Ice Age transition as simulated by current climate models. *PAGES news*, **19** (1), 7–8.
- Goosse, H., H. Renssen, A. Timmermann, R. Bradley, and M. Mann, 2006: Using paleoclimate proxy-data to select an optimal realisation in an ensemble of simulations of the climate of the past millenium. *Climate Dynamics*, **27**, 165–184.
- Goosse, H., H. Renssen, A. Timmermann, and R. Bradley, 2005: Internal and forced climate variability during the last millennium: a model-data comparison using ensemble simulations. *Quaternary Science Reviews*, **24**, 1345–1360.
- Goswami, B., V. Krishnamurthy, and H. Annmalai, 1999: A broad-scale circulation index for the interannual variability of the Indian summer monsoon. *Quarterly Journal of the Royal Meteorological Society*, **125**, 611–633.
- Graham, N., C. Ammann, D. Fleitmann, K. M. Cobb, and J. Luterbacher, 2011: Support for global climate reorganization during the 'Medieval Climate Anomaly'. *Climate Dynamics*, **37**, 1217–1245.
- Guilyardi, E., A. Wittenberg, A. Fedorov, M. Collins, C. Wang, A. Capotondi, and G. JAN, 2009: Understanding El Nino in ocean-Atmosphere general circulation models. *Bull. Amer. Meteor. Soc.*, **90**, 325–340.
- Guo, Q., J. Cai, and X. Shao, 2004: Studies on variations of East-Asian Summer Monsoon during AD 1873-2000 (in Chinese). *Chinese Journal of Atmospheric Sciences*, **28**, 206–216.
- Hagemann, S., K. Arpe, and E. Roeckner, 2006: Evaluation of the hydrological cycle in the ECHAM5 model. *Journal of Climate*, **19** (16), 3810–3827.
- Hahn, D. and S. Manabe, 1975: The role of mountains in the south Asian monsoon circulation. *J. Atmos. Sci.*, **32** (8), 1515–1541.
- Hoerling, M., A. Kumar, and T. Xu, 2001: Robustness of the nonlinear climate response to ENSOs extreme phases. *Journal of Climate*, **14**, 1277–1293.
- Holmes, J., E. Cook, and B. Yang, 2009: Climate change over the past 2000 years in Western China. *Quaternary International*, **194**, 91–107.
- Holmes, J., J. Zhang, F. Chen, and M. Qiang, 2007: Paleoclimatic implications of an 850-year oxygen-isotope record from the northern Tibetan Plateau. *Geophysical Research Letters*, **34** (23), L23 403.
- Houghton, R., 2003: Revised estimates of the annual net flux of carbon to the atmosphere from changes in land use and land management 1850–2000. *Tellus B*, **55** (2), 378–390.

- Hsu, P., T. Li, and B. Wang, 2011: Trends in global monsoon area and precipitation over the past 30 years. *Geophysical Research Letters*, **38 (8)**, L08 701.
- Hughes, M. and H. Diaz, 1994: Was there a medieval warm period, and if so, where and when? *Climatic Change*, **26 (2)**, 109–142.
- Huybers, P. and W. Curry, 2006: Links between annual, Milankovitch and continuum temperature variability. *Nature*, **441**, 329–332.
- Jiang, T., Q. Zhang, R. Blender, and K. Fraedrich, 2006: Yangtze Delta floods and droughts of the last millennium: Abrupt changes and long term memory. *Theoretical and Applied Climatology*, **82 (3)**, 131–141.
- Jones, P. and M. Mann, 2004: Climate over past millennia. *Reviews of Geophysics*, **42 (2)**, 1–42.
- Ju, J. and J. Slingo, 1995: The Asian summer monsoon and ENSO. *Quarterly Journal of the Royal Meteorological Society*, **121 (525)**, 1133–1168.
- Jungclaus, J., 2009: Palaeoclimate: Lessons from the past millennium. *Nature Geoscience*, **2 (7)**, 468–470.
- Jungclaus, J., S. Lorenz, C. Timmreck, C. Reick, V. Brovkin, K. Six, J. Segschneider, et al., 2010: Climate and carbon-cycle variability over the last millennium. *Climate of the Past*, **6**, 1009–1044.
- Jungclaus, J. and the COMSIMM Team, 2009: Ensemble simulations of the Last Millennium using an Earth System Model including an interactive carbon cycle. *European General Assembly (EGU) 2011*.
- Kalnay, E., M. Kanamitsu, R. Kistler, W. Collins, D. Deaven, L. Gandin, M. Iredell, et al., 1996: The NCEP/NCAR 40-year reanalysis project. *Bulletin of the American Meteorological Society*, **77**, 437–471.
- Kawamura, R., 1998: A possible mechanism of the Asian summer monsoon-ENSO coupling. *Journal of the Meteorological Society of Japan*, **76 (6)**, 1009–1027.
- Kirchner, I. and H. Graf, 1995: Volcanos and El Niño: signal separation in Northern Hemisphere winter. *Climate Dynamics*, **11 (6)**, 341–358.
- Krivova, N., L. Balmaceda, and S. Solanki, 2007: Reconstruction of solar total irradiance since 1700 from the surface magnetic flux. *Astronomy and Astrophysics*, **467 (1)**, 335–346.
- Kruskal, W., 1957: Historical notes on the Wilcoxon unpaired two-sample test. *Journal of the American Statistical Association*, **52 (279)**, 356–360.
- Lau, K. M., K. M. Kim, and S. Yang, 2000: Dynamical and boundary forcing characteristics of regional components of the Asian summer monsoon. *Journal of Climate*, **13**, 2461–2482.

- Li, H., A. Dai, T. Zhou, and J. Lu, 2010: Responses of East Asian summer monsoon to historical SST and atmospheric forcing during 1950–2000. *Climate Dynamics*, **34** (4), 501–514.
- Liu, H., X. Shao, L. Huang, E. Liang, X. Fang, and L. Wang, 2005a: Statistical characteristics of annual precipitation variation during the past 1000 years in Delingha, Qinghai Province, China (in Chinese). *Quaternary Sciences*, **25** (2), 176–183.
- Liu, J., H. von Storch, X. Chen, E. Zorita, J. Zheng, and S. Wang, 2005b: Simulated and reconstructed winter temperature in the eastern China during the last millennium. *Chinese Science Bulletin*, **50** (24), 2872–2877.
- Liu, X., D. Qin, X. Shao, T. Chen, and J. Ren, 2005c: Temperature variations recovered from tree-rings in the middle Qilian Mountain over the last millennium. *Science in China Series D: Earth Sciences*, **48** (4), 521–529.
- Liu, Y., Z. An, H. Ma, Q. Cai, Z. Liu, J. Kutzbach, J. Shi, et al., 2006: Precipitation variation in the northeastern Tibetan Plateau recorded by the tree rings since 850 AD and its relevance to the Northern Hemisphere temperature. *Science in China Series D: Earth Sciences*, **49** (4), 408–420.
- Lohmann, U. and J. Feichter, 2005: Global indirect aerosol effects: a review. *Atmospheric Chemistry and Physics*, **5** (3), 715–737.
- Luterbacher, J., D. Dietrich, E. Xoplaki, M. Grosjean, and H. Wanner, 2004: European seasonal and annual temperature variability, trends, and extremes since 1500. *Science*, **303** (5663), 1499–1503.
- Luterbacher, J., et al., 2010: Circulation dynamics and its influence on European and Mediterranean January–April climate over the past half millennium: results and insights from instrumental data, documentary evidence and coupled climate models. *Climatic change*, **101** (1), 201–234.
- Mann, H. and D. Whitney, 1947: On a test of whether one of two random variables is stochastically larger than the other. *The annals of mathematical statistics*, **18** (1), 50–60.
- Mann, M., 2002: The value of multiple proxies. *Science*, **297**, 1481–1482.
- Mann, M., M. Cane, S. Zebiak, and A. Clement, 2005: Volcanic and solar forcing of the tropical Pacific over the past 1000 years. *Journal of Climate*, **18** (3), 447–456.
- Mann, M., Z. Zhang, M. Hughes, R. Bradley, S. Miller, S. Rutherford, and F. Ni, 2008: Proxy-based reconstructions of hemispheric and global surface temperature variations over the past two millennia. *Proceedings of the National Academy of Sciences*, **105** (36), 13 252–13 257.

- Mann, M., Z. Zhang, S. Rutherford, R. Bradley, M. Hughes, D. Shindell, C. Ammann, et al., 2009: Global signatures and dynamical origins of the Little Ice Age and Medieval Climate Anomaly. Supporting online material is available at www.sciencemag.org/cgi/content/full/326/5957/1256/DC1. Reprinted with permission from AAAS. *Science*, **326**, 1256–1260.
- Mao, X., S. Cheng, Y. Hong, Y. Zhu, and F. Wang, 2009: The influence of volcanism on paleoclimate in the northeast of China: Insights from Jinchuan peat, Jilin Province, China. *Chinese Journal of Geochemistry*, **28 (2)**, 212–219.
- Marland, G., T. Boden, and R. Andres, 2003: *Global, regional, and national fossil fuel CO2 emissions*. In: *Trends: a compendium of data on global change*. Carbon Dioxide Information Analysis Center, National Laboratory, U.S. Department of Energy, Oak Ridge. Available at http://cdiac.ornl.gov/trends/emis/em_cont.html.
- Marsland, S., H. Haak, J. Jungclaus, M. Latif, and F. Roske, 2003: The Max-Planck-Institute global ocean/sea ice model with orthogonal curvilinear coordinates. *Ocean Modelling*, **5 (2)**, 91–127.
- Mass, C. and D. Portman, 1989: Major volcanic eruptions and climate- A critical evaluation. *Journal of Climate*, **2 (6)**, 566–593.
- McGregor, S., A. Timmermann, and O. Timm, 2010: A unified proxy for ENSO and PDO variability since 1650. *Climate of the Past*, **6**, 1–17.
- McKee, T., N. Doesken, and J. Kleist, 1993: The relationship of drought frequency and duration to time scales. *Proceedings of the 8th Conference on Applied Climatology*, Vol. 184.
- Menon, S., J. Hansen, L. Nazarenko, and Y. Luo, 2002: Climate effects of black carbon aerosols in China and India. *Science*, **297**, 2250–2253.
- Meure, C., D. Etheridge, C. Trudinger, P. Steele, R. Langenfelds, T. Van Ommen, A. Smith, and J. Elkins, 2006: Law Dome CO₂, CH₄ and N₂O ice core records extended to 2000 years BP. *Geophys. Res. Lett.*, **33 (14)**, L14 810.
- Millennium group, 2012: Community simulations of the last millennium, Max Planck Institute for Meteorology, Coordinator: J. Jungclaus. Available at <http://www.mpimet.mpg.de/en/science/internal-projects/millennium.html>.
- Miller, G., Á. Geirsdóttir, Y. Zhong, D. Larsen, B. Otto Bliesner, M. Holland, D. Bailey, et al., 2012: Abrupt onset of the Little Ice Age triggered by volcanism and sustained by sea-ice/ocean feedbacks. *Geophysical Research Letters*, **39 (2)**, L02 708.
- National Research Council: North, G., F. Biondi, P. Bloomfield, J. Christy, K. Cuffey, R. Dickinson, E. Druffel, et al., (Eds.) , 2006: *Surface temperature reconstructions for the last 2000 years*. Washington, DC: National Academy Press. Available at: <http://www.nap.edu/catalog/11676.html> (last accessed 06 Jan 2012).

- Newhall, C. and S. Self, 1982: The volcanic explosivity index VEI- An estimate of explosive magnitude for historical volcanism. *Journal of Geophysical Research*, **87 (C2)**, 1231–1238.
- Oppenheimer, C., 2003: Climatic, environmental and human consequences of the largest known historic eruption: Tambora volcano (Indonesia) 1815. *Progress in Physical Geography*, **27 (2)**, 230–259.
- Peng, C., S. Buldyrev, S. Havlin, M. Simons, H. Stanley, and A. Goldberger, 1994: Mosaic organization of DNA nucleotides. *Physical Review E*, **49 (2)**, 1685.
- Peng, Y., C. Shen, W. Wang, and Y. Xu, 2010: Response of Summer Precipitation over Eastern China to Large Volcanic Eruptions. *Journal of Climate*, **23 (3)**, 818–824.
- Peng, Y., Y. Xu, and L. Jin, 2009: Climate changes over eastern China during the last millennium in simulations and reconstructions. *Quaternary International*, **208**, 11–18.
- Penland, C. and L. Matrosova, 2006: Studies of El Niño and interdecadal variability in tropical sea surface temperatures using a nonnormal filter. *Journal of Climate*, **19 (22)**, 5796–5815.
- Pongratz, J., 2009: A model estimate on the effect of anthropogenic land cover change on the climate of the last millennium. Ph.D. thesis, International Max Planck Research School on Earth System Modelling; University Hamburg.
- Pongratz, J., C. Reick, T. Raddatz, and M. Claussen, 2008: A reconstruction of global agricultural areas and land cover for the last millennium. *Global Biogeochemical Cycles*, **22 (3)**, GB3018.
- Pongratz, J., C. Reick, T. Raddatz, and M. Claussen, 2009: Effects of anthropogenic land cover change on the carbon cycle of the last millennium. *Global Biogeochemical Cycles*, **23 (4)**, GB4001.
- Qian, W., T. Ding, J. Fu, X. Lin, and Y. Zhu, 2008: Review on the data application and climate variability in China for various timescales. *Advances in Climate Change*, **4 (Suppl.)**, 1–6.
- Qian, W., Q. Hu, Y. Zhu, and D. Lee, 2003: Centennial-scale dry-wet variations in East Asia. *Climate Dynamics*, **21**, 77–89.
- Qiu, J., 2008: China: The third pole. *Nature*, **454**, 393–396, doi:10.1038/454393a.
- Quinn, W., 1993: The large-scale ENSO event, the El Niño and other important regional features. *Bull. Inst. fr. études andines*, **22**, 13–34.
- Raddatz, T., C. Reick, W. Knorr, J. Kattge, E. Roeckner, R. Schnur, K. Schnitzler, et al., 2007: Will the tropical land biosphere dominate the climate–carbon cycle feedback during the twenty-first century? *Climate Dynamics*, **29 (6)**, 565–574.

- Rampino, M. and S. Self, 1982: Historic eruptions of Tambora (1815), Krakatau (1883), and Agung (1963), their stratospheric aerosols, and climatic impact. *Quaternary Research*, **18** (2), 127–143.
- Robock, A., 2000: Volcanic eruptions and climate. *Reviews of Geophysics*, **38**, 191–219.
- Robock, A. and Y. Liu, 1994: The volcanic signal in Goddard Institute for Space Studies three-dimensional model simulations. *Journal of Climate*, **7**, 44–55.
- Robock, A. and J. Mao, 1995: The volcanic signal in surface temperature observations. *Journal of Climate*, **8** (5), 1086–1103.
- Robock, A., L. Oman, and G. Stenchikov, 2008: Regional climate responses to geoengineering with tropical and Arctic SO₂ injections. *Journal of Geophysical Research*, **113**, D16 101.
- Rodwell, M. and B. Hoskins, 1996: Monsoons and the dynamics of deserts. *Quarterly Journal of the Royal Meteorological Society*, **122**, 1385–1404.
- Roeckner, E., G. Baeuml, L. Bonaventura, R. Brokopf, M. Esch, M. Giorgetta, S. Hagemann, et al., 2003: *The Atmospheric General Circulation Model ECHAM5. Part 1: Model Description*. Max-Planck-Institut for Meteorology, Report, 127 pp.
- Rosenfeld, D., U. Lohmann, G. Raga, C. O’Dowd, M. Kulmala, S. Fuzzi, A. Reissell, and M. Andreae, 2008: Flood or drought: How do aerosols affect precipitation? *Science*, **321**, 1309–1313.
- Santer, B., T. Wigley, C. Doutriaux, J. Boyle, J. Hansen, P. Jones, G. Meehl, et al., 2001: Accounting for the effects of volcanoes and ENSO in comparisons of modeled and observed temperature trends. *Journal of Geophysical Research*, **106** (D22), 28 033–28 059.
- Schmidt, G., J. Jungclaus, C. Ammann, E. Bard, P. Braconnot, T. Crowley, G. Delaygue, and other, 2011: Climate forcing reconstructions for use in PMIP simulations of the last millennium (v1. 0). *Geoscientific Model Development*, **4**, 33–45.
- Schneider, D., C. Ammann, B. Otto Bliesner, and D. Kaufman, 2009: Climate response to large, high-latitude and low-latitude volcanic eruptions in the Community Climate System Model. *Journal of Geophysical Research*, **114**, D15 101.
- Schwarzschild, B., 2012: The triggering and persistence of the Little Ice Age. *Physics Today*, **April**, 15–16,18.
- Seager, R. and R. Burgman, 2011: Medieval hydroclimate revisited. *PAGES news*, **19**, 10–11.

- Seager, R., N. Graham, C. Herweijer, A. Gordon, Y. Kushnir, and E. Cook, 2007: Blueprints for Medieval hydroclimate. *Quaternary Science Reviews*, **26**, 2322–2336.
- Shao, X., L. Huang, H. Liu, E. Liang, X. Fang, and L. Wang, 2005: Reconstruction of precipitation variation from tree rings in recent 1000 years in Delingha, Qinghai. *Science in China Series D: Earth Sciences*, **48 (7)**, 939–949.
- Shen, C., W. Wang, Y. Peng, Y. Xu, and J. Zheng, 2009: Variability of summer precipitation over Eastern China during the last millennium. *Climate of the Past*, **5**, 129–141.
- Shindell, D., G. Schmidt, M. Mann, and G. Faluvegi, 2004: Dynamic winter climate response to large tropical volcanic eruptions since 1600. *Journal of Geophysical Research*, **109**, D05 104.
- Shindell, D., G. Schmidt, R. Miller, and M. Mann, 2003: Volcanic and solar forcing of climate change during the preindustrial era. *Journal of Climate*, **16 (24)**, 4094–4107.
- Sienz, F., I. Bordi, K. Fraedrich, and A. Schneidereit, 2007: Extreme dry and wet events in Iceland: Observations, simulations and scenarios. *Meteorologische Zeitschrift*, **16**, 9–16.
- Sims, A., D. Niyogi, and S. Raman, 2002: Adopting drought indices for estimating soil moisture: A North Carolina case study. *Geophysical Research Letters*, **29 (8)**, 1183.
- Sinha, A., K. Cannariato, L. Stott, H. Cheng, R. Edwards, M. Yadava, R. Ramesh, and I. Singh, 2007: A 900-year (600 to 1500 AD) record of the Indian summer monsoon precipitation from the core monsoon zone of India. *Geophysical Research Letters*, **34**, 16 707.
- Solomon, S., D. Qin, M. Manning, Z. Chen, M. Marquis, et al., 2007: *Climate Change 2007: The Physical Science Basis. Contribution to the Fourth Assessment Report of the Intergovernmental Panel on Climate Change*. Cambridge Univ Press, New York.
- Soon, W. and S. Yaskell, 2003: Year without a Summer. *Mercury*, **32 (3)**, 13–22.
- Stenchikov, G., T. Delworth, V. Ramaswamy, R. Stouffer, A. Wittenberg, and F. Zeng, 2009: Volcanic signals in oceans. *Journal of Geophysical Research*, **114**, D16 104.
- Stenchikov, G., K. Hamilton, R. Stouffer, A. Robock, V. Ramaswamy, B. Santer, and H. Graf, 2006: Arctic Oscillation response to volcanic eruptions in the IPCC AR4 climate models. *Journal of Geophysical Research*, **111**, D07 107.

- Stine, S., 1994: Extreme and persistent drought in California and Patagonia during mediaeval time. *Nature*, **369**, 546–549.
- Stothers, R., 1984: The great Tambora eruption in 1815 and its aftermath. *Science*, **224**, 1191–1198.
- Sun, Y., Y. Ding, and A. Dai, 2010: Changing links between South Asian summer monsoon circulation and tropospheric land-sea thermal contrasts under a warming scenario. *Geophysical Research Letters*, **37**, L02 704.
- Tan, L., Y. Cai, Z. An, R. Edwards, H. Cheng, C. Shen, and H. Zhang, 2010: Centennial-to decadal-scale monsoon precipitation variability in the semi-humid region, northern China during the last 1860 years: Records from stalagmites in Huangye Cave. *The Holocene*, **21** (2), 287–296.
- Tan, L., Y. Cai, L. Yi, Z. An, and L. Ai, 2008: Precipitation variations of Longxi, northeast margin of Tibetan Plateau since AD 960 and their relationship with solar activity. *Climate of the Past*, **4**, 19–28.
- Thompson, R., 1995: Volcanic eruptions and global temperatures. *Ambio*, **24** (5), 320–321.
- Timmreck, C., H. Graf, S. Lorenz, U. Niemeier, D. Zanchettin, D. Matei, J. Jungclaus, and T. Crowley, 2010: Aerosol size confines climate response to volcanic super-eruptions. *Geophysical Research Letters*, **37**, L24 705.
- Timmreck, C., S. Lorenz, T. Crowley, S. Kinne, T. Raddatz, M. Thomas, and J. Jungclaus, 2009: Limited temperature response to the very large AD 1258 volcanic eruption. *Geophysical Research Letters*, **36**, L21 708.
- Tsiropoula, G., 2003: Signatures of solar activity variability in meteorological parameters. *Journal of atmospheric and solar-terrestrial physics*, **65** (4), 469–482.
- Vautard, R. and M. Ghil, 1989: Singular spectrum analysis in nonlinear dynamics, with applications to paleoclimatic time series. *Physica D: Nonlinear Phenomena*, **35** (3), 395–424.
- Wang, B., Q. Bao, B. Hoskins, G. Wu, and Y. Liu, 2008: Tibetan Plateau warming and precipitation changes in East Asia. *Geophysical Research Letters*, **35**, L14 702.
- Wang, B. and Q. Ding, 2006: Changes in global monsoon precipitation over the past 56 years. *Geophysical Research Letters*, **33**, L06 711.
- Wang, B., R. Wu, and K. Lau, 2001: Interannual Variability of the Asian Summer Monsoon: Contrasts between the Indian and the Western North Pacific-East Asian Monsoons. *Journal of Climate*, **14** (20), 4073–4090.

- Wang, G., A. Dolman, R. Blender, and K. Fraedrich, 2010: Fluctuation regimes of soil moisture in ERA-40 re-analysis data. *Theoretical and Applied Climatology*, **99**, 1–8.
- Wang, N., X. Jiang, L. Thompson, and M. Davis, 2007a: Accumulation rates over the past 500 years recorded in ice cores from the northern and southern Tibetan Plateau, China. *Arctic, Antarctic, and Alpine Research*, **39** (4), 671–677.
- Wang, R., S. Wang, and K. Fraedrich, 1991: An approach to reconstruction of temperature on a seasonal basis using historical documents from China. *International Journal of Climatology*, **11** (4), 381–392.
- Wang, S., X. Wen, Y. LUO, W. Dong, Z. Zhao, and B. Yang, 2007b: Reconstruction of temperature series of China for the last 1000 years. *Chinese Science Bulletin*, **52** (23), 3272–3280.
- Wang, Y., H. Cheng, R. Edwards, Y. He, X. Kong, Z. An, J. Wu, et al., 2005: The Holocene Asian monsoon: links to solar changes and North Atlantic climate. *Science*, **308**, 854–857.
- Wei, F. and T. Zhang, 2010: Oscillation characteristics of summer precipitation in the Huaihe River valley and relevant climate background. *Science China Earth Sciences*, **53**, 301–316.
- Wetzel, P., E. Maier Reimer, M. Botzet, J. Jungclaus, N. Keenlyside, and M. Latif, 2006: Effects of ocean biology on the penetrative radiation in a coupled climate model. *Journal of Climate*, **19** (16), 3973–3987.
- Wu, G., Y. Liu, Q. Zhang, A. Duan, T. Wang, R. Wan, X. Liu, et al., 2007: The influence of mechanical and thermal forcing by the Tibetan Plateau on Asian climate. *Journal of Hydrometeorology*, **8** (4), 770–789.
- Wu, R. and B. Wang, 2002: A Contrast of the East Asian Summer Monsoon-ENSO Relationship between 1962-77 and 1978-93*. *Journal of Climate*, **15** (22), 3266–3279.
- Xu, X., C. Lu, X. Shi, S. Gao, A. Xu, X. Lu, C. Shi, and X. Gao, 2008: World water tower: An atmospheric perspective. *Geophysical Research Letters*, **35** (20), L20 185.
- Yang, B., A. Braeuning, K. Johnson, and Y. Shi, 2002: General characteristics of temperature variation in China during the last two millennia. *Geophysical Research Letters*, **29** (9), 1–4.
- Yang, B., A. Braeuning, S. Y., and J. Zhang, 2003: Temperature variations on the Tibetan Plateau over the last two millennia. *Chinese Science Bulletin*, **48** (14), 1446–1450.

- Yang, B., A. Bräuning, Z. Dong, Z. Zhang, and K. Jiao, 2008: Late Holocene monsoonal temperate glacier fluctuations on the Tibetan Plateau. *Global and Planetary Change*, **60**, 126–140.
- Yang, B., Y. Shi, and H. Li, 2001: Climatic variations in China over the last 2000 years. *Chinese Geographical Science*, **11** (2), 97–103.
- Yang, B., J. Wang, A. Bräuning, Z. Dong, and J. Esper, 2009: Late Holocene climatic and environmental changes in arid central Asia. *Quaternary International*, **194**, 68–78.
- Yang, Y., Z. Man, and J. Zheng, 2005: A serious famine in Yunnan (1815-1817) and the eruption of Tambora volcano (in Chinese). *Fudan Journal (Social Sciences)*, **1** (1), 79–85.
- Yao, T., L. Thompson, D. Qin, L. Tian, K. Jiao, Z. Yang, and C. Xie, 1996: Variations in temperature and precipitation in the past 2000 a on the Xizang (Tibet) Plateau–Guliya ice core record. *Science in China Series D: Earth Sciences*, **4**, 425–433.
- Yoshimori, M., T. Stocker, C. Raible, and M. Renold, 2005: Externally forced and internal variability in ensemble climate simulations of the Maunder Minimum. *Journal of Climate*, **18**, 4253–4270.
- Zhai, J., B. Su, V. Krysanova, T. Vetter, C. Gao, and T. Jiang, 2010: Spatial variation and trends in PDSI and SPI indices and their relation to streamflow in 10 large regions of China. *Journal of Climate*, **23** (3), 649–663.
- Zhang, D., R. Blender, and K. Fraedrich, 2011: Volcanic and ENSO effects in China in simulations and reconstructions: Tambora eruption 1815. *Climate of the Past Discussion*, **7**, 2061–2088.
- Zhang, D., R. Blender, and K. Fraedrich, 2012: Volcanoes and ENSO in millennium simulations: global impacts and regional reconstructions in East Asia. *Theoretical and Applied Climatology (accepted)*, doi:10.1007/s00704-012-0670-6.
- Zhang, D., R. Blender, X. Zhu, and K. Fraedrich, 2010: Temperature variability in China in an ensemble simulation for the last 1,200 years. *Theoretical and Applied Climatology*, **103**, 387–399.
- Zhang, P., H. Cheng, R. Edwards, F. Chen, Y. Wang, X. Yang, J. Liu, et al., 2008a: A test of climate, sun, and culture relationships from an 1810-year Chinese cave record. *Science*, **322**, 940–942.
- Zhang, Q., M. Gemmer, and J. Chen, 2008b: Climate changes and flood/drought risk in the Yangtze Delta, China, during the past millennium. *Quaternary International*, **176**, 62–69.

- Zhang, Y., Z. Kong, S. Yan, Z. Yang, and J. Ni, 2009: 'Medieval Warm Period' on the northern slope of central Tianshan Mountains, Xinjiang, NW China. *Geophysical Research Letters*, **36**, L11 702.
- Zheng, J., W. Wang, Q. Ge, Z. Man, and P. Zhang, 2006: Precipitation variability and extreme events in eastern China during the past 1500 years. *Terrestrial Atmospheric and Oceanic Sciences*, **17 (3)**, 579.
- Zhou, T., L. Zhang, and H. Li, 2008: Changes in global land monsoon area and total rainfall accumulation over the last half century. *Geophysical Research Letters*, **35**, L16 707.
- Zhu, H., X. Shao, Z. Yin, and L. Huang, 2011: Early summer temperature reconstruction in the eastern Tibetan plateau since ad 1440 using tree-ring width of *Sabina tibetica*. *Theoretical and Applied Climatology*, **106**, 45–53.
- Zhu, X., O. Bothe, and K. Fraedrich, 2010: Summer atmospheric bridging between Europe and East Asia: Influences on drought and wetness on the Tibetan Plateau. *Quaternary International*, doi:10.1016/j.quaint.2010.06.015.
- Zhu, X., K. Fraedrich, and R. Blender, 2006: Variability regimes of simulated Atlantic MOC. *Geophysical Research Letters*, **33**, L21 603.
- Zorita, E., 2012: *Climate impacts on the Baltic Sea :From Science to Policy. Chapter 4: A basic introduction to climate modeling and its uncertainties (in press)*.
- Zorita, E., H. Von Storch, F. Gonzalez Rouco, U. Cubasch, J. Luterbacher, S. Legutke, I. Fischer Bruns, and U. Schlese, 2004: Climate evolution in the last five centuries simulated by an atmosphere-ocean model: global temperatures, the North Atlantic Oscillation and the Late Maunder Minimum. *Meteorologische Zeitschrift*, **13 (4)**, 271–289.

Acknowledgement

My immense gratitude goes to everyone who supported the creation of my PhD thesis:

First of all, I would like to thank my supervisor Prof. Dr. Klaus Fraedrich for his innumerable scientific ideas and inspiring advises during the whole PhD time, which enabled the completion of my thesis. I'm also thankful to my second supervisor Dr. Richard Blender for his kind guidances, fruitful discussions and being always available for my questions and problems all the time, particularly on writing scientific texts. Without you both, nothing could have been done. I would also like to thank my Advisory Panel Chair Prof. Dr. Martin Claussen for the precious comments and worthy suggestions on all the panel meetings that have improved my work.

Special thanks to Dr. Xiuhua Zhu and Dr. Kathrin Riemann-Campe for their generous and countless help in answering all my technical and scientific questions. Especially at the beginning of my PhD, their hospitalities and help warm up my winter. I thank Frank Lunkeit for his first-time and clear replies to all my questions arising on the model simulations. I thank Frank Sienz, Silke Schubert and Edibert Kirk for the technical support associated with data operations and my computer problems. In this view, I thank all my colleatues in the Theoretical Meteorology Group, for their comprehensive help and information in daily work and group meetings. During my stay in Hamburg which I enjoyed very much, they together with my supervisors provided a friendly and inspiring working atmosphere.

I thank the Millennium consortium, especially Johann Jungclaus, Julia Pongratz, Thomas Raddatz, Stephan Lorenz, Christian Reik and Veronika Gayler at the Max Planck Institute for Meteorology for providing the millennium experiments and for the stimulating discussions in the group meetings and over emails. I thank the support for the visit to Max Planck Institute for Meteorology by the Institute of Geographical Sciences and Natural Resources Research, Chinese Academy of Sciences. I thank the KlimaCampus for supporting me visiting conferences.

With respect to the manuscripts included in this thesis, I would like to acknowledge Klaus Fraedrich and Richard Blender as the first referees, and the anonymous reviewers for constructive comments. I also thank all the previous scientific workers for providing the reconstructed data in their papers.

On a more personal level, I want to thank my dear mother Shuxian Gao and my husband Philip Willuweit for their unconditional supports including many recreative weekends and nights at home, as well as encouraging me and sharing my stresses especially in the last several months.

Dan Zhang

18. Mai 2012, Hamburg